

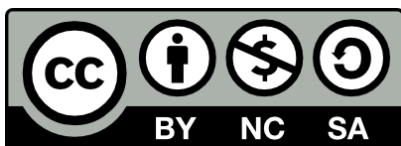
# **Fourier Transform Four-Wave Mixing Spectroscopy with Femtosecond Single-Shot Interferometry**

Inauguraldissertation  
der Philosophisch-naturwissenschaftlichen Fakultät  
der Universität Bern

vorgelegt von

**Aaron Christopher Riede**  
aus Deutschland

Leiter der Arbeit:  
Prof. Dr. Andrea Cannizzo  
Institut für Angewandte Physik



This work is licensed under a Creative Commons Attribution 4.0 International License <https://creativecommons.org/licenses/by/4.0/>

# **Fourier Transform Four-Wave Mixing Spectroscopy with Femtosecond Single-Shot Interferometry**

Inauguraldissertation  
der Philosophisch-naturwissenschaftlichen Fakultät  
der Universität Bern

vorgelegt von

**Aaron Christopher Riede**  
aus Deutschland

Leiter der Arbeit:  
Prof. Dr. Andrea Cannizzo  
Institut für Angewandte Physik

Von der Philosophisch-naturwissenschaftlichen Fakultät angenommen.

Bern, 04. Februar 2022

Der Dekan  
Prof. Dr. Zoltán Balogh



# Contents

---

<b>Contents</b>	<b>i</b>
<b>List of Figures</b>	<b>iv</b>
<b>List of Acronyms</b>	<b>v</b>
<b>1 Introduction</b>	<b>1</b>
<b>2 Concept of Four-Wave Mixing Spectroscopy</b>	<b>5</b>
2.1 Theory of four-wave mixing spectroscopy . . . . .	5
2.1.1 Density matrix approach . . . . .	6
2.1.2 Perturbative expansion of the polarization . . . . .	7
2.1.3 First-order response function . . . . .	10
2.1.4 Dephasing and Bloch picture . . . . .	12
2.1.5 Third-order response function . . . . .	17
2.1.6 Link to molecular response: the susceptibility . . . . .	21
2.1.7 Semi-impulsive limit and phase matching . . . . .	21
2.2 Experimental realizations . . . . .	23
2.2.1 Frequency domain spectroscopy . . . . .	23
2.2.2 Time domain spectroscopy and heterodyne detection . . . . .	24
2.2.3 Box-CARS geometry . . . . .	26
2.2.4 Phase stabilization . . . . .	27
2.2.5 Delay control . . . . .	29
2.2.6 The approach of this work: single-shot interferometry . . . . .	31
<b>3 Single-Shot Interferometry</b>	<b>35</b>
3.1 Phase stability . . . . .	35
3.2 Pump-probe-to-box-CARS element . . . . .	38
3.3 Delay extraction algorithm . . . . .	42
3.4 Phase calibration procedure . . . . .	46
3.5 Simplification of translation stage alignment . . . . .	48
3.6 Conclusion . . . . .	49

<b>4</b>	<b>Shaping and Characterization of Ultrabroad Pulses</b>	<b>51</b>
4.1	Pulse shaping techniques . . . . .	53
4.1.1	Material transmission . . . . .	53
4.1.2	Grating compressor . . . . .	54
4.1.3	Prism compressor . . . . .	55
4.1.4	Chirped mirror . . . . .	57
4.1.5	Adaptive pulse shaping . . . . .	60
4.2	Mathematical description of adaptive pulse shaping . . . . .	63
4.3	Ray tracing simulation of adaptive pulse shaping . . . . .	65
4.4	Pulse characterization techniques . . . . .	69
4.4.1	Cross-phase modulation . . . . .	69
4.4.2	Transient grating FROG . . . . .	75
4.5	Pulse generation and compression . . . . .	77
4.5.1	NOPA . . . . .	77
4.5.2	Supercontinuum . . . . .	81
4.6	Conclusion . . . . .	83
<b>5</b>	<b>Towards FT FWM Spectroscopy Experiments</b>	<b>87</b>
5.1	Homodyne TG spectroscopy . . . . .	87
5.2	Comparison of approaches to scan delays . . . . .	89
5.2.1	Delay scan via translation stage . . . . .	90
5.2.2	Delay scan via mechanical fluctuations . . . . .	92
5.3	Delay uncertainty simulations . . . . .	95
5.4	FT FWM spectroscopy . . . . .	97
5.4.1	Experimental parameters . . . . .	97
5.4.2	Phase calibration, binning and shot selection . . . . .	99
5.4.3	Presentation and discussion of results . . . . .	102
5.4.4	Independent control of the population time . . . . .	106
5.5	Conclusion . . . . .	108
<b>6</b>	<b>Concluding Remarks</b>	<b>109</b>
6.1	Summary . . . . .	109
6.2	Prospect . . . . .	111
	<b>Appendix</b>	<b>I</b>
	<b>Bibliography</b>	<b>III</b>

# List of Figures

---

2.1	Interaction sequence . . . . .	9
2.2	Inhomogeneous dephasing . . . . .	13
2.3	Illustration of inhomogeneous Bloch vectors . . . . .	16
2.4	Response of rephasing and non-rephasing pathway . . . . .	18
2.5	Bloch vector evolution of the rephasing pathway $R_1$ . . . . .	20
2.6	Depiction of the box-CARS geometry . . . . .	22
2.7	Pulse sequences in time and frequency domain spectroscopy . . . . .	24
2.8	Depiction of the box-CARS geometry with LO . . . . .	26
2.9	Passive phase stabilization approaches . . . . .	28
2.10	Pair of glass wedges . . . . .	30
2.11	Conceptual sketch of the multi-camera approach . . . . .	33
3.1	Schematic of Michelson interferometer and home-built spectrometer . . . . .	36
3.2	Comparison of SSI and averaged interferograms . . . . .	38
3.3	Schematic of P2B element . . . . .	39
3.4	Differential phase determination setup . . . . .	40
3.5	Delay extraction algorithm . . . . .	43
3.6	Results of delay extraction . . . . .	45
3.7	Temporal arrangements of pulses . . . . .	46
3.8	Effect of a tilted translation stage in a Michelson interferometer . . . . .	48
4.1	Effect of transmission through glass on a laser pulse . . . . .	54
4.2	Schematics of prism and grating compressor setups . . . . .	55
4.3	Schematic of a chirped mirror . . . . .	57
4.4	Group delay of chirped mirror pair . . . . .	58
4.5	Schematic of adaptive pulse shaping . . . . .	59
4.6	Diffraction shaping . . . . .	62
4.7	Color code images of the phase in diffraction based shaping . . . . .	63
4.8	Ray tracing simulation on adaptive pulse shaping . . . . .	67
4.9	Shaping capability of deformable mirrors . . . . .	68
4.10	Simulation of the cross-phase modulation of a chirped pulse . . . . .	70
4.11	Vanishing of XPM for compressed pulses . . . . .	71
4.12	XPM trace of supercontinuum . . . . .	72
4.13	GD extraction from XPM trace . . . . .	73

4.14	Induction of the transient grating . . . . .	76
4.15	Schematic of the FT FWM spectroscopy setup . . . . .	77
4.16	Typical NOPA spectra . . . . .	78
4.18	Delay control with two translation stages . . . . .	79
4.17	Bandwidth selection inside NOPA . . . . .	79
4.19	TG FROG traces of NOPA pulses . . . . .	81
4.20	Schematic of the SC compression setup . . . . .	82
4.21	Iterative compression SC pulses . . . . .	84
5.1	Phase matching and pulse sequence in TG spectroscopy experiment	87
5.2	NOPA spectrum and absorption of Rhodamine 800 . . . . .	88
5.3	TG spectroscopy result for Rhodamine 800 in ethanol . . . . .	89
5.4	Delays from phase calibration procedure . . . . .	90
5.5	Repeatability of difference in delays . . . . .	91
5.6	Fluctuation-induced delays . . . . .	93
5.7	Simulated 2D spectra with delay uncertainty . . . . .	96
5.8	Phase matching and pulse sequence in FT FWM experiment . . .	97
5.9	Histogram and correlation plots of delays in FT FWM experiment	98
5.10	Density of shots in correlation plot . . . . .	100
5.11	Schematic of binning procedures . . . . .	101
5.12	Spectrogram and 2D spectrum of FT FWM on Rhodamine 800 .	103
5.13	Comparison of 2D spectra analyzed with different parameters . .	105
5.14	Prevention of an unconstant population time . . . . .	107
6.1	Knife-edge prism mirror in Michelson interferometer . . . . .	111



# List of Acronyms

---

<b>AOM</b>	acousto-optic modulator
<b>AOPDF</b>	acousto-optic programmable dispersive filter
<b>ARC</b>	anti-reflective coating
<b>CaF<sub>2</sub></b>	calcium fluoride
<b>CARS</b>	coherent anti-Stokes Raman spectroscopy
<b>CEP</b>	carrier envelope phase
<b>CMP</b>	chirped mirror pair
<b>DCM</b>	double chirped mirror
<b>DPD</b>	differential phase determination
<b>FFT</b>	fast Fourier transform
<b>FID</b>	free induction decay
<b>FOD</b>	fourth order dispersion
<b>FROG</b>	frequency-resolved optical gating
<b>FT</b>	Fourier transform
<b>FWHM</b>	full width at half maximum
<b>FWM</b>	four-wave mixing
<b>GD</b>	group delay
<b>GDD</b>	group delay dispersion
<b>LC SLM</b>	liquid crystal spatial light modulator
<b>LO</b>	local oscillator
<b>MIR</b>	mid-infrared
<b>NIR</b>	near-infrared
<b>NOPA</b>	noncollinear optical parametric amplifier

**OKE** optical Kerr effect  
**P2B** pump-probe-to-box-CARS  
**PTS** piezoelectric translation stage  
**SC** supercontinuum  
**SLM** spatial light modulator  
**SNR** signal-to-noise ratio  
**SSI** single-shot interferometry  
**TAS** transient-absorption spectroscopy  
**TG** transient grating  
**TOD** third order dispersion  
**UV** ultraviolet  
**XPM** cross-phase modulation  
**XUV** extreme ultraviolet

# Chapter 1

---

## Introduction

Optical spectroscopy in its many variations is one of the most powerful tools of investigation and yielded countless insights in different scientific fields like molecular chemistry, biology, medicine and astronomy – just to mention a few. The advent of pulsed laser systems was a milestone in the history of spectroscopy, whose relevance was recognized by awarding the Nobel prize in physics to Mourou and Strickland in 2018 for their contribution to the generation of high-intensity, ultrashort optical pulses. The impact has been twofold: on the one hand it allowed to design experiments with femtosecond time resolution and on the other hand, it enabled to reach electromagnetic fields intense enough to induce detectable nonlinear effects in matter.

The former permits to investigate dynamic molecular processes in the time scale of nuclear motions (tens of femtoseconds). This has literally skyrocketed our comprehension of physical and chemical phenomena in molecules and condensed matter. The examples are countless, and an overview can be found in several review articles and books (Maiuri et al., 2020; Hannaford, 2005). By now, spectroscopic experiments with time resolutions down to attoseconds have been performed (Cavalieri et al., 2007).

The latter aspect of ultrafast optical pulses revolutionized our way how we can manipulate matter and light and ultimately led to experimental techniques that among others include multiphoton processes, higher harmonics generation, supercontinuum generation, non-thermal surface ablation and parametric amplification. Many of them today are the base of the most successful applications of ultrafast lasers in various fields.

In this context, a unique spectroscopic technique is Fourier transform (FT) four-wave mixing (FWM) spectroscopy: a multidimensional spectroscopic technique in which the two aspects, that were mentioned beforehand, merge to use time-resolved nonlinear responses of matter to unveil its evolution at a deeper level.

It has the unique capability of tracking down couplings among different molecular states, disentangling inhomogeneous and homogeneous contributions to spectral line widths and investigating quantum coherences in different molecular systems. The first experiments in this field were realized in the near-infrared (Hybl et al., 1998) and mid-infrared (Hamm et al., 1998; Woutersen and Hamm, 2000; Golonzka et al., 2001) to investigate vibrational transitions in molecules.

As explicitly described within this thesis, the three most challenging prerequisites for a successful implementation of this insightful experimental technique are phase stability between the involved laser pulses, a precise delay control and pulse compression down to the Fourier limit

Due to the necessity of phase stability, which is easier to fulfill for lower frequencies, it took some years to transfer this technology to the visible and ultraviolet spectrum, where electronic transitions can be probed (Brixner et al., 2004; Cowan et al., 2004; Brixner et al., 2005). For that, elaborate approaches for phase stabilization have been developed by different research groups, as it is in more detail described in section 2.2. However, all of them aim to suppress phase fluctuations at the cost of limiting the performance of the experiment, e.g. the bandwidth or the pulse geometry.

In this work, I present a novel experimental scheme to carry out FT FWM experiments, which bases on the fact, that phase fluctuations arise from processes like mechanical vibrations of optical components and air turbulences, which are accumulated throughout the integration time of the detection system. However, in a pulsed laser experiment, the effective integration time is given by the pulse length and not the electronics of the detector, if data are collected on a single-shot basis instead of averaging over many shots. As a consequence, with a femtosecond laser system, it is possible to reduce the effective integration time by many orders of magnitude, which enables to run interferometric experiments without a loss of phase information even in the presence of phase fluctuations (Achazi and Cannizzo, 2017).

Furthermore, by implementing three synchronized spectrometers to simultaneously measure all relevant interpulse delays with interferometric precision, the presented approach allows to select the shots that fulfill all requirements in terms of delay times during the analysis and thus makes a precise experimental delay control gratuitous. This represents a Copernican revolution compared to the approach followed until now, because it does not seek for any phase stabilization.

On the contrary, since mechanical fluctuations lead to a statistical distribution of delays, the novel approach benefits from the presence of noise sources.

In addition, the concept of multi-camera single-shot interferometry (SSI) in a FT FWM spectroscopy experiment is not restricted to the visible spectrum, but straightforwardly can be applied in basically any frequency range, where short pulses can be generated and single-shot detectors are available.

This thesis is structured in six chapters. After this **introduction**, the **second chapter** derives the concept of FWM spectroscopy theoretically. Furthermore, an overview on existing experimental techniques to solve the issues of delay control and phase stabilization, together with their advantages and drawbacks is given. Finally the approach of this work and how it tackles challenges of existing techniques is presented.

In the **third chapter**, the reader is introduced to the concept of SSI in a multi-camera approach, how it overcomes the need for phase stabilization and precise delay control and how it is implemented in this work. Moreover, an algorithm that allows to extract single-shot delays with a sub-10 as precision from interferograms is developed and tested.

Subsequently, in **chapter four**, I discuss different pulse shaping techniques and how they effect the spectral and temporal structure of ultrafast laser pulses. This includes static methods like grating and prism compressors, as well as chirped mirrors. The main focus, however, is put on adaptive pulse shaping with a deformable mirror or a liquid crystal spatial light modulator (LC SLM) as a phase mask. I present a new approach to adaptive pulse shaping by using a prism as a dispersing element and discuss its benefits and drawbacks on the basis of ray tracing simulation results. Moreover, the reader is introduced to pulse characterization with the help of transient grating (TG) frequency-resolved optical gating (FROG) and the cross-phase modulation (XPM). Finally, both are used to characterize the spectral phase of ultrabroad pulses that were compressed with a chirped mirror pair and with an iterative method using an LC SLM, respectively.

In the **fifth chapter**, different outcomes of experimental FWM spectroscopy experiments are presented. I start with TG spectroscopy results to proof the appropriateness of Rhodamine 800 as a characterization sample for the FT FWM spectroscopy experiment. To continue, two methods to vary the delay between the

excitation pulses in an FT FWM experiment are analyzed and compared. One of them bases on a purposeful induction of mechanical noise to the system. Furthermore, the effects of delay uncertainties are discussed on the basis of simulation results. Finally, I show the outcomes of an FT FWM spectroscopy experiment where analysis methods, which are unique to SSI, are tested on real data. Indeed, a strong improvement of the signal strength, gives evidence on the superior performance of SSI with respect to conventional acquisition schemes.

The **last chapter** concludes this thesis and gives a prospect on future developments, FT FWM spectroscopy in combination with SSI could enable, as well as further possible improvements of the presented approach.

## Concept of Four-Wave Mixing Spectroscopy

### 2.1 Theory of four-wave mixing spectroscopy

In this section, the theory behind four-wave mixing spectroscopy is derived. Its argumentative structure is mainly based on Hamm and Zanni (2011).

Within the electric dipole approximation, a molecule that interacts with an electric field  $E(t)$  can be described in the Schrödinger picture with the Hamilton operator  $H_0$  of an isolated molecule and the interaction energy  $W(t)$

$$H = H_0 + W(t) \quad (2.1)$$

$$W(t) = -\mu E(t), \quad (2.2)$$

where  $\mu$  is the dipole moment  $\mu$  of the molecule. In the following, a semi-classical treatment will be applied to this interaction, where the molecule will be considered a quantum-mechanical object and the electric field as a classical wave.

Furthermore, the electric field is described as light pulses in the semi-impulsive limit. This includes, that any pulses in the experiment are shorter than the fastest processes under investigation, but longer than one period of the light and thus have a well-defined frequency  $\omega$  and phase  $\varphi$ , as well as a wave vector  $\vec{k}$ .

$$E(\vec{r}, t) = E_0 \delta(t) e^{\mp i\omega t \pm i\vec{k} \cdot \vec{r} \pm i\varphi}. \quad (2.3)$$

The time evolution of the molecular wave function  $|\psi\rangle$  is given by the time-dependent Schrödinger equation.

$$i\hbar \frac{\partial}{\partial t} |\psi\rangle = H |\psi\rangle \quad (2.4)$$

An expansion of  $|\psi\rangle$  in the base of the Hamiltonian eigenvectors  $|n\rangle$  is used to solve equation 2.4 for the time evolution of  $|\psi\rangle$ .

$$|\psi(t)\rangle = \sum_n c_n(t) |n\rangle \quad (2.5)$$

For every eigenstate  $|n\rangle$ , the probability amplitude is given by  $c_n$ , whose time evolution is described by

$$c_n(t) = c_n(0)e^{iE_n t/\hbar}. \quad (2.6)$$

### 2.1.1 Density matrix approach

To describe the interaction of light and matter and in particular, the evolution of an ensemble of molecules after excitation with a laser pulse in a statistical environment like a solvent, the concept of density matrices is convenient and will be introduced in the following. The definition of the density matrix is

$$\rho(t) = |\psi(t)\rangle \langle\psi(t)|. \quad (2.7)$$

Plugging the eigenvector expansion in equation 2.5 into the definition of  $\rho$  yields the density matrix elements

$$\rho_{nm}(t) = c_n(t)c_m^*(t). \quad (2.8)$$

The probability of a system for being in the state  $|n\rangle$  is thus described by the diagonal element  $\rho_{nn}$ , whereas the off-diagonal terms  $\rho_{nm}$  can be viewed as the coherence terms between the states  $|n\rangle$  and  $|m\rangle$ . The expectation value of an operator  $A$  is expressed as

$$\begin{aligned} \langle\psi(t)| A |\psi(t)\rangle &= \sum_m c_m^*(t) \sum_n c_n(t) \langle m| A |n\rangle = \sum_{m,n} c_m^*(t)c_n(t)A_{mn} \\ &= \sum_{m,n} \rho_{nm}A_{mn} = \text{Tr}(\rho A) = \langle\rho A\rangle = \langle A\rho\rangle. \end{aligned} \quad (2.9)$$

In literature, angle brackets  $\langle...\rangle$  are used to express the quantum-mechanical expectation value and/or the trace of an operator. To prevent confusion, in this work,  $\langle...\rangle$  always indicates a trace. The last equality in equation 2.9 is due to the invariance of the trace under cyclic permutations.



The time evolution of the density matrix is given by the Liouville-von Neumann equation, which is the analogon of the time dependent Schrödinger equation in the density matrix picture.

$$\begin{aligned}\frac{d}{dt}\rho &= -\frac{i}{\hbar} [H, \rho] \\ &= -\frac{i}{\hbar} (H\rho - \rho H)\end{aligned}\quad (2.10)$$

The solution to the Liouville-von Neumann equation without an external perturbation and thus a time independent Hamilton operator is

$$\rho_{nm}(t) = \rho_{nm}(0)e^{-i\omega_{nm}t}, \quad (2.11)$$

with  $\omega_{nm} = (E_m - E_n)/\hbar$  being the resonant frequency between the energy levels  $n$  and  $m$ . The diagonal elements of the density matrix are constant  $\rho_{nn}(t) = \rho_{nn}(0)$ .

In spectroscopy, the so called interaction picture is often used, since it allows a separation of the dynamics that are intrinsic to the molecule (equation 2.11) and those that are induced by the perturbation of the laser pulse. When it is applied to the density matrix formalism, one gets a kinetic equation that works in analogy to the Liouville-van Neumann equation with a new interaction potential  $W_I(t)$  (Hamm and Zanni, 2011). The subscript I indicates the interaction picture.

$$\frac{d}{dt}\rho_I(t) = -\frac{i}{\hbar} [W_I(t), \rho_I(t)] \quad (2.12)$$

$$\rho(t) = e^{-\frac{i}{\hbar}H_0(t-t_0)} \rho_I(t) e^{\frac{i}{\hbar}H_0(t-t_0)} \quad (2.13)$$

$$W_I(t) = e^{\frac{i}{\hbar}H_0(t-t_0)} W e^{-\frac{i}{\hbar}H_0(t-t_0)} \quad (2.14)$$

### 2.1.2 Perturbative expansion of the polarization

The first-order differential equation 2.12 can be solved by time-dependent perturbation theory through a perturbative expansion. Therefore one integrates equation 2.12 and plugs it into itself.

$$\rho_I(t) = \rho_I(t_0) - \int_{t_0}^t \frac{i}{\hbar} [W_I(\tau_1), \rho_I(t_0)] d\tau_1 \quad (2.15)$$

$$= \rho_I(t_0) - \int_{t_0}^t \frac{i}{\hbar} \left[ W_I(\tau_2), - \int_{t_0}^{\tau_2} \frac{i}{\hbar} [W_I(\tau_1), \rho_I(t_0)] d\tau_1 \right] d\tau_2 \quad (2.16)$$

By iteratively applying this step one gets a solution that is a sum of multiple integrals. The  $n$ th summand corresponds to the  $n$ th order of the perturbative expansion and contains  $n$  integrals.

$$\rho_I(t) = \sum_{n=0}^{\infty} \rho_I^{(n)}(t) = \rho_I(t_0) - \sum_{n=1}^{\infty} \left( -\frac{i}{\hbar} \right)^n \int_{t_0}^t d\tau_n \int_{t_0}^{\tau_n} d\tau_{n-1} \dots \int_{t_0}^{\tau_2} d\tau_1 E(\tau_n) E(\tau_{n-1}) \dots E(\tau_1) [\mu_I(\tau_n), [\mu_I(\tau_{n-1}), \dots [\mu_I(\tau_1), \rho_I(t_0)] \dots]], \quad (2.17)$$

where  $\rho_I^{(n)}$  is the  $n$ th perturbation order of the density matrix in the interaction picture. Here, the interaction energy  $W_I$  was replaced by equation 2.2. The dipole operator in the interaction picture  $\mu_I$  is defined as

$$\mu_I(t) = e^{\frac{i}{\hbar} H_0(t-t_0)} \mu e^{-\frac{i}{\hbar} H_0(t-t_0)}. \quad (2.18)$$

Equation 2.13 and  $\rho_I(t_0) = \rho(t_0)$  is used to obtain the perturbative expansion of the density matrix in the Schrödinger picture.

$$\rho(t) = \rho(t_0) - \sum_{n=1}^{\infty} \left( -\frac{i}{\hbar} \right)^n \int_{t_0}^t d\tau_n \int_{t_0}^{\tau_n} d\tau_{n-1} \dots \int_{t_0}^{\tau_2} d\tau_1 E(\tau_n) E(\tau_{n-1}) \dots E(\tau_1) e^{-\frac{i}{\hbar} H_0(t-t_0)} [\mu_I(\tau_n), [\mu_I(\tau_{n-1}), \dots [\mu_I(\tau_1), \rho(t_0)] \dots]] e^{+\frac{i}{\hbar} H_0(t-t_0)} \quad (2.19)$$

$$= \sum_{n=0}^{\infty} \rho^{(n)}(t). \quad (2.20)$$

Ultimately this derivation targets an expression for the emitted electric field and thus the macroscopic polarization  $P(t)$  of a sample. It is given by the expectation value of the dipole operator  $\mu$ . From equation 2.9, one gets

$$P(t) = \langle \mu(t) \rho(t) \rangle \quad (2.21)$$

The expansion orders of the density matrix in equation 2.19 also reflect in expansion orders of the macroscopic polarization. By using the invariance of the trace after a cyclic permutation one can eliminate the time evolution operators in  $\mu_I$  and end up with the dipole operators in the Schrödinger picture. This is achieved by applying the product rule for commutators several times. In detail, the calculus can be looked up in the Appendix, Problem A.

Furthermore,  $t_0$  is a point in time before the first interaction. Since the density

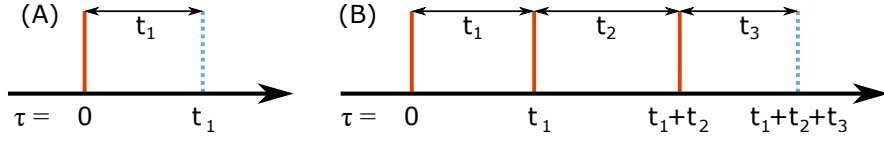


**Figure 2.1** – Interaction sequence to visualize the relevant delays. (A) Experiment with one interaction. (B) Experiment with three interactions. Red: Interactions between light and molecule. Blue dotted: Point in time of signal detection.

matrix is assumed to be in an equilibrium state without time evolution before the first interaction,  $t_0 \rightarrow -\infty$  and  $\rho(t_0) = \rho_0$ .

$$P^{(0)}(t) = \text{const.} \quad (2.22)$$

$$P^{(1)}(t) = \frac{i}{\hbar} \int_{-\infty}^t d\tau_1 E(\tau_1) \langle \mu(t) [\mu(\tau_1), \rho_0] \rangle \quad (2.23)$$

$$P^{(2)}(t) = \frac{1}{\hbar} \int_{-\infty}^t d\tau_2 \int_{-\infty}^{\tau_2} d\tau_1 E(\tau_2) E(\tau_1) \cdot \langle \mu(t) [\mu(\tau_2), [\mu(\tau_1), \rho_0]] \rangle \quad (2.24)$$

$$P^{(3)}(t) = -\frac{i}{\hbar} \int_{-\infty}^t d\tau_3 \int_{-\infty}^{\tau_3} d\tau_2 \int_{-\infty}^{\tau_2} d\tau_1 E(\tau_3) E(\tau_2) E(\tau_1) \cdot \langle \mu(t) [\mu(\tau_3), [\mu(\tau_2), [\mu(\tau_1), \rho_0]]] \rangle \quad (2.25)$$

The  $n$ th order of  $P$  is the polarization that is generated through  $n$  interactions between the molecule and the electric field. The  $\tau_n$  are points in time of the corresponding interaction between molecule and electric field. Without loss of generality, the first interaction time is defined as  $\tau_1 = 0$ . The times between interactions are defined as  $t_n = \tau_{n+1} - \tau_n$ , as it is depicted for  $n = 1$  and  $n = 3$  in figure 2.1.

While  $P^{(0)}$  is a constant dipole moment and thus does not emit any radiation,  $P^{(2)}(t)$  vanishes in isotropic materials, as it is the case for liquid samples. In this work, the main focus is kept on  $P^{(1)}(t)$  and especially  $P^{(3)}(t)$ , which is responsible for the emission of the signal in a FWM spectroscopy experiment. By changing from absolute points in time  $\tau_n$  to relative delays  $t_n$ , equations 2.23 and 2.25 can

be rewritten with the so called molecular response function  $R^{(n)}$  as

$$P^{(1)}(t) = \int_0^\infty dt_1 E(t-t_1) R^{(1)}(t_1) \quad (2.26)$$

$$R^{(1)}(t_1) \propto i \langle \mu(t_1) [\mu(0), \rho_0] \rangle \quad (2.27)$$

$$P^{(3)}(t) = \int_0^\infty dt_3 \int_0^\infty dt_2 \int_0^\infty dt_1 E(t-t_3) E(t-t_3-t_2) E(t-t_3-t_2-t_1) \cdot R^{(3)}(t_3, t_2, t_1) \quad (2.28)$$

$$R^{(3)}(t_3, t_2, t_1) \propto -i \langle \mu(t_3 + t_2 + t_1) [\mu(t_2 + t_1), [\mu(t_1), [\mu(0), \rho_0]]] \rangle. \quad (2.29)$$

Of course, the electric fields in these equations can be represented by complex numbers and thus  $P^{(1)}(t)$  looks as

$$P^{(1)}(t) = \int_0^\infty dt_1 (\tilde{E}(t-t_1) + \tilde{E}^*(t-t_1)) R^{(1)}(t_1), \quad (2.30)$$

with  $\tilde{E}(t) = E'(t) e^{-i\omega t}$ ,  $\tilde{E}^*$  being its complex conjugate and  $E'(t)$  the envelope of the laser pulse.

### 2.1.3 First-order response function

As a next step, the linear molecular response function  $R^{(1)}(t)$  is considered in more detail. The execution of the commutator together with  $\tau_1 = 0$  and the invariance of the trace under cyclic permutation leads to

$$\begin{aligned} R^{(1)}(t) &\propto i \langle \mu(t) \mu(0) \rho_0 - \mu(t) \rho_0 \mu(0) \rangle \\ &= i \langle \mu(t) \mu(0) \rho_0 \rangle - i \langle \rho_0 \mu(0) \mu(t) \rangle. \end{aligned} \quad (2.31)$$

In the first term of 2.31, the two dipole operators act from the left, i.e. on the ket side of the density matrix, whereas in the second term it is the bra side. Before the interaction, i.e. for negative times, the density matrix is assumed to be in the ground state ( $c_n = 0$  for  $n > 0$ ). Its time evolution between two interactions is given by equation 2.11. In the dipole operator, only the off-diagonal elements, namely the transition dipole elements  $\mu_{nm}$ , ( $n \neq m$ ) describe optical interactions, whereas the diagonal elements  $c_n c_n^*$  indicate static dipoles and are therefore

neglected in the following. For a two-level system, one gets

$$\rho_0 = \begin{pmatrix} 1 & 0 \\ 0 & 0 \end{pmatrix} \quad (2.32)$$

$$\mu = \mu_{01} \begin{pmatrix} 0 & 1 \\ 1 & 0 \end{pmatrix}. \quad (2.33)$$

Plugging them into the first term of equation 2.31 leads to

$$\begin{aligned} i\langle \mu(t_1)\mu(0)\rho_0 \rangle &= i\mu_{01}^2 \left\langle \begin{pmatrix} 0 & 1 \\ 1 & 0 \end{pmatrix} e^{-i\omega_{01}t_1} \begin{pmatrix} 0 & 1 \\ 1 & 0 \end{pmatrix} \begin{pmatrix} 1 & 0 \\ 0 & 0 \end{pmatrix} \right\rangle \\ &= i\mu_{01}^2 \left\langle \begin{pmatrix} 0 & 1 \\ 1 & 0 \end{pmatrix} \begin{pmatrix} 0 & 0 \\ e^{-i\omega_{01}t_1} & 0 \end{pmatrix} \right\rangle \end{aligned} \quad (2.34)$$

$$= i\mu_{01}^2 e^{-i\omega_{01}t_1} \quad (2.35)$$

During this sequence of interaction, time evolution and field emission, the density matrix goes through the following states.

$$\begin{pmatrix} 1 & 0 \\ 0 & 0 \end{pmatrix} \xrightarrow[\mu_0 \rightarrow]{\text{⚡}} \begin{pmatrix} 0 & 0 \\ 1 & 0 \end{pmatrix} \xrightarrow[t_1]{\text{⌚}} \begin{pmatrix} 0 & 0 \\ e^{-i\omega_{01}t_1} & 0 \end{pmatrix} \xrightarrow[\mu_1 \rightarrow]{\text{💡}} \begin{pmatrix} e^{-i\omega_{01}t_1} & 0 \\ 0 & 0 \end{pmatrix} \quad (2.36)$$

The small arrows next to the  $\mu_i$  indicate from which side, the operator is applied. Lightning, alarm clock and light bulb in this depiction represent an interaction with the electric field, a time evolution and the signal emission, respectively.

The second term of equation 2.31 gives the complex conjugate of the first term and thus

$$R^{(1)}(t_1) \propto ie^{-i\omega_{01}t_1} - ie^{+i\omega_{01}t_1} \propto \sin(\omega_{01}t_1) \quad (2.37)$$

Plugging equation 2.37 into 2.30 and assuming a resonant excitation ( $\omega = \omega_{01}$ ) yields

$$\begin{aligned} P^{(1)}(t) &\propto \int_0^\infty dt_1 E'(t-t_1) (e^{-i\omega(t-t_1)} + e^{i\omega(t-t_1)}) (ie^{-i\omega t_1} - ie^{i\omega t_1}) \\ &= ie^{-i\omega t} \int_0^\infty dt_1 E'(t-t_1) (1 - e^{i2\omega t_1}) \\ &\quad + ie^{i\omega t} \int_0^\infty dt_1 E'(t-t_1) (e^{-i2\omega t_1} - 1) \end{aligned} \quad (2.38)$$

The macroscopic first-order polarization  $P^{(1)}(t)$  consists of four summands. The high frequency oscillatory nature ( $2\omega$ ) of the second and the third summand makes the integral negligibly small compared to the first and fourth term, which solely consist of the envelope of the electric field. Neglecting the oscillatory terms is called rotating wave approximation and yields a convolution of the electric field envelope with a sine function for the first-order polarization.

$$P^{(1)}(t) \propto \int_0^\infty dt_1 E'(t - t_1) \sin(\omega t) \quad (2.39)$$

As a conclusion it can be said, that an interaction between the ket part of the density matrix and  $\tilde{E}(t)$  leads to a  $\rho_{10}$  coherence (a non-zero matrix element  $\rho_{10}$ , equation 2.34), whereas an interaction between the bra of the density matrix and the complex conjugated  $\tilde{E}^*(t)$  yields a  $\rho_{01}$  coherence. The pathway from  $\rho_{00}$  to  $\rho_{10}$  and back into the ground state  $\rho_{00}$ , that the density matrix undergoes is called Feynman pathway. For the linear case, there is only one Feynman pathway and its complex conjugate that survive the rotating wave approximation.

$$\tilde{E}(t) : \rho_{00} \longrightarrow \rho_{10} \longrightarrow \rho_{00} \quad (2.40)$$

$$\tilde{E}^*(t) : \rho_{00} \longrightarrow \rho_{01} \longrightarrow \rho_{00} \quad (2.41)$$

The generation of non-zero values in the off-diagonal elements of the density matrix, namely a coherence, results in an oscillating term in the macroscopic polarization (equation 2.39). This, on the other hand, gives, according to the Maxwell equations, rise to an emission of radiation. The radiation that is emitted by the first order polarization  $P^{(1)}$  is called free induction decay (FID).

#### 2.1.4 Dephasing and Bloch picture

So far, only isolated molecules were considered. However, in a real experiment, typically an ensemble of molecules is investigated and all of them are influenced by their surroundings, e.g. the solvent, container surfaces and other molecules. For that reason, they do not all have identical energy levels  $\hbar\omega$ , but show a distribution  $p(\omega)$ . The resulting density matrix for the ensemble is the average of all single molecule density matrices.

Right after an interaction with an electric field, the contributions to the coherence terms  $\rho_{01}$  or  $\rho_{10}$  of each molecule oscillate in phase, but with time passing, they

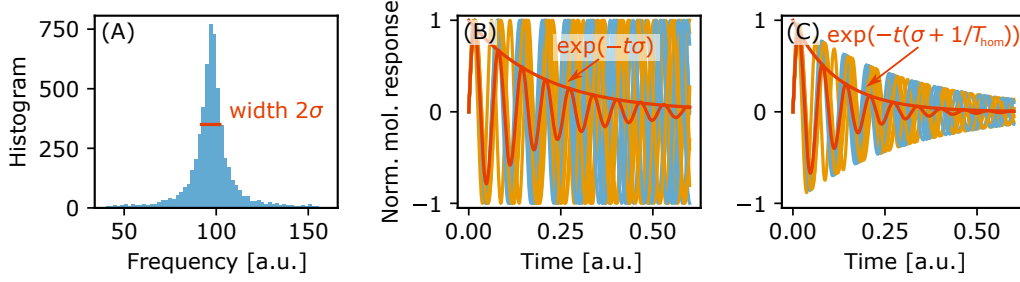


**Figure 2.2** – Inhomogeneous dephasing of the molecular response of an ensemble of 6000 molecules with a Lorentzian frequency distribution. (A) Histogram of frequencies with Lorentzian shape and width  $\sigma$ . (B) Red: Average of 6000 oscillators, that decays with  $e^{-t/T_{\text{inh}}} = e^{-t\sigma}$ . Blue and yellow: Ten randomly chosen single oscillators. (C) Same plot as (B), but each individual oscillator is considered to have an additional damping factor  $e^{-t/T_{\text{hom}}}$ .

lose their phase correlation and interfere destructively. Depending on the shape of the frequency distribution, this leads to different dephasing behaviors in the time domain. The case of a Lorentzian distribution, which in literature is often used to model this decay of the off-diagonal terms of the density matrix (Hamm and Zanni, 2011), is illustrated in figure 2.2. Here, a Lorentzian frequency distribution with width  $\sigma$  (subfigure (A)) is assumed for the sinusoidal behavior of each of the 6000 single molecular coherence terms, that are considered for this visualization. The average is plotted in red in figure 2.2 (B) together with 10 of the 6000 single molecule contributions (blue and yellow).

Mathematically, in the frequency space, this average is identical to a convolution of the distribution  $p(\omega)$  with the  $\delta$ -distribution of a single molecule. If a Lorentzian is assumed, a Fourier transform (FT) leads to an oscillatory term multiplied with an exponential decay in the time space.

$$\int_{-\infty}^{\infty} \delta(\omega) p_{\text{Lor}}(\omega - \omega_0) d\omega \xrightarrow[\text{transform}]{\text{Fourier}} e^{-i\omega_0 t} e^{-t/T_{\text{inh}}} \quad (2.42)$$

This loss of coherence is called inhomogeneous dephasing and the corresponding time constant  $T_{\text{inh}}$  is proportional to the inverse of the width  $\sigma$  of the Lorentzian.

$$\rho_{10}(t) \propto e^{-i\omega t} e^{-t/T_{\text{inh}}} = e^{-i\omega t} e^{-t\sigma}. \quad (2.43)$$

Note that in this example every individual molecule retains its complete amplitude and phase behavior. It is only the average coherence that decreases with time. This picture ignores, however, that the oscillatory nature of  $R^{(1)}$  leads to an emission of the FID and – to fulfill energy conservation – to an exponential decay of itself. For that reason, figure 2.2 (B) is not a realistic scenario and only helps to understand inhomogeneous dephasing.

If a homogeneous decay, i.e. a decay of the coherence term of every individual molecule with a time constant  $T_{\text{hom}}$  is considered together with an inhomogeneous frequency distribution the two decay times add up like

$$\frac{1}{T_2^*} = \frac{1}{T_{\text{hom}}} + \frac{1}{T_{\text{inh}}}. \quad (2.44)$$

The time constant  $T_2^*$  is called pure dephasing time and is not to be mistaken with the dephasing time  $T_2$ , which is discussed a bit later in the text (equation 2.50). The simultaneous presence of homogeneous and inhomogeneous dephasing is depicted in figure 2.2 (C).

A convenient way to visualize the effect of an inhomogeneous distribution on the evolution of an ensemble of dipoles in a two-level system are Bloch vectors.

$$\begin{aligned} B_z(t) &= c_0(t)c_0^*(t) - c_1(t)c_1^*(t) \\ B_x(t) &= i(c_0(t)c_1^*(t) - c_0^*(t)c_1(t)) \\ B_y(t) &= c_0(t)c_1^*(t) + c_0^*(t)c_1(t) \end{aligned} \quad (2.45)$$

The value of the  $z$ -axis that is the difference in population of the excited and the ground state and the  $x$ - and  $y$ -axis represent the coherence between the two states.

If a statistical ensemble is the subject of investigation, one has to consider the average of all individual vectors. This can also be expressed in terms of density matrix components.

$$\begin{aligned} \overline{B}_z(t) &= \rho_{00} - \rho_{11} \\ \overline{B}_x(t) &= -(\rho_{01} + \rho_{10}) \\ \overline{B}_y(t) &= i(\rho_{01} - \rho_{10}) \end{aligned} \quad (2.46)$$

The overline indicates the statistical average. According to equations 2.34 and 2.37, in a scenario with one interaction, the molecular response  $R^{(1)}(t)$  is propor-



tional to the  $x$ -component of the average Bloch vector  $\overline{B}$ .

$$R^{(1)}(t) \propto \overline{B}_x(t) \quad (2.47)$$

Before the interaction with the laser pulse the Bloch vector components are

$$B(t < 0) = (B_x, B_y, B_z) = (0, 0, 1). \quad (2.48)$$

An interaction with the electric field rotates the vector by an angle, that depends on the field strength of the pulse, in the  $zy$ -plane. Afterwards, the time evolution in the Bloch representation corresponds to a rotation around the  $z$ -axis (see equations 2.45 and 2.6), which is identical to a response of the molecule (equation 2.47). This consequently yields an oscillatory macroscopic polarization of the sample and ultimately the emission of an electric field.

Population relaxation, meanwhile, is displayed by an increase of  $c_0$  and a decrease of  $c_1$  or a motion of the vector towards the ground state  $B = (0, 0, 1)$ , to stay in the Bloch vector picture. In the absence of dephasing, the vector of a single molecule always has length one, which is why this picture is also sometimes referred to as the Bloch sphere.

Figure 2.3 shows the case of an inhomogeneous ensemble of molecules, each is represented by its own Bloch vector (yellow), whose average (red) displays the ensemble density matrix. The interaction rotates all vectors in the  $zy$ -plane and immediately they start to rotate around  $B_z$  along the yellow circle with their individual angular velocity  $\omega_i$ . This leads to a separation of the individual Bloch vectors and a spiral motion of the average towards the  $z$ -axis (red spiral). The blue arrow shows the projection of the average Bloch vector on the  $xy$ -plane to depict the decrease of the linear response  $R^{(1)} \propto \overline{B}_x$  due to inhomogeneous dephasing.

In this example, the molecules do not undergo population relaxation,  $B_z$  is constant. However, as already stated earlier, ignoring a decay of the single molecule coherence violates energy conservation. For that reason, it is necessary to introduce a population relaxation, which is described with an exponential decay with the time constant  $T_1$  through

$$\begin{aligned} \rho_{11}(t) &= \rho_{11}(0)e^{-t/T_1} \\ \rho_{00}(t) &= 1 - \rho_{11}(t). \end{aligned} \quad (2.49)$$

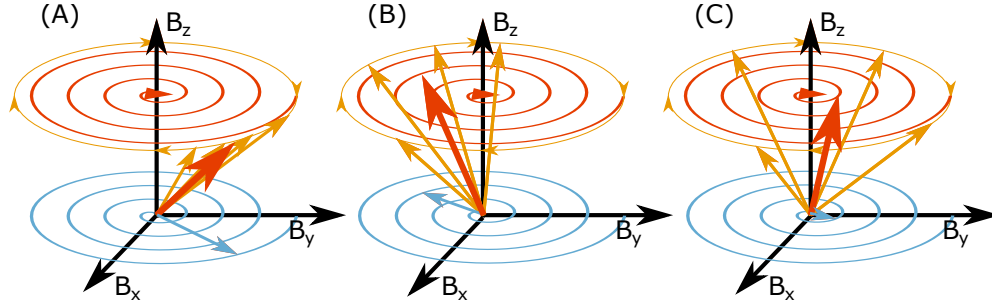


**Figure 2.3** – Illustration of Bloch vectors of four inhomogeneously distributed molecules with different energy levels  $\hbar\omega_i$ . Yellow: individual Bloch vectors. Red: average vector. Blue: projection of average on  $xy$ -plane, to depict the molecular response  $R^{(1)} \propto \bar{B}_x$ . (A) Immediately after interaction with an electric field. (B) and (C) Inhomogeneous dephasing with time passing. There is no population relaxation in this example,  $B_z = \text{const.}$

Since  $\rho_{11} = c_1 c_1^* < c_0 c_0^* = \rho_{00}$ , population relaxation, i.e. an increase of  $c_0 c_0^*$  leads to a decrease of the coherence terms  $c_0 c_1^*$  and  $c_1^* c_0$ . In the Bloch formalism, this is depicted as a motion of the vector along the sphere towards the ground state ( $B_z = 1$ ).

The quantitative correlation between the population relaxation time  $T_1$  and the overall decoherence time  $T_2$  is given via the pure dephasing time  $T_2^*$ , that was already introduced in equation 2.44.

$$\frac{1}{T_2} = \frac{1}{2T_1} + \frac{1}{T_2^*} \quad (2.50)$$

$T_2^*$  describes all dephasing processes that do not occur due to population relaxation. The upper limit for the dephasing time  $T_2$  of an ensemble of molecules is  $2T_1$ . As soon as pure dephasing processes, like inhomogeneous dephasing come into play,  $T_2$  gets even smaller.

As a general remark, it has to be said that the approximation that in the density matrix picture was done by only looking at the first expansion order of  $\rho$  results in  $\rho_{11} = 0$  and  $\rho_{00} \approx 1$ , after one interaction. However, a rotation of the Bloch vectors through an interaction leads to  $B_z < 1$  and thus  $|c_1|^2 > 0$ . This mismatch is resolved by allowing only very small angles between the Bloch vector and  $B_z$ , if only the first order of the density matrix is considered. Like that,  $B_z \approx 1$  is fulfilled.

### 2.1.5 Third-order response function

So far, one interaction between light and matter was considered. This corresponds to the first order of the macroscopic polarization  $P^{(1)}$ , as described in equation 2.26. For FWM spectroscopy however, the third order polarization  $P^{(3)}$  is the measure of interest. This case is mathematically described by equation 2.28 and will be discussed in this section.

The interaction sequence for an experiment with three pulses and the denotation of the relevant delays is sketched in figure 2.1 (B). As before in section 2.1.3, every of the three interactions can take place either on the ket or on the bra side of the density matrix and thus, the rotating wave approximation suppresses either the  $E^*(t)$  or the  $E(t)$  contribution in the response function. By executing the commutators in equation 2.29, it can be found that  $R^{(3)}$  looks like

$$\begin{aligned}
 R^{(3)}(t_3, t_2, t_1) = & \\
 & i\langle\mu_3\mu_1\rho_{-\infty}\mu_0\mu_2\rangle - i\langle\mu_2\mu_0\rho_{-\infty}\mu_1\mu_3\rangle \Rightarrow R_1 + R_1^* \\
 & + i\langle\mu_3\mu_2\rho_{-\infty}\mu_0\mu_1\rangle - i\langle\mu_1\mu_0\rho_{-\infty}\mu_2\mu_3\rangle \Rightarrow R_2 + R_2^* \\
 & + i\langle\mu_3\mu_0\rho_{-\infty}\mu_1\mu_2\rangle - i\langle\mu_2\mu_1\rho_{-\infty}\mu_0\mu_3\rangle \Rightarrow R_4 + R_4^* \\
 & + i\langle\mu_3\mu_2\mu_1\mu_0\rho_{-\infty}\rangle - i\langle\rho_{-\infty}\mu_0\mu_1\mu_2\mu_3\rangle \Rightarrow R_5 + R_5^*. \quad (2.51)
 \end{aligned}$$

As in the case of  $R^{(1)}$  with only one interaction (see section 2.1.3), these terms are called Feynman pathways and by convention, they are labelled with the notations  $R_1, R_2, R_4, R_5$  and their complex conjugates  $R_i^*$ . In equation 2.51, only pathways that appear in a two-level system are considered.

The Feynman pathways that conventionally are labelled as  $R_3, R_6$  and their complex conjugates create coherences with a second excited state.

$$\begin{aligned}
 & i\langle\mu_3\mu_2\mu_1\rho_{-\infty}\mu_0\rangle - i\langle\mu_0\rho_{-\infty}\mu_1\mu_2\mu_3\rangle \Rightarrow R_3 + R_3^* \\
 & + i\langle\mu_3\mu_2\mu_0\rho_{-\infty}\mu_1\rangle - i\langle\mu_1\rho_{-\infty}\mu_0\mu_2\mu_3\rangle \Rightarrow R_6 + R_6^* \quad (2.52)
 \end{aligned}$$

Exemplary, the evolution of the density matrix in the case of an  $R_4$  and  $R_1$  pathway is shown for a two-level system. Starting in the ground state, dipole operators and time evolutions are applied to  $\rho_0$  from the side defined in equations 2.51. The small arrows next to the  $\mu_i$  indicate from which side, the operator is applied. Lightning, alarm clock and light bulb depict an interaction with the electric field, time evolution and signal emission, respectively. The last step corresponds to the

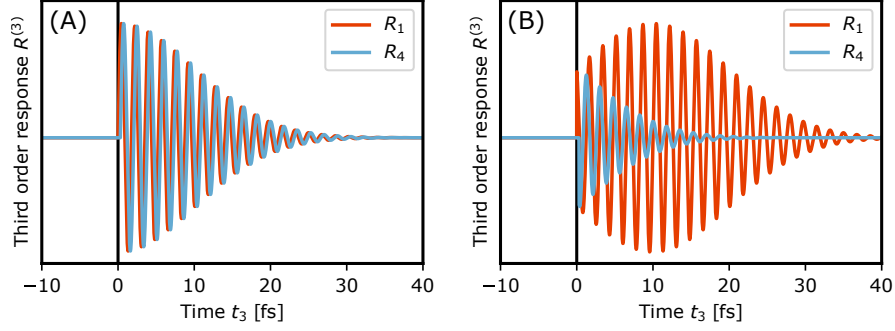


**Figure 2.4** – Third order response of rephasing (red) and non-rephasing (blue) pathways for an inhomogeneous Gaussian distribution of frequencies  $\omega_{01}$ .  $R^{(3)}$  only occurs after the third interaction at  $t_3 = 0$ . (A) Response function for  $t_1 = 0$ . Rephasing and non-rephasing pathways are indistinguishable. (B) Response function for  $t_1 = 10$  fs.

trace, in order to get the macroscopic polarization  $P^{(3)}$ .

$$\begin{aligned}
 R_4 : \quad & \begin{pmatrix} 1 & 0 \\ 0 & 0 \end{pmatrix} \xrightarrow[\leftarrow \mu_0]{\text{light}} \begin{pmatrix} 0 & 0 \\ i & 0 \end{pmatrix} \xrightarrow[t_1]{\text{clock}} \begin{pmatrix} 0 & 0 \\ ie^{-i\omega_{01}t_1} & 0 \end{pmatrix} \xrightarrow[\leftarrow \mu_1]{\text{light}} \begin{pmatrix} 0 & 0 \\ 0 & ie^{-i\omega_{01}t_1} \end{pmatrix} \\
 & \xrightarrow[\leftarrow \mu_2]{\text{light}} \begin{pmatrix} 0 & 0 \\ ie^{-i\omega_{01}t_1} & 0 \end{pmatrix} \xrightarrow[t_3]{\text{clock}} \begin{pmatrix} 0 & 0 \\ ie^{-i\omega_{01}(t_1+t_3)} & 0 \end{pmatrix} \xrightarrow[\mu_3 \rightarrow]{\text{light}} \begin{pmatrix} ie^{-i\omega_{01}(t_1+t_3)} & 0 \\ 0 & 0 \end{pmatrix} \\
 & \xrightarrow{\langle \dots \rangle} ie^{-i\omega_{01}(t_1+t_3)} \quad (2.53)
 \end{aligned}$$

$$\begin{aligned}
 R_1 : \quad & \begin{pmatrix} 1 & 0 \\ 0 & 0 \end{pmatrix} \xrightarrow[\leftarrow \mu_0]{\text{light}} \begin{pmatrix} 0 & i \\ 0 & 0 \end{pmatrix} \xrightarrow[t_1]{\text{clock}} \begin{pmatrix} 0 & ie^{i\omega_{01}t_1} \\ 0 & 0 \end{pmatrix} \xrightarrow[\mu_1 \rightarrow]{\text{light}} \begin{pmatrix} 0 & 0 \\ 0 & ie^{i\omega_{01}t_1} \end{pmatrix} \\
 & \xrightarrow[\leftarrow \mu_2]{\text{light}} \begin{pmatrix} 0 & 0 \\ ie^{i\omega_{01}t_1} & 0 \end{pmatrix} \xrightarrow[t_3]{\text{clock}} \begin{pmatrix} 0 & 0 \\ ie^{-i\omega_{01}(t_3-t_1)} & 0 \end{pmatrix} \xrightarrow[\mu_3 \rightarrow]{\text{light}} \begin{pmatrix} ie^{-i\omega_{01}(t_3-t_1)} & 0 \\ 0 & 0 \end{pmatrix} \\
 & \xrightarrow{\langle \dots \rangle} ie^{-i\omega_{01}(t_3-t_1)} \quad (2.54)
 \end{aligned}$$

During  $t_2$ , between the interactions with  $\mu_1$  and  $\mu_2$ , the system in either case is in a population state and the off-diagonal elements are 0. Thus, according to equation 2.11, the system does not evolve during that time.

To simulate an inhomogeneously broadened ensemble of molecules, the results of

the evolutions in equations 2.53 and 2.54 are convoluted with a Gaussian distribution of frequencies around  $\overline{\omega_{01}}$  and with a width  $\Delta\omega_{01}$ . Choosing a Gaussian frequency distribution other than e.g. a Lorentzian one fits better, if the broadening is mainly driven by the Doppler effect. This is the case for samples in the liquid phase and thus suits best as a theoretical approach for this work (Bransden and Joachain, 1998).

$$R_4 : \quad i \int d\omega_{01} e^{-\frac{(\omega_{01}-\overline{\omega_{01}})^2}{2\Delta\omega_{01}^2}} e^{-i\omega_{01}(t_3+t_1)} \quad (2.55)$$

$$R_1 : \quad i \int d\omega_{01} e^{-\frac{(\omega_{01}-\overline{\omega_{01}})^2}{2\Delta\omega_{01}^2}} e^{-i\omega_{01}(t_3-t_1)} \quad (2.56)$$

Switching into the time space by the application of an FT leads to

$$R_4 : \quad i e^{-\Delta\omega^2(t_3+t_1)^2/2} e^{-i\omega_{01}(t_3+t_1)} \quad (2.57)$$

$$R_1 : \quad i e^{-\Delta\omega^2(t_3-t_1)^2/2} e^{-i\omega_{01}(t_3-t_1)}. \quad (2.58)$$

The third order response for  $R_1$  and  $R_4$  is displayed in figure 2.4. Subfigure (A) shows the case of  $t_1 = 0$ , where both pathways are indistinguishable. For  $t_1 > 0$ , however, the phase of the oscillation differs, which is due to the difference in the second exponent in equations 2.57 and 2.58. Besides that, the peak position of the envelope shifts into opposite directions for both contributions (figure 2.4 (B)). Since the presence of all three interactions is mandatory for a third order response,  $R^{(3)} > 0$  only for  $t_3 > 0$ .

The emission of the signal in the case of  $R_1$  is not instantaneous after the third pulse, but delayed by  $t_1$ . This effect is called photon echo and we talk about a rephasing pathway in the case of  $R_1$ , whereas  $R_4$  is called non-rephasing. It can be shown, that  $R_2$  and  $R_5$  are rephasing and non-rephasing, respectively, as well.

A more figurative explanation for the appearance of a photon echo is given by the Bloch vector picture. Figure 2.5 shows the projection of Bloch diagrams on the  $xy$ -plane for the evolution of an inhomogeneous ensemble of four molecules during a rephasing FWM spectroscopy experiment.

Before the first interaction, all molecules are in the ground state and  $\overline{B}_z = 1$ . In figure 2.5 (A), this is illustrated with the filled circle. The first interaction creates a coherence and rotates the vectors in the  $yz$ -plane. During the time  $0 < t < t_1$  they oscillate clockwise around  $B_z$  according to equations 2.45.

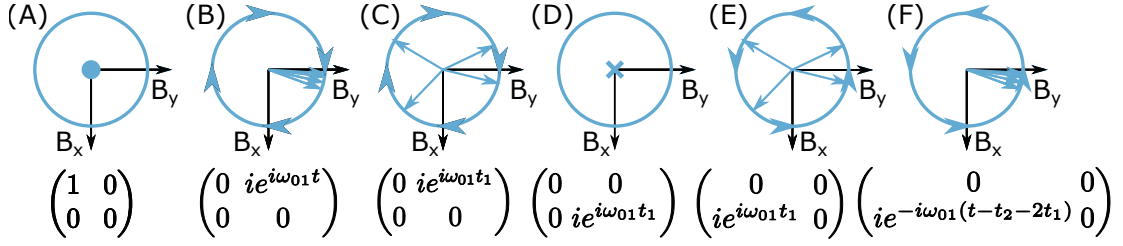


**Figure 2.5** – Bloch vector evolution of rephasing pathway for an inhomogeneously broadened ensemble of four emitters. A projection on the  $xy$ -plane is shown. Filled circle: Vectors pointing in the positive  $z$ -direction. Cross: Vectors pointing in the negative  $z$ -direction. Bottom line: Respective density matrix. (A)  $t < 0$ : All molecules are in the ground state,  $B_z = 1$ . (B)  $0 < t < t_1$ : Immediately after the first interaction, all molecules are in phase. Clockwise oscillation around  $B_z$ . Start of dephasing process. (C)  $t = t_1$ : Moment of the second interaction, dephasing process has proceeded. (D)  $t_1 < t < t_1 + t_2$ : After the second interaction,  $B_z = -1$ . No coherence dynamics, phase is preserved. (E)  $t = t_1 + t_2$ : The moment after the second interaction, the phase is identical to (C), but the vectors rotate counterclockwise now. (F)  $t_1 + t_2 < t < 2t_1 + t_2$ : Rephasing process due to counterclockwise rotation and photon echo at  $t = 2t_1 + t_2$ , or  $t_3 = t_1$ .

As the transition frequencies show inhomogeneous broadening, the vectors rotate with different angular frequencies  $\omega_i$  (B). With time passing, the inhomogeneity of the frequency distribution leads to a dephasing until the moment of the second interaction at  $t = t_1$ . Note that each individual vector's phase is still well defined, it is only the average that dephases (C). The second interaction rotates the vectors towards the  $B_z$ -direction with  $B_z = -1$ . The excited state is now populated and no phase dynamics occur during  $t_1 < t < t_1 + t_2$ . However, the phase of the vectors is preserved (D).

After the third interaction, at  $t = t_1 + t_2$  all Bloch vectors point in the same directions, as immediately before the second interaction (E). Since the density matrix switched from a coherence in  $\rho_{01}$  to  $\rho_{10}$  with the pulses 2 and 3 (compare with equation 2.54), the oscillation direction is now reversed. The molecular energy levels and thus the absolute value of the angular frequency  $\omega_i$  of each individual arrow remains unchanged, which is the reason for the rephasing process during  $t_1 + t_2 < t < t_1 + t_2 + t_3$ . At  $t_3 = t_1$ , the rephasing process is complete and all vectors point into the same direction  $B_y$  again. This leads to an oscillating macroscopic polarization and ultimately to the emission of a field with the echo delay  $t_1$ .

### 2.1.6 Link to molecular response: the susceptibility

The link between the third order polarization and molecular properties such as optical transitions can be shown by transforming equation 2.28 into the frequency space

$$P^{(3)}(t) \propto \int_0^\infty d\omega_3 \int_0^\infty d\omega_2 \int_0^\infty d\omega_1 \chi^{(3)}(\omega_S, \omega_1, \omega_2, \omega_3) \cdot E(\omega_1)E(\omega_2)E(\omega_3)e^{-i\omega_S t}, \quad (2.59)$$

with  $\omega_S = \pm\omega_1 \pm \omega_2 \pm \omega_3$  being the signal frequency and the signs depending on the considered Feynman pathway (Mukamel, 1995).

The  $n$ th order susceptibility  $\chi^{(n)}$  is a tensor of rank  $n + 1$ , which correlates a material response at frequency  $\omega_S$ , namely the macroscopic polarization, with  $n$  light field interactions at frequencies  $\omega_i$  ( $i = 1, 2, \dots, n$ ). In this respect, off-diagonal elements of  $\chi^{(n)}$  report on the presence of intramolecular interactions and couplings between different molecular states.

In the case of  $n = 3$ , which will mainly be considered in this work, it is thus three interactions between a molecule and an electric field  $E(\omega_i)$ , ( $i = 1, 2, 3$ ) that lead to an emission of a fourth electric field  $E(\omega_S)$ . Since four electric field interactions are involved when investigating  $\chi^{(3)}$ , such experiments are often referred to as four-wave mixing (FWM) spectroscopy.

### 2.1.7 Semi-impulsive limit and phase matching

If the semi-impulsive limit from equation 2.3 is applied to the third order polarization in equation 2.28, the integrals can be solved to get

$$P^{(3)} \propto E_0^3 e^{i(\mp\omega_1 \mp \omega_2 \mp \omega_3)t} e^{i(\pm \vec{k}_1 \pm \vec{k}_2 \pm \vec{k}_3) \cdot \vec{r}} e^{i(\pm\varphi_1 \pm \varphi_2 \pm \varphi_3)} \sum_m R_m^{(3)}, \quad (2.60)$$

with the subscript  $m$  indicating the Feynman pathway.

Due to the rotating wave approximation, that was described and applied in section 2.1.3, each of the pathways  $R_m$  is generated by a specific sequence of three interactions with either  $\tilde{E} \propto e^{-i\omega t}$  or  $\tilde{E}^* \propto e^{+i\omega t}$ . The type of interaction thus defines the signs in the exponents of the exponential functions in equation 2.60. On the pathway  $R_1^{(3)}$ , the density matrix interacts with  $\tilde{E}_1^*$ ,  $\tilde{E}_2$  and  $\tilde{E}_3$ , while on pathway  $R_4^{(3)}$  it is  $\tilde{E}_1$ ,  $\tilde{E}_2^*$  and  $\tilde{E}_3$ . This leads to the following equations for the

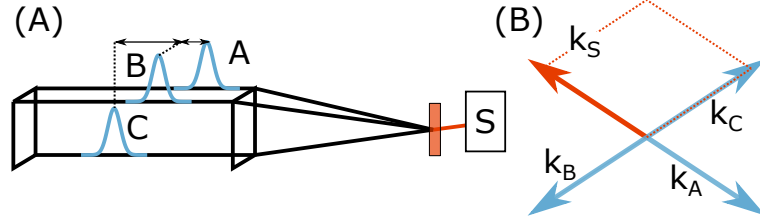


**Figure 2.6** – Depiction of the box-CARS geometry. (A) Real space schematic of box-CARS. The beams A, B and C propagate along distinct corners of a rectangle and are focused on one spot in the sample. With a suitable time ordering, e.g.  $\tau_A < \tau_B < \tau_C$ , a third order signal will be emitted into the direction of the fourth corner (red) and can be detected by a spectrometer S. (B) Projection of wave vectors of the beams A, B, C and signal on a plane perpendicular to the direction of propagation. According to  $k_S = -k_A + k_B + k_C$ , the rephasing signal is emitted towards the fourth corner of the rectangle and is thus phase matched. Red dotted lines: Sum of the vectors to get  $k_S$ .

wave vector, the frequency and the phase of the signal field.

$$\begin{aligned}
 R_1 : \quad \vec{k}_S &= -\vec{k}_1 + \vec{k}_2 + \vec{k}_3 \\
 \omega_S &= -\omega_1 + \omega_2 + \omega_3, \\
 \varphi_S &= -\varphi_1 + \varphi_2 + \varphi_3
 \end{aligned} \tag{2.61}$$

$$\begin{aligned}
 R_4 : \quad \vec{k}_S &= +\vec{k}_1 - \vec{k}_2 + \vec{k}_3, \\
 \omega_S &= +\omega_1 - \omega_2 + \omega_3 \\
 \varphi_S &= +\varphi_1 - \varphi_2 + \varphi_3
 \end{aligned} \tag{2.62}$$

It can be seen that, if the laser pulses that are responsible for the three interactions are collinear, rephasing and non-rephasing contributions to  $P_m^{(3)}$  will emit a signal into the same direction and it will be impossible to discriminate between them geometrically.

In the non-collinear case, however,  $\vec{k}_1 \neq \vec{k}_2 \neq \vec{k}_3$  and thus different Feynman pathways are emitted in different directions. Consequently, if a clear time ordering of the interactions is given (pulses 1 and 2 do not overlap in time), one can select the rephasing or the non-rephasing signal by placing the detector in one or the other direction. If pulses 1 and 2 do overlap, it is not clear, which of the pulses interacts first with the molecule and the emitted signal will contain information of both pathways.



The considerations for equations 2.61 and 2.62 resemble momentum and energy conservation. Both demands are satisfied in the so called box-CARS geometry, which is presented in figure 2.6. All three pulses propagate on parallel trajectories that are situated in the corners of a rectangle and are then focused on one point in the sample (A). The notations A, B and C indicate a geometrical position of a certain beam, whereas the previously used 1, 2 and 3 refer to an ordering of light-molecule interactions in time. By changing the time ordering, any of the beams  $\{A, B, C\}$  might be responsible for one of the interactions  $\{1, 2, 3\}$ .

The same rectangular shape is given in a projection of the  $k$ -vectors on a plane that is perpendicular to the direction of propagation (figure 2.6 B). For the time ordering  $\tau_A < \tau_B < \tau_C$ , the rephasing signal will be emitted into the direction  $k_S = -k_A + k_B + k_C$ , which is the fourth corner of the rectangle and momentum, as well as energy conservation are fulfilled. The box-CARS geometry will be discussed in more detail in section 2.2.3.

## 2.2 Experimental realizations

Section 2.1 introduced the reader to the formalism and theory of FWM spectroscopy and concludes with different Feynman pathways that contribute to the overall emitted signal field. Based on these findings, several experimental geometries for the optical regime were developed, some of which will be presented in the following. Basically, they can be classified into two categories, namely frequency and time domain approaches.

### 2.2.1 Frequency domain spectroscopy

In frequency domain spectroscopy, a narrow-band pulse excites the sample and a broad-band second pulse is used as a probe (figure 2.7 (B)). The pump frequency is then tuned through the spectral range of interest using for example an etalon (Hamm et al., 1998) or a spatial light modulator (SLM) (Shim et al., 2007). The first two interactions between molecules and light happen during the first pulse, whereas the third interaction is due to the second one. This implies  $\vec{k}_1 = \vec{k}_2$  and selecting rephasing or non-rephasing pathways through phase matching is impossible, since they will be emitted into the same direction (equation 2.60). The emitted light is then detected by a spectrometer and one obtains a signal  $S(\omega_{pu}, \omega_S)$ , that depends on the frequency of the pump and of the signal. Ac-

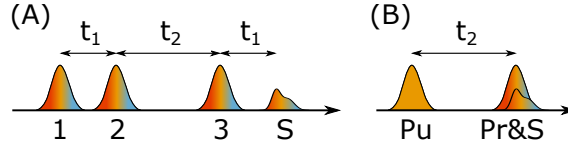


**Figure 2.7** – Pulse sequences in time and frequency domain spectroscopy. (A) Time domain spectroscopy with two broad-band pulses to excite the sample and the signal of a rephasing pathway. (B) Frequency domain spectroscopy with one tunable narrow-band pulse for excitation (Pu) and a broad-band probe pulse (Pr).

According to the number of frequency dimensions, FWM spectroscopy is sometimes also referred to as 2D spectroscopy.

It is important to note that, by selecting the bandwidth of the pump pulse, one has to find a compromise between frequency and time resolution, and it is impossible to optimize both at the same time.

### 2.2.2 Time domain spectroscopy and heterodyne detection

The other approach is time domain spectroscopy, where not one frequency after the other is exciting the sample, but all at the same time. Therefore, two spectrally broad pulses with a well defined delay are needed for the excitation (figure 2.7 (A)). Now, in contrast to frequency domain FWM spectroscopy, the three interactions take place within distinct laser pulses and one is able to modify the delay between them. The time  $t_1$  between the first two pulses determines, which of the frequencies interfere constructively or destructively in the sample and thus, which molecules of the inhomogeneous ensemble are excited. Consequently, shifting one of the two pump pulses in time leads to an excitation with a new set of frequencies. In the case of an inhomogeneous ensemble of molecules, many of the pump frequencies might overlap with an absorption line and lead to the emission of a signal  $S(t_1, \omega_S)$ . The disentanglement of all the frequencies applied simultaneously is then done by an FT along  $t_1$ .

$$S(t_1, \omega_S) \xrightarrow[\text{transform}]{\text{Fourier}} S(\omega_{12}, \omega_S). \quad (2.63)$$

For that reason the field of spectroscopic FWM experiments that follow the time domain approach is also referred to as FT FWM spectroscopy.

The execution of the FT requires precise knowledge of the delay between the first two interactions. This delay, however, for pulses that are not in the Fourier limit,

depends on the interaction wavelengths  $\omega_1$  and  $\omega_2$  (see chapter 4). Accordingly, it is mandatory in FT FWM spectroscopy, that the two exciting pulses have a constant phase, or in other words, are Fourier-limited.

Another necessity of the FT, is to know the amplitude and phase of the signal  $S(t_1, \omega_S)$  and not only the intensity, as measured by a square-law detector. Therefore, people use the concept of heterodyne detection, where a phase-stable beam, also referred to as local oscillator (LO), is mixed with the signal field and then detected spectroscopically.

There are different geometrical beam arrangements that have been used for FT FWM spectroscopy. In a pump-probe geometry, one beam contains a double-pulse, with tunable delay for the first two interactions. Thus they have the same wave vector ( $\vec{k}_1 = \vec{k}_2$ ) and the signal of both, the rephasing and non-rephasing pathways is emitted in the direction of the second beam, which serves for the third interaction and also as the LO.

$$\vec{k}_S = \mp \vec{k}_1 \pm \vec{k}_2 + \vec{k}_3 = \vec{k}_3 \quad (2.64)$$

In a non-collinear scheme like the box-CARS geometry, however, none of the three beams overlaps spatially with the emitted signal and an additional beam has to be added to the setup. Figure 2.8 shows an experimental design of a box-CARS geometry that allows heterodyne detection by including an LO to the fourth corner of the rectangle. In more detail, this is discussed in section 2.2.3.

No matter, how the heterodyne detection is realized experimentally, the measured intensity is the absolute square of the sum of the two superimposed fields and contains the pure quadratic terms from LO and signal, as well as a mixed term.

$$\begin{aligned} I_{\text{het}} &= |E_{\text{LO}} + E_S|^2 \\ &= |E_{\text{LO}}|^2 + |E_S|^2 + 2|E_{\text{LO}}||E_S|\cos(\omega t_{\text{SLO}} + \varphi_{\text{LO}} - \varphi_S), \end{aligned} \quad (2.65)$$

where the subscripts LO and S indicate the local oscillator and the signal, respectively, and  $t_{\text{SLO}}$  is the delay between the two. Such an interference pattern is called interferogram.

Since only the third term of equation 2.65 shows an oscillatory pattern, the first two contributions can be suppressed with a window function in the Fourier space. The third term then contains all the phase information that can be preserved from such an interferogram and  $\varphi_S$  can be extracted if  $t_{\text{SLO}}$  and the phase of the

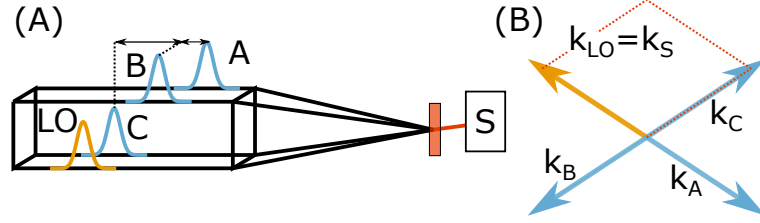


**Figure 2.8** – Depiction of the box-CARS geometry with an LO. (A) Real space schematic of box-CARS. The beams A, B, C and LO propagate along distinct corners of a rectangle and are focused in one spot in the sample. The emitted signal (red) copropagates together with the LO into a spectrometer S. (B) Projection of wave vectors of the beams A, B, C and LO on a plane perpendicular to the direction of propagation. If the signal fulfills  $k_S = -k_A + k_B + k_C$ , it is superimposed with the LO for interferometric detection. Red dotted lines: Sum of the vectors to get  $k_S$ .

LO are well-known. It simplifies the extraction of the signal phase, if the LO is Fourier-limited, since then, no correction for  $\varphi_{LO}$  has to be done.

For the detection of the third term, namely the fringes of an interferogram, phase stability is necessary. As soon as there are fluctuations between  $\varphi_{LO}$  and  $\varphi_S$  during the integration time of the detector, the interference fringes will start to lose contrast. Furthermore, since an FT is performed, a precise control of the delay between the two excitation pulses is – besides phase stability – a second crucial criterion for a successful time domain spectroscopy experiment. Sections 2.2.4 and 2.2.5 treat different experimental realizations to fulfill both requirements.

### 2.2.3 Box-CARS geometry

There are different geometric realizations of FWM spectroscopy experiments, including collinear, partly collinear and non-collinear ones. While detailed descriptions of the most common approaches can be found e.g. in the work of Fuller and Ogilvie (2015), in this section, the so called box-CARS geometry, which belongs to the non-collinear setups, is presented. It was initially implemented in coherent anti-Stokes Raman spectroscopy (CARS) experiments and is sometimes also referred to as boxcar geometry. Basically, it is the arrangement of three beams in the corners of a rectangle. Subsequently they are focused by a lens or concave mirror into the sample. As already explained in section 2.1.7, it allows to generate a phase-matched signal field that satisfies momentum and energy conservation.

Implementing a heterodyne detection scheme in the box-CARS geometry is done

by setting an LO to the fourth corner of the rectangle, as shown in figure 2.8. Subfigure (A) shows the geometry of beams A, B and C (blue) and the LO. All are focused into one point in the sample in a way, that a third order signal is emitted into the direction of the LO. The wave vector space is shown in figure 2.8 (B) with  $\vec{k}_{\text{LO}}$  in yellow and  $\vec{k}_A$ ,  $\vec{k}_B$ ,  $\vec{k}_C$  in blue. By setting up the experimental geometry like that, the wave vector of the LO will be

$$\vec{k}_{\text{LO}} = -\vec{k}_A + \vec{k}_B + \vec{k}_C. \quad (2.66)$$

According to equations 2.61 and 2.62, this yields a mixing of the LO and the rephasing signal for a time ordering  $\tau_A < \tau_B < \tau_C$  and a mixing of LO and the non-rephasing signal for  $\tau_B < \tau_A < \tau_C$ .

Consequently, the box-CARS geometry allows independent heterodyne measurements of the rephasing and the non-rephasing signal, depending on whether beam A or beam B arrives first. In this work, a positive value of  $t_{\text{AB}}$  will refer to  $\tau_A < \tau_B$  and vice versa.

### 2.2.4 Phase stabilization

As mentioned in section 2.2.2, phase stability is a crucial criterion for heterodyne detection. Conventionally, the limit of  $\Delta\varphi < 2\pi/100$  is used for the so called interferometric phase stability. In this section, some techniques to fulfill this requirement are presented.

#### Active phase stabilization

Some of the phase stabilization schemes, that have been developed in the past years are active phase stabilization approaches, where an additional beam, e.g. a HeNe laser is copropagating with the other beams. Like this, long term drifts of the setup can be assessed interferometrically and – via a feedback loop – corrected for with mirrors that are mounted on piezoelectric actuators (Volkov et al., 2005; Zhang et al., 2005). The disadvantages of this kind of technique are the big alignment effort for the second beam and the complicated work on the feedback loop, but – most importantly – that only long term phase drifts can be compensated. The setup is not fast enough to correct for fast fluctuations, like e.g. mechanical vibrations. For that reason, active phase stabilization is mainly suitable for experiments in the near-infrared (NIR) and mid-infrared (MIR).

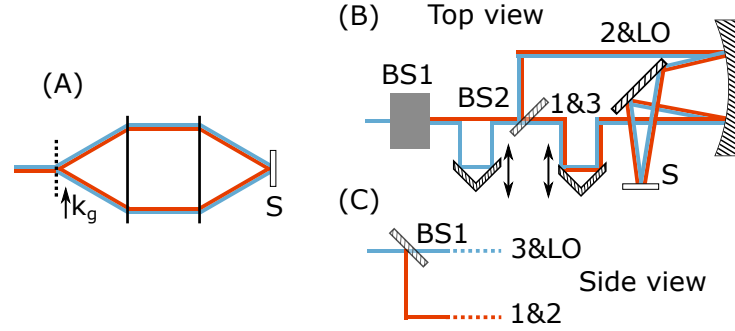


**Figure 2.9** – Passive phase stabilization. Red lines: beams behind figure plane. Blue lines: Beams in figure plane. (A) Conceptual design of approach with diffractive optics. Dotted line: Diffractive beam splitter with the grating vector  $k_g$ . Solid lines: Lenses. S: Sample. (B) Top view of approach without diffractive optics by Selig et al. (2008). BS1 and BS2: 50:50 beam splitter. (C) Side view of same setup as (B).

### Passive phase stabilization

The development towards experiments with shorter wavelengths necessitates other phase stabilization methods and gave rise to passive approaches. They mostly consist of steering all involved pulses through identical optics. In doing so, any mechanical vibrations will result in the same phase jitter for all involved pulses and no differential phase fluctuations will appear. This, however, imposes limitations on the setup implementation and the possibilities of delay control.

A passively phase-stable way to build a non-collinear geometry was in similar ways conceived by Maznev et al. (1998), Goodno et al. (1998) and Brixner et al. (2004). As shown in figure 2.9 (A), they integrate a diffractive grating instead of conventional beam splitters into their setup. They use the first diffraction orders ( $\pm 1$ ) to generate spatially separated duplicates of two incoming beams for a box-CARS geometry. The heterodyned signal then looks like equation 2.65 and in the case of a rephasing experiment has the phase

$$\varphi_{\text{het}} = +\varphi_1 - \varphi_2 - \varphi_3 + \varphi_{\text{LO}}. \quad (2.67)$$

Any phase jitter  $\delta\varphi$  from the diffractive grating is added to all of  $\varphi_1$ ,  $\varphi_2$ ,  $\varphi_3$  and  $\varphi_{\text{LO}}$ . Thus  $\delta\varphi$  contributes twice with a negative and twice with a positive sign to the total phase of the interferogram and this concept is considered passively phase-stable. A conventional beam splitter would add  $\delta\varphi$  with opposite signs to the transmitted and the reflected beam and any fluctuations would lead to a noise

in  $\varphi_{\text{het}}$ . However, the bandwidth of such an experiment with diffractive gratings is limited, since broad spectra lead to an undesired lateral chirp in the beams and bad transmission efficiencies of the grating. They reach delay control by inserting a pair of glass wedges into all beams. This method is in more detail described in section 2.2.5.

A different popular passive technique, which schematically is shown in figure 2.9 (B) and (C), was published by Selig et al. (2008). They use two conventional beam splitters to generate four duplicates, but – by an appropriate design of the setup – steer the beams in pairs through all optics of the experiment, such that any instabilities are induced into two pulses that contribute with opposite sign to the overall phase in equation 2.67. Delay control is accomplished by using standard retroreflectors on translation stages (section 2.2.5).

### 2.2.5 Delay control

In the previous section, some approaches to reduce phase fluctuations down to interferometric stability were presented. This limit, however, also applies for the precision of the delay control ( $< \lambda/100c$ ). Different techniques to fulfill this criterion have been used in the past and in the following, some of them will be presented.

#### Retroreflector on a translation stage

The most common approach to delay control is the implementation of a retroreflector or a single mirror on a linear translation stage. In order to improve the effective resolution and precision of there delay control, Son et al. (2017) tilt the translation direction of the stage with respect to the beam by an angle  $90^\circ - \alpha$ , with  $\alpha \approx 0.3^\circ$ . In doing so, their precision improves by a reduction ratio of  $1/\sin \alpha \approx 190$  compared to a setup, where the translation axis of the stage and the beam are parallel.

Using translation stages though always implies distinct beam paths for every pulse and thus offers a source for differential phase fluctuations. For that reason, more sophisticated phase stabilization measures, like the one of Selig et al. (2008), that was presented in section 2.2.4, have to be applied.

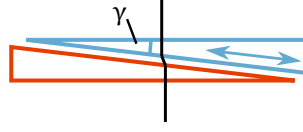


**Figure 2.10** – Pair of anti-parallel glass wedges, where one is fix (red) and one is translatable (blue) for delay control. Black: Beam path.  $\gamma$ : Internal wedge angle

### Glass wedges

Inserting pairs of glass wedges which are aligned anti-parallel with respect to each other, allows to delay a pulse that passes through both wedges by moving one of them (figure 2.10). A small internal wedge angle  $\gamma$  enables a very fine control of the delay due to a large reduction ratio  $1/\sin \gamma$  of the wedge translation. The advantage with respect to the retroreflector on a translation stage is, that all beams can be reflected by the same mirrors and phase fluctuations due to vibrating optics are thus induced into all beams identically. Consequently, there will not be any significant differential phase. However, increasing the amount of glass for one of the pulses, induces a higher order phase and thus makes a simultaneous compression of all pulses impossible. More details on compression of pulses and the effects of material transmission are given in chapter 4.

### Birefringent materials

While the glass wedges for delay control can only be implemented in non-collinear geometries, Brida et al. (2012) developed a similar method with which they generate two collinear pulses with a well-defined delay. They utilize a pair of birefringent wedges, such that a transmitted pulse is polarized by  $45^\circ$  with respect to the optical axis of the material. The wedges are arranged anti-parallel, as depicted in figure 2.10. Due to the different group velocities of the ordinary and extraordinary beam, the result are two collinear pulses with perpendicular polarization and a delay that is determined by the thickness of the birefringent material. This thickness can be varied by moving one of the two wedges in or out. Finally, a polarizer can bring the two pulses back to an identical polarization.

### Adaptive pulse shaping

Different adaptive pulse shapers are used in FT FWM spectroscopy experiments for the generation of double pulse sequences in collinear geometries, as well as for delay control in non-collinear geometries.



In some experiments, the interaction between a radio frequency acoustic wave and an incident optical pulse is used to generate a phase-locked pulse pair with a well-defined delay in an acousto-optic programmable dispersive filter (AOPDF) (Myers et al., 2008; Krebs et al., 2013). This collinear pulse pair then serves as pump pulses in a pump-probe geometry.

SLMs, are devices with a one- or two-dimensional active area, in which the spectral phase and/or the amplitude of a beam can be modulated. Therefore, the incoming light has to be dispersed in a diffractive or refractive way and collimated such that each frequency component's phase can be modulated individually (see e.g. figure 4.5). Different devices have been developed for the spatial modulation of spectral pulse components, amongst them acousto-optic modulators (AOMs), which, as AOPDFs, base on spatial refractive index modulations induced by an acoustic wave, and liquid crystal spatial light modulators (LC SLMs), in which the orientation of birefringent liquid crystals is controlled and thus the refractive index can be tuned. The functional principle of LC SLMs is in more detail described in section 4.1.5.

These devices allow to induce a combination of spectral amplitude and phase shaping, which enable the user to generate a collinear pulse sequence and control the respective delays without the motion of any mechanical parts (von Vacano et al., 2007). This was used for fully collinear experiments (Tian et al., 2003), as well as for the generation of a collinear pulse pair as pump pulses in a pump-probe geometry (Shim et al., 2007; Tseng et al., 2009).

Furthermore, non-collinear experiments have been performed, where an LC SLM with a two-dimensional active area has been used and every beam was manipulated in a distinct area on the device. By inducing a linear spectral phase, a pulse is shifted in time (chapter 4) and consequently, all differential delays can be determined with this approach (Rodriguez et al., 2015; Schlau-Cohen et al., 2012).

### 2.2.6 The approach of this work: single-shot interferometry

All the strategies for phase stabilization and precise delay control that were presented in sections 2.2.4 and 2.2.5 have been proven to work, but also show limitations and none of them is universal. This survey, on the other hand, documents how dynamic the field of FT FWM spectroscopy is. The current frontiers are constantly pushed towards shorter wavelengths like UV (Krebs et al., 2013), XUV

(Bohinc et al., 2019) and even the hard X-ray range (Mukamel et al., 2013), which increases the difficulties in phase stabilization and sets new limitations for the setup design and the selection of strategies. For that reason, it is highly desirable to develop new approaches to FT FWM spectroscopy, which release these constraints and are applicable in a wide spectral range.

This work introduces a new approach to FT FWM spectroscopy for ultrabroad spectra, which is applicable in a wide wavelength range. The concept was recently proposed by Achazi and Cannizzo (2017) and it gets along without any efforts for phase stabilization and uses only conventional linear translation stages for delay control. It is based on a multiple-camera single-shot detection scheme and implies the collection, storage and analysis of at least three optical spectra per laser shot in an experiment with ultrashort laser pulses.

There are several reasons, why collecting interferograms on a single shot base is beneficial. First of all, the phase fluctuations that are induced by vibrations of optics are related to the integration time  $t_{\text{int}}$  of the experiment and the speed  $v$  of the mechanical vibrations in the setup.

$$\Delta\varphi \leq \frac{2\pi}{\lambda} v t_{\text{int}}, \quad (2.68)$$

where  $\lambda$  is the wavelength of the detected light. In single-shot interferometry (SSI), however it is not the integration time of the detection electronics (typically on the order of microseconds for a line camera), that defines  $t$ , but the length of the laser pulses. This reduces the effective integration time down to a few femtoseconds and thus improves the phase stability by a factor of  $10^9$ . Assuming  $t_{\text{int}} = 100$  fs as an effective integration time, a typical velocity  $v = 1$  mm/s and wavelengths of  $\lambda = 400$  nm or longer, one gets  $\Delta\varphi \leq 1.6 \cdot 10^{-8}$  rad, which is less than  $\lambda/10^8$  and therefore more than suitable for an experiment with interferometric precision in the UV-VIS range of the spectrum.

A second feature of the single-shot multi-camera approach is, that it enables the user to measure any relevant differential phase shot by shot, by superimposing fractions of the respective beams with beam splitters and detecting their interferograms in spectrometers (S2 and S3, figure 2.11). From the differential phase of the beams, the pulse delay can be determined with a high precision that, among other things, depends on the spectral width of the pulses, and reaches down to a few attoseconds in the visible range, as shown in chapter 3.

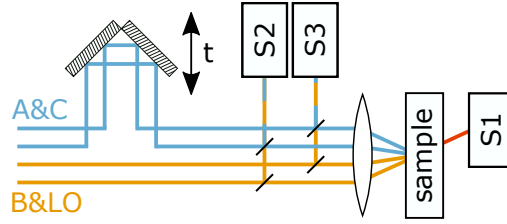


**Figure 2.11** – Conceptual sketch of the multi-camera approach. Blue beams (A and C) can be delayed by a retroreflector on a translation stage. Yellow beams: B and LO. Red: the signal is heterodyned with the LO and detected by spectrometer S1. Spectrometers S2 and S3 measure the relative phase between pulses A and B, as well as LO and C.

This allows to renounce the use of an elaborate mechanism for delay control and therefore run experiments with delays that are driven by mechanical oscillations and distributed statistically. In the analysis, it is then possible to select all these laser shots that are useful for the experiment.

It is noteworthy that, with the exact knowledge of the differential phase on a single-shot base, the delay control is executed by the statistical noise of the system, which in a conventional FT FWM spectroscopy experiment has to be suppressed as much as possible. Through the single-shot multi-camera approach both, a precise delay control and the phase stabilization become superfluous and potentially even undesired. Chapter 3 covers the potential, the abilities and the challenges of SSI in more details.



## Single-Shot Interferometry

As written in section 2.2.6, it is the motivation of this work to develop a broadband FT FWM spectroscopy experiment that avoids measures of phase stabilization or attosecond delay control by the implementation of a single-shot interferometry (SSI) scheme. While typically, great efforts are made to fulfill these two conditions for a successful time domain 2D spectroscopy experiment (see sections 2.2.5 and 2.2.4), SSI makes both endeavors superfluous or at least much easier to implement for broad band optical pulses.

### 3.1 Phase stability

In FT FWM spectroscopy, a phase stability of approximately  $\lambda/100$  is desired and systems fulfilling this requirement conventionally are considered as interferometrically stable. In case of stronger fluctuations, the contrast of the interferograms and thus the amplitude the detected signal decays. However, it is possible to achieve good results with stabilities on the order of  $\lambda/20$ .

Potential instabilities arise from air fluctuations or mechanical vibrations of optical components. This jitter accumulates throughout the integration time  $t_{\text{int}}$  of the optical detector and thus affects the measured data. The linear phase fluctuation  $\Delta\varphi$  that is induced by a single optical component  $i$ , is given by

$$\Delta\varphi_i = \frac{2\pi}{\lambda} v_i t_{\text{int}}, \quad (3.1)$$

with the speed of the oscillating part  $v_i$  and the wavelength of the detected light  $\lambda$ . These contributions, if uncorrelated, add up as a sum of squares in the case of several vibrating optical components.

$$\Delta\varphi_{\text{tot}} = \sqrt{\sum_i \Delta\varphi_i^2} \quad (3.2)$$

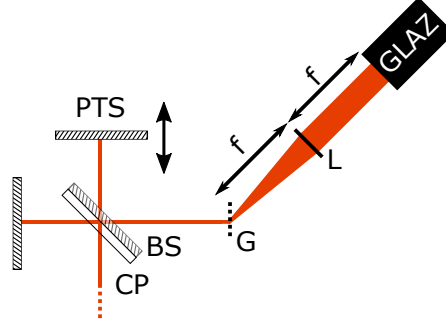


**Figure 3.1** – Schematic of Michelson interferometer and home-built spectrometer. PTS: Piezoelectric translation stage. BS: Beam splitter (50% reflectivity). CP: Chirp compensation plate. G: Diffractive grating with 600 grooves/mm. L: lens with focal length  $f = 20$  cm. GLAZ: Single-shot CMOS detector GLAZ LINESCAN with 1024 pixels of  $25\ \mu\text{m}$  width each.

Instead of reducing the speed  $v_i$  of a vibrating mechanical component or use passive phase stabilization methods, as described in section 2.2.4, decreasing the integration time leads to an identical result.

For the velocity  $v_i$  of a vibrating mirror,  $v_i \leq 1\ \text{mm/s}$  is a conservative guess, that is used in literature and approved by experimental data that were collected within this work. Assuming an integration time of the detector of  $t_{\text{int}} = 10\ \mu\text{s}$ , a number of 20 mirrors and an experiment with the lowest wavelength being  $400\text{nm}$ , this reflects in a phase jitter of  $\Delta\varphi_{\text{tot}} = 0.11 \cdot 2\pi$  rad and is thus much larger than the desired  $\lambda/100$ . However, the given integration time is well below the repetition rate of a kHz laser system. If one is able to detect, store and analyse every shot of the laser independently, the effective integration time is not anymore determined by the detection electronics but by the pulse length of the laser, which in a broad band experiment in the visible range can reach down to a few femtoseconds (see chapter 4). With  $t_{\text{int}} = 50\ \text{fs}$ , the calculation above with 20 mirrors and  $\lambda = 400\ \text{nm}$  gives

$$\Delta\varphi_{\text{tot}} \leq 10^{-9} \cdot 2\pi,$$

and therefore fulfills the limit for interferometric phase stability with ease. Even experiments with longer pulse lengths or deep ultra violet light would not fail due to a lack of phase stability, which makes this approach appealing for experiments with larger frequencies, where conventional phase stabilization is challenging.

To undermine this statement, experimental results are shown in the following. The

output of a noncollinear optical parametric amplifier (NOPA) with a spectrum of  $\lambda = 510\text{--}730\text{ nm}$  passes through a Michelson interferometer (figure 3.1), with one arm having a variable length, and is detected in a home-built spectrometer. The latter consists of a grating with 600 grooves/mm to diffract the light, which is then focused by a  $2f$ -line with a focal length of 20 cm on a single-shot CMOS detector (GLAZ LINESCAN). The detector array has a minimum integration time of  $2\text{ }\mu\text{s}$ , a maximum repetition rate of 8.5 kHz and a number of 1024 pixels of  $25\text{ }\mu\text{m}$  width each (figure 3.1). The detector calibrations of all GLAZ LINESCAN cameras in use for this work is done with two certified absorptive reference liquids, that show multiple absorption lines in the range between 240 nm and 870 nm (STARNA SCIENTIFIC HOLMIUM OXIDE and STARNA SCIENTIFIC DIDYMIUM OXIDE).

The resulting spectrum is an interferogram and it is determined by the length difference  $\Delta d$  of the two arms

$$I(\omega) = |E_A(\omega)|^2 + |E_B(\omega)|^2 + 2|E_A(\omega)||E_B(\omega)| \cos\left(\frac{\omega\Delta d}{c} + \Delta\varphi_{\text{HO}}(\omega)\right), \quad (3.3)$$

with the subscripts A and B indicating the two replicas of the pulse in the interferometer and  $\Delta\varphi_{\text{HO}}$  being the higher orders of the differential phase between the two. The path difference  $\Delta d$  between the two arms in the Michelson interferometer is set to  $\Delta d/c \approx 400\text{ fs}$ , such that the spectrometer can clearly resolve the fringes of the interferogram.

In order to impose phase fluctuations artificially, two methods were applied. Beats against the optical table of the laboratory were used to induce mechanical vibrations, whereas pressurized  $\text{CO}_2$  was used for the generation of air turbulences. Figure 3.2 (A) shows a single-shot interferogram from the experiment with the mechanical vibrations (blue), an average of 8000 shots with mechanical vibrations (red) and an average of 8000 shots with air turbulences (yellow). While the single-shot data show the largest contrast of all measurements, both, turbulences as well as mechanical vibrations of the optical components lead to a partial collapse of the fringes, namely the third term of equation 3.3.

Quantitatively, in the case of mechanical vibrations, the contrast of the fringes is reduced down to 6% with respect to the single shots in the spectral region around 650 nm. Inducing air turbulences leads to a reduction down to 65%. Both can best be seen in figure 3.2 (B), where only the oscillatory part of the interferogram, which corresponds to the third term in equation 3.3, is plotted. Isolating this contribution was done with a windowing function in the Fourier space. Similar

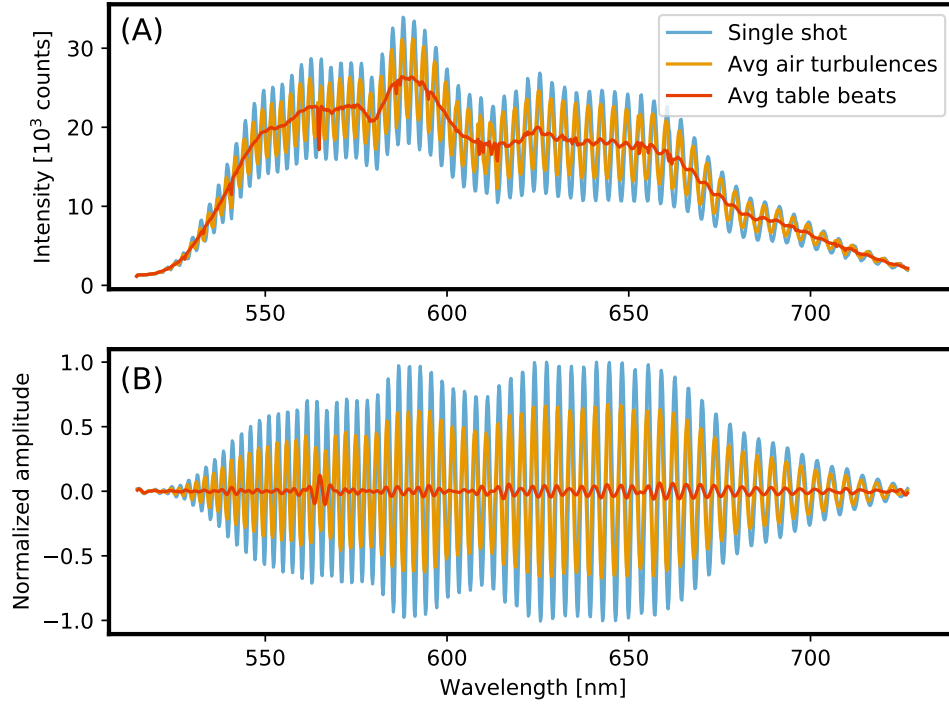


**Figure 3.2** – Comparison of a single-shot interferogram and averaged interferograms in non-phase stable conditions. 8000 interferograms were measured with two different types of perturbation. Blue: Single-shot interferogram while mechanical vibrations of optics have been induced by beating against the optical table. Yellow: Average of 8000 single-shot interferograms during air turbulences in the beam path. Red: Average of 8000 single-shot interferograms while bouncing against the optical table. (A) Measured intensity. (B) Oscillatory term of equation 3.3, isolated through windowing in Fourier space.

results were achieved by Achazi and Cannizzo (2017).

## 3.2 Pump-probe-to-box-CARS element

The central part of the experimental design for the presented approach to FT FWM spectroscopy with SSI is an element in the setup, which transforms a pump-probe scheme into a box-CARS geometry with an LO and at the same time allows to measure the differential phase between all relevant involved pulses. This component, called pump-probe-to-box-CARS (P2B) element, is schematically depicted in figure 3.3. Two beams (e.g. pump and probe), of which the red one is situated



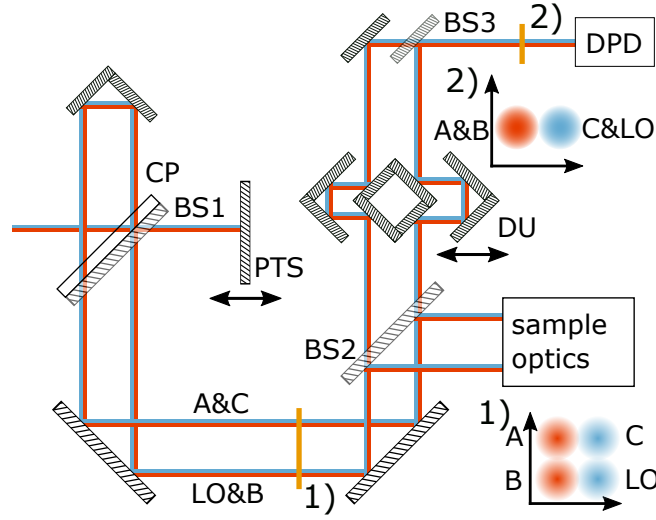


**Figure 3.3** – Schematic of the P2B element including the realization of the multi-camera approach. Two beams enter the setup from the left. Red beams are situated behind the figure plane. BS1: Beam splitter (50% reflectivity). CP: Chirp compensation plate. PTS: Piezoelectric translation stage to determine the delay of the pulses. After the modified Michelson interferometer four pulses propagate in a box-CARS geometry. BS2: beam splitter (90% reflectivity). BS3: Beam splitter (50% reflectivity). DU: Delay unit consisting of a reflecting cube and two retroreflectors, of which one sits on a translation stage. DPD: One differential phase determination setup for each pulse double-pulse beam. Inlets display the cross sections 1) and 2) marked yellow.

behind the blue one, enter parallel into a modified Michelson interferometer that consists of a 50:50 beam splitter (BS1) and a chirp compensation plate (CP). The end mirror of one interferometer arm is mounted on a piezoelectric translation stage (PTS) and the other one is a retroreflector. The beam splitter is arranged in a way that the reflective surface points towards the compensation plate. Like that, all four beams pass through the same amount of glass, which is beneficial for the pulse compression procedure. The PTS (PI HERA P-622.1CD) in the closed loop mode has a travel range of  $250\text{ }\mu\text{m}$ , a resolution of  $0.7\text{ nm}$  and a repeatability of  $\pm 1\text{ nm}$ . Its pitch and yaw angle account for  $\pm 3\text{ }\mu\text{rad}$ . After the modified Michelson interferometer four pulses propagate on parallel trajectories that correspond to the corners of a rectangle, as it is required for an experiment in the box-CARS geometry with an LO (section 2.2.3).

The majority of the intensity (90%) is then reflected towards the focusing optics and the sample by beam splitter BS2 and the signal that is emitted from the

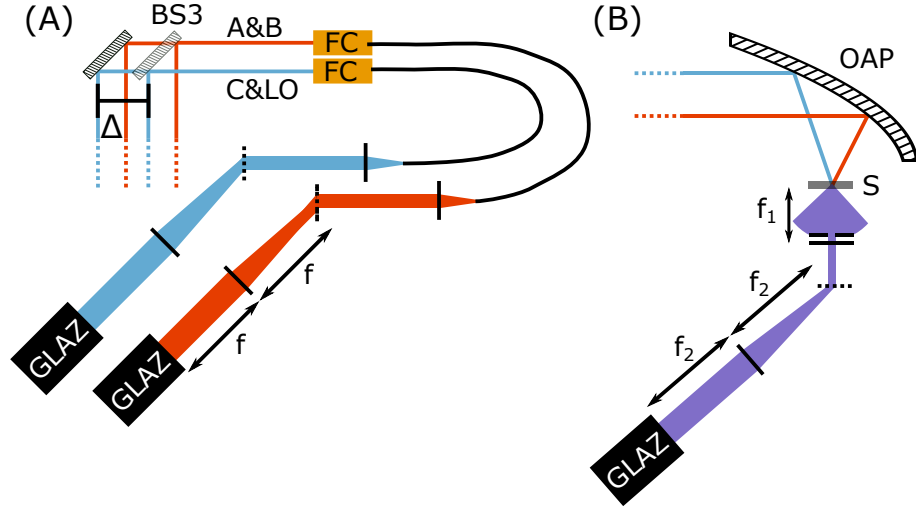


**Figure 3.4** – Schematic of the detection schemes. (A) Differential phase determination (DPD) setup. BS3: 50:50 beam splitter to overlap beams A and B, as well as LO and C. FC: fiber couplers to couple both double pulse beams into one single-mode fiber each (mode field diameter  $2.8\text{--}4.1\text{ }\mu\text{m}$ , numerical aperture  $A_N = 0.13$ ). A lens (solid black line) collimates the beam and a diffractive grating (dotted black line) is used for angular dispersion. Another lens with focal length  $f = 10$  cm creates an image point of the fiber output facet on the detector (GLAZ LINESCAN),  $\Delta$ : Additional optical path length of beams B and LO due to setup geometry and glass transmission in BS3. (B) Sample phase detection setup. OAP: off-axis parabolic mirror with effective focal length  $f_e = 10$  cm. S: Glass slab with scattering surface. Solid black lines: Lenses with focal lengths  $f_1 = f_2 = 20$  cm. Dotted black line: Grating with  $600\text{ gr/mm}$ .

sample can be detected in the detection scheme that is shown in figure 3.1. The transmitted fraction of the intensity is used to measure the differential phase of the pulse pairs (A,B) and (C,LO) in the differential phase determination (DPD) setup (figure 3.4 (A)). This is done by first overlapping the corresponding pulses spatially with a 50:50 beam splitter BS3 and afterwards coupling both double-pulse beams into one single-mode fiber each (mode field diameter  $2.8\text{--}4.1\text{ }\mu\text{m}$ , numerical aperture  $A_N = 0.13$ ) with a fiber coupler. The fiber couplers consist of an aspheric lens ( $f = 19\text{ mm}$ ) and a corresponding spacer that fixes the fiber in the correct position. The fiber is phase retaining and guides the two pulses to a spectrometer setup consisting of a collimating lens, a diffractive grating and a lens ( $f = 10\text{ cm}$ ) that focuses the light on the GLAZ LINESCAN detector (figure 3.4 (A)). This setup leads to a Gaussian waist size of the focal spot of approximately

15  $\mu\text{m}$  for a single wavelength. Since the detector has pixels with a width of 25  $\mu\text{m}$ , they are bigger than the spot size and a better wavelength resolution and thus a larger range of delays, that are detectable with the DPD, is only achievable with a different detector array.

With this scheme, a spectral resolution of 0.14 nm/pixel can be achieved. Assuming that at least four pixels per fringe are desirable to extract a phase from the interferogram, the upper limit for  $t_{\text{AB}}$  that is detectable with this scheme is about

$$t_{\text{max}} = 2.2 \text{ ps} \quad (3.4)$$

for light with a wavelength of 600 nm. On the other hand, the lower limit  $t_{\text{min}}$  is defined by the delay that leads to one single fringe over the whole spectrum. A typical spectrum in the DPD reaches from 570 nm to 700 nm which corresponds to

$$t_{\text{min}} = 10 \text{ fs.} \quad (3.5)$$

The real  $t_{\text{min}}$  has to be estimated by a factor 4 or 5 higher, since it is tough to identify a single fringe in a spectrum that has an intrinsic structure.

During an FT FWM spectroscopy experiment, the range of interest for delays will be approximately  $t_{\text{AB}} = -100 \text{ fs}$  to  $t_{\text{AB}} = +100 \text{ fs}$ . This delay, however is related to the sample position and not the DPD setup. If the PTS in figure 3.3 is set to a delay in this range, the delay of the pulses in the DPD setup will be shifted by a value  $\Delta/c$ , where  $\Delta$  is the additional optical path length of the beams LO and B between the beam splitter BS3 and the last mirror before BS3, as well as the transmission through the glass of the beam splitter (figure 3.4 (A)).  $\Delta$  is approximately 1 cm and thus  $\Delta/c \approx 30 \text{ ps}$ . This is a delay that exceeds by far the upper limit  $t_{\text{max}}$  of the DPD. For that reason, the P2B element contains a delay unit (DU, figure 3.3) that consists of a reflecting cube and two retroreflectors. One of the retroreflectors is placed on a manual translation stage to induce a variable delay to the pulses A and C. This allows to tune the delay between the pulses A and B, as well as LO and C with a precision of approximately 70 fs, which is precise enough to set the delay in the DPD to values between  $t_{\text{min}}$  and  $t_{\text{max}}$ , independent from the delays at the sample position.

The presented approach to FT FWM spectroscopy necessitates at least three spectrometers: one for the heterodyne detection of signal and LO and one for

the DPD of each pulse pair (A,B) and (C,LO). For the analysis, it is crucial, that every single-shot spectrum from a camera can be assigned to the correct spectrum from the other cameras. To guarantee that, the three cameras communicate in a master/slave configuration. That means that one camera, namely the master, collects all the data acquired from the other cameras (slaves) and sends it to the computer. Only when the master got the information from all cameras that they are ready to detect the next shot, as well as a trigger signal from the laser system, it permits the detection of the next shot to all slaves simultaneously. This scheme makes sure, that if one camera misses a shot, not all subsequent shots cannot be assigned to the right data in one of the other detectors anymore. Of course, it is possible to add one or more photodiodes or further cameras to the master/slave configuration, if needed.

### 3.3 Delay extraction algorithm

For the presented approach to FT FWM spectroscopy, it is crucial, to measure the delays of the pulses A and B as well as C and LO on a single-shot base with the highest possible precision, but at least  $\lambda/20$ , which in the range of  $\lambda = 600$  nm corresponds to 100 as. In order to fulfill this requirement, many approaches have been developed and tested throughout this work and they all have in common, that the respective pulse pair is overlapped and detected in a DPD setup (figure 3.4 (A)). The intensity that is then measured by the detector is an interferogram and is identical to the one described in equation 3.3 with  $t = \Delta d/c$  being the delay between the two considered pulses.

From this point on, a multiplicity of methods exists to get the delay of the two pulses. The complexity of the approaches varies a lot, as they range from fitting a function like the cosine in equation 3.3 to the interferograms in the frequency space, running a peak finding procedure on the Fourier transform of the interferograms in the time space, to an extraction of the phase of the complex interferogram and a subsequent determination of the phase parameters. One major outcome of this study was, that a fast Fourier transform (FFT) from the frequency to the time space and/or vice versa is disadvantageous, since that necessitates equidistant steps of the interferogram in the frequency space. After the measurement, however, equidistant spacing is only given in the pixel domain and some kind of interpolation would be necessary. Such an interpolation, on the other hand, always leads to truncation errors and thus induces noise that in consequence reduces

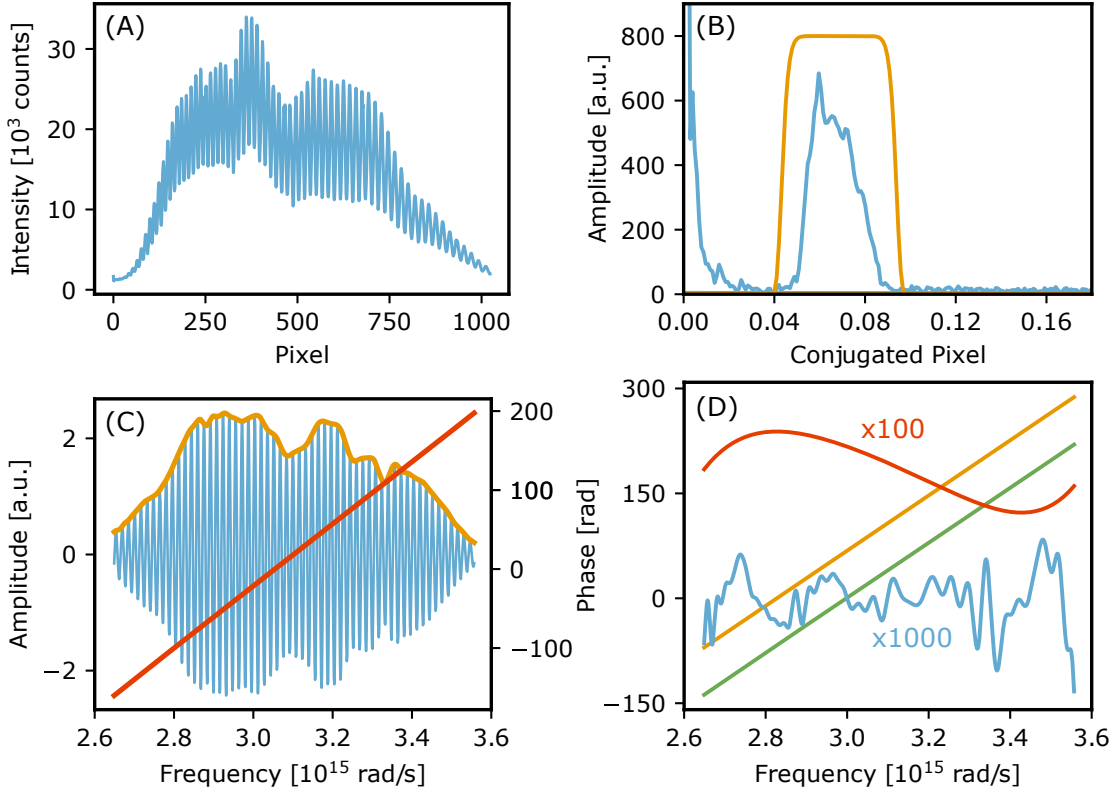


**Figure 3.5** – Delay extraction algorithm. (A) Interferogram in the pixel space. (B) Blue: Amplitude of the complex valued signal in the conjugated pixel space after FFT. Yellow: Higher-order Gaussian as windowing function. (C) Complex spectrum in the frequency space after back-transform and detector calibration. Red: Phase. Yellow: Amplitude. Blue: Real part. (D) Linearization results after averaging  $N = 4000$  interferograms. Green: Phase from subfigure (C). Yellow: Linearized phase. Red: Subtracted higher orders magnified by factor 100. Blue: Residuals of the linear fit, magnified by factor 1000.

the precision of the delay extraction algorithm.

It was thus a major finding of this work that the precision on the delay extraction can be improved by applying the FFT directly in the trivially equidistant pixel space of the detector, selecting the oscillatory term of equation 3.3 by windowing in the conjugated pixel space and transforming the data back into the pixel domain. Now, no equidistant spacing is needed anymore and one can assign a frequency to each pixel of the detector without expecting losses in precision. In the following, the analysis procedure that was tested to extract the delay between two pulses shot by shot with the best precision is presented in more detail.

Initially, there is a set of  $N$  interferograms in the pixel space (figure 3.5 (A)), which are assumed to all have identical higher phase orders ( $\Delta\varphi_{\text{HO}}$  in equation 3.3), since the material transmission does not change from one shot to the next. However, due to fluctuations of the opto-mechanic components, the delay  $t$  between two pulses A and B might vary. The number of interferograms  $N$  depends of course on the type of experiment and the acquisition time, but with a 5 kHz laser system already after a few seconds it reaches tens of thousands. For illustration, 4000 shots of the data that were already used in figure 3.2 (blue) are analyzed and figure 3.5 shows each step of the procedure for one single interferogram.

**Windowing in the conjugated pixel space** It is the first step to perform an FFT for every interferogram from the pixel space to the conjugated pixel space. Doing a detector calibration first would necessitate a subsequent interpolation, since an FFT requires equidistant spacing of the points, which a calibration does not give. An interpolation, however, leads to unwanted noise and is avoided by doing the FFT from the pixel space instead of the frequency space. The result is a complex function, whose amplitude contains a zero-frequency component, which corresponds to the first two contributions of equation 3.3 and a peak at a higher position in the conjugated pixel space that represents the oscillatory pattern of the interferogram, namely the third term of equation 3.3 (figure 3.5 (B)). The latter is the one that contains the information on the differential phase and can be isolated by a multiplication with a windowing function, e.g. a higher-order Gaussian. Besides the isolation of the oscillatory part of the interferogram, this step reduces the overall noise of the data.

**Calibration in the pixel space** The back-transform of the windowed signal in the conjugated pixel space yields  $N$  complex spectra in the pixel space and as displayed in figure 3.5 (C), through a detector calibration, one obtains spectral amplitudes  $A_i(\omega)$  and phase data  $\Delta\varphi_i$ .

$$\Delta\varphi_i(\omega) = \Delta\varphi_{\text{HO}}(\omega) + \omega t_i \quad (3.6)$$

**Linearization and first order fitting** Since the higher orders of the phase are identical for all shots, they can be subtracted from  $\Delta\varphi_i$  to get a linearized phase

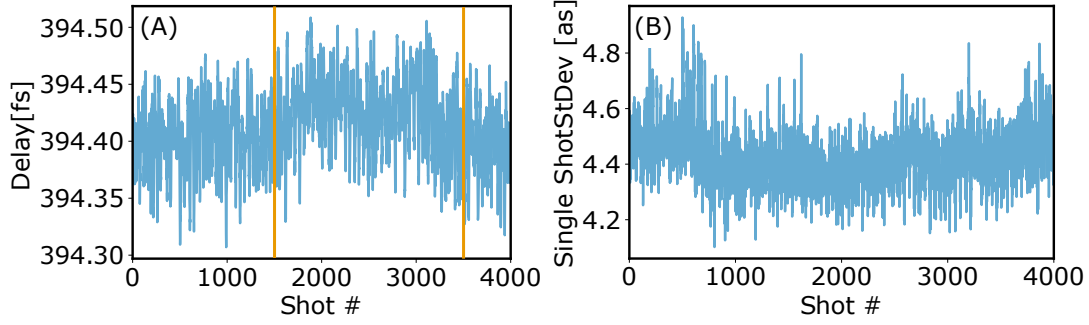


**Figure 3.6** – Results of the delay extraction algorithm explained in figure 3.5. (A) Delay for every of the 4000 shots. Average value  $t_{\text{ave}} = 394.4$  fs, the delay fluctuation is  $\Delta t = 30$  as standard deviation. Yellow markers: Range of shots with increased delay. (B) Single-shot fitting error in terms of standard deviation  $\delta t < 5$  as.

$\Delta\varphi_{i,\text{lin}}(\omega)$ . Therefore first, the average phase of all  $N$  shots is calculated.

$$\Delta\varphi_{\text{ave}}(\omega) = \Delta\varphi_{\text{HO}}(\omega) + \frac{1}{N} \sum_{i=1}^N \omega t_i = \Delta\varphi_{\text{HO}}(\omega) + \omega t_{\text{ave}} \quad (3.7)$$

After that a higher order polynomial function is fitted to the average value and all orders except the first one are subtracted from the single shot phase  $\Delta\varphi_i$ . The results are  $N$  linearized phase functions  $\Delta\varphi_{i,\text{lin}}(\omega)$  and to each of them an individual polynomial of first order can be fitted. This step is depicted in figure 3.5 (D) with the original and the linearized phase being a bit shifted for the sake of visualization. The higher orders are magnified by a factor of 100. In this case, they, since the experimental setup barely leads to any additional material transmission for one of the two pulses. However, if one of the pulses experiences more glass transmission,  $\Delta\varphi_{\text{HO}}$  can become more significant.

The advantage of this approach compared to a fitting of  $N$  high-order polynomials to the complete phase functions  $\Delta\varphi_i$  is twofold. First, the computational time is reduced a lot, because a fitting procedure with more than two parameters only has to be executed for the average phase and not for every single shot. Second, this method profits from the knowledge that all higher order terms  $\Delta\varphi_{\text{HO}}(\omega)$  are identical and reduces the number of fitting parameters to two, namely the zeroth and first order. A high number of fitting parameters, though, can lead to a worse precision of the fit, since small variations in one parameter can be compensated by

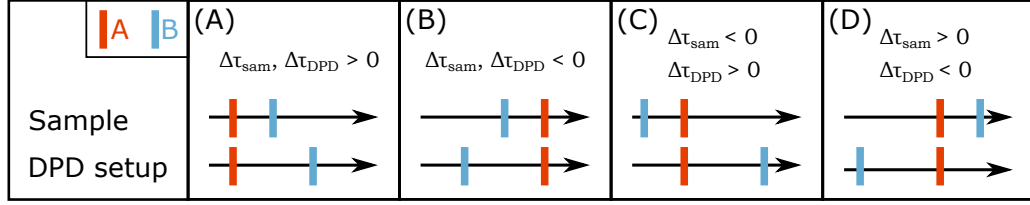


**Figure 3.7** – Possible temporal arrangements of pulses in DPD setup and sample position that are indistinguishable by measuring only the absolute value. Red: Pulse A. Blue: Pulse B. A delay is considered positive, if A appears earlier than B. Without loss of generality, pulses A are drawn to appear at identical times.

another one. This effect is called parameter correlation (Johnson, 2000). In the data that are shown in figure 3.5, the presented approach increases the precision by a factor of 6 compared to a single-shot high-order polynomial fitting. However, the more higher order contributions a phase has, the more one benefits from this linearization method.

The physical interpretation of the different polynomial orders of the spectral phase is in more detail discussed in chapter 4, but the first order of the spectral differential phase is the one that is the most relevant for this chapter, since it is a direct measure of the delay between two pulses.

Figure 3.6 (A) shows the delays that were extracted by the algorithm described above and in figure 3.5 for every of the 4000 shots. In average, the delay is  $t_{\text{ave}} = 394.4\text{fs}$  and the  $t_i$  are distributed around the average with a standard deviation of around  $\Delta t = 30\text{as}$ . The increased delay between shot number 1500 and and shot number 3500 (between yellow markers) most probably results from the air turbulences that were induced with pressurized  $\text{CO}_2$  during the experiment. Note that this dataset was taken from the measurement presented in figure 3.2.

Figure 3.6 (B) shows the single-shot standard deviation fitting error on the first order parameter, which is the precision of the delay extraction algorithm. For the presented dataset, this value is as low as  $\delta t < 5\text{as}$ .

### 3.4 Phase calibration procedure

For geometrical reasons, that were explained in section 3.2 the differential phase that is measured in the DPD setup is not identical to the phase, the two pulses have at the sample position. For that reason, a calibration, that allows to retrieve



the phase at the sample position from the phase that was extracted from the DPD setup, has to be done. The two beams, whose differential phase should be calibrated, are sent to the sample position and the DPD setup simultaneously. As can be seen in figure 3.4 (B), an off-axis parabolic mirror with an effective focal length of  $f_e = 10$  cm focuses both beams into one spot. A glass slab with a scattering surface is moved into this point and scatters both beams at angles that partly overlap. A diaphragm and a lens with  $f_1 = 20$  cm select and collimate the desired part of the scattered light. The spectrometer in this detection scheme is identical to figure 3.1 and consists of a grating with 600 grooves/mm as a dispersive element, a lens with  $f = 20$  cm and the GLAZ LINESCAN detector that was already described beforehand (figure 3.4 (B)).

Since the previously non-collinear beams are now superimposed by the scattering surface, the detected intensity follows the interferogram in equation 3.3 and one is able to retrieve the phase in the DPD setup  $\Delta\varphi_{\text{DPD}}(\omega)$  and the sample position  $\Delta\varphi_{\text{sam}}(\omega)$  simultaneously. The calibration phase, that later is needed to retrieve the sample phase from the DPD phase, is then given by

$$\varphi_{\text{cal}}(\omega) = \Delta\varphi_{\text{DPD}}(\omega) - \Delta\varphi_{\text{sam}}(\omega) \quad (3.8)$$

The result of the delay extraction algorithm is, however, not distinct, since this procedure cannot distinguish between a scenario, where beam A arrives before beam B or vice versa. Without a restriction of generality, the first case is considered a positive delay and the latter a negative one. Mathematically, this reflects in the fact, that one can only retrieve the absolute values  $|\Delta\varphi_{\text{DPD}}(\omega)|$  and  $|\Delta\varphi_{\text{sam}}(\omega)|$ . Since in both measurement arms, the delay can be either positive or negative, there are four combination, how the pulses can be arranged in time for a given set of  $|\Delta\varphi_{\text{DPD}}(\omega)|$  and  $|\Delta\varphi_{\text{sam}}(\omega)|$ . This is explained in figure 3.7.

**Table 3.1** – Links between increasing or decreasing absolute values of delays with scenarios in figure 3.7 for a motion of beam B towards later points in time.

$ \Delta\tau_{\text{sam}} $	$ \Delta\tau_{\text{DPD}} $	Scenario
$\nearrow$	$\nearrow$	A
$\searrow$	$\searrow$	B
$\searrow$	$\nearrow$	C
$\nearrow$	$\searrow$	D

Breaking this symmetry, to overcome the ambiguity of the differential phase, can be done by moving the PTS and collecting interferograms in different stage positions. In doing so, e.g. pulse B can be moved towards later times, whereas pulse A remains unchanged. This corresponds to an increase of the delay  $\Delta\tau$  in both, the DPD setup and the sample position. Table 3.1 shows how to link the results of a symmetry break with increasing  $\Delta\tau$  with a scenario in figure 3.7.

If this scenario yields, that  $\Delta\tau_{\text{sam}}(\omega)$  or  $\Delta\tau_{\text{DPD}}(\omega)$  is negative, the sign of  $\Delta\varphi_{\text{sam}}(\omega)$  or  $\Delta\varphi_{\text{DPD}}(\omega)$ , respectively, has to be inverted before the subtraction in equation 3.8. After  $\varphi_{\text{cal}}(\omega)$  is known, one can, on a shot-by-shot base, conclude from  $\Delta\varphi_{\text{DPD}}(\omega)$  to  $\Delta\varphi_{\text{sam}}(\omega)$ .

### 3.5 Simplification of translation stage alignment

Measuring the delay between the two excitation pulses on a single-shot base instead of defining it with a delay control mechanism (section 2.2.5) simplifies FT FWM tremendously. One aspect of this simplification is the adjustment of the PTS. If the translation direction of the stage is not perfectly parallel to the incoming beam, a wrong delay between the two excitation pulses is assumed, as depicted in figure 3.8. The hatched rectangles are the variable end mirror of one Michelson interferometer arm in different scenarios. Black is the initial position before a motion. In the red scenario, the direction of motion of the stage is parallel to the beam (yellow), whereas the blue mirror moved with a slight tilting angle  $\alpha$ , but by the same distance. While the delay of the laser pulse in the red case, will be identical to the shift of the stage, a mismatch of  $\Delta x$  has to be considered in the blue case. Obviously, this mismatch scales with the length of the mirror motion  $x$  and can be calculated as

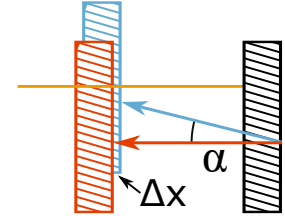


**Figure 3.8** – Effect of a tilted translation stage in a Michelson interferometer arm. Yellow: incoming and outgoing beam. Black: Mirror in initial position. Red: Mirror after a motion parallel to the beam. Blue: Mirror after a motion with a tilt of angle  $\alpha$ .  $\Delta x$ : Resulting mismatch.

$$\frac{\Delta x}{x} = 1 - \cos \alpha. \quad (3.9)$$

By measuring the delay between the pulses instead of relying on the PTS and its alignment, the presented approach to FT FWM spectroscopy overcomes problems

of this kind. A potential scaling factor in the delays can now be recognized during the analysis but does not lead to wrong results.

## 3.6 Conclusion

As a conclusion of the SSI chapter, it can be said, that throughout this work, evidence was produced, that a single-shot detection scheme in combination with a femtosecond laser system reduces the phase fluctuations in a FT FWM setup such that no further efforts for phase stabilization are needed (section 3.1) and it even resists heavy perturbation like e.g. beats against the optical table.

Furthermore, the P2B element was designed and implemented (section 3.2). It converts a pump-probe setup into a box-CARS geometry with an LO for FWM experiments, adds a variable delay to the duplicates of the incoming pulses and at the same time, with its multi-camera approach, allows to measure all relevant delays on a shot-by-shot base. For this precise measurement, many single-shot phase extraction algorithms have been developed and tested. The one with the best results yields a single-shot precision of few attoseconds (figure 3.6) and is presented in section 3.3. In order to conclude on the differential phase of two pulses at the sample position, a phase calibration procedure was established (section 3.4).

It is noteworthy that the fundamental idea of SSI together with the multi-camera approach is expandable to basically any wavelength range. One of the requirements is the availability of beam splitters for the Michelson interferometer, even though, this could also be realized with a knife edge mirror. Furthermore the existence of single-shot line cameras is crucial.



# Chapter 4

---

## Shaping and Characterization of Ultrabroad Pulses

A full mathematical description of a plane wave is given by the electric field in the time domain

$$\vec{E}(\vec{r}, t) = \vec{E}'(\vec{r}, t) e^{i(\vec{k} \cdot \vec{r} - \omega t + \varphi(t))} \quad (4.1)$$

where  $\vec{E}'$  is the polarization vector. An equivalent definition can be done in the frequency domain

$$E(\omega) = A(\omega) e^{i\varphi(\omega)} \quad (4.2)$$

with the spectral amplitude  $A(\omega)$  and the corresponding phase  $\varphi(\omega)$ . Pulsed lasers, as they are used in this work, emit wave packets showing a behavior that often is approximated with a Gaussian curve in time and frequency.

$$E(t) = E'_0 e^{-\frac{t^2}{2\sigma_t^2}} e^{-i\omega t + \varphi(t)} \quad (4.3)$$

$$E(\omega) = A_0 e^{-\frac{(\omega - \omega_0)^2}{2\sigma_\omega^2}} e^{i\varphi(\omega)} \quad (4.4)$$

Since both approaches are connected via the Fourier transform, one can manipulate the spectral phase in order to control the temporal evolution of the pulses. To recognize the effects of the spectral phase on  $E(t)$ , it can be useful to describe  $\varphi(\omega)$  in a Taylor expansion around a central frequency  $\omega_0$ .

$$\begin{aligned}\varphi(\omega) = & \varphi(\omega_0) + \left. \frac{d\varphi}{d\omega} \right|_{\omega_0} (\omega - \omega_0) + \left. \frac{1}{2} \frac{d^2\varphi}{d\omega^2} \right|_{\omega_0} (\omega - \omega_0)^2 \\ & + \left. \frac{1}{6} \frac{d^3\varphi}{d\omega^3} \right|_{\omega_0} (\omega - \omega_0)^3 + \dots + \left. \frac{1}{n!} \frac{d^n\varphi}{d\omega^n} \right|_{\omega_0} (\omega - \omega_0)^n\end{aligned}\quad (4.5)$$

The terms of this expansion are abbreviated as

$$\begin{aligned}\varphi(\omega) = & \text{CEP} + \text{GD}(\omega - \omega_0) + \frac{1}{2} \text{GDD}(\omega - \omega_0)^2 \\ & + \frac{1}{6} \text{TOD}(\omega - \omega_0)^3 + \dots\end{aligned}\quad (4.6)$$

The zeroth order of the phase is called carrier envelope phase (CEP) and is the phase difference between the carrier wave and the envelope  $E'(t)$  of the light pulse. The group delay (GD) describes the delay between the arrival of a pulse and an arbitrary point in time. A light pulse is called compressed or Fourier-limited, if the GD is constant for all frequencies. In that case, a pulse cannot become any shorter in time without changing the absolute value of the spectrum. The group delay dispersion (GDD) is also called the chirp of a pulse and describes the frequency dependency of the GD. In general, the  $n$ -th polynomial order of the spectral phase contributes to the GD with order  $n - 1$ . In this work, the third and fourth order dispersion are abbreviated as TOD and FOD, respectively.

While the GD corresponds to a temporal shift of the pulse envelope, the instantaneous frequency can be described as

$$\omega(t) = \frac{\partial \varphi(t)}{\partial t}.\quad (4.7)$$

This direct impact of the spectral phase on the temporal evolution of a pulse is why it is crucial to anyone active in ultrafast optical spectroscopy, but also many other fields like microscopy (Dudovich et al., 2002), interferometry (Huang et al., 2001), or telecommunication (Sardesai et al., 1998), to have means of controlling and detecting the phase of a laser.

**Table 4.1** – Examples of GDD of different materials at wavelength  $\lambda = 600$  nm.

Material	Thickness	GDD	Reference
F2 glass	1 mm	163 fs <sup>2</sup>	(Schott, 2017)
Fused quartz	1 mm	56 fs <sup>2</sup>	(Malitson, 1965)
CaF <sub>2</sub>	1 mm	40 fs <sup>2</sup>	(Malitson, 1963)
Air	1 m	28 fs <sup>2</sup>	(Ciddor, 1996)

## 4.1 Pulse shaping techniques

There are numerous techniques and processes that can manipulate the phase and/or the amplitude of a laser pulse. In the following, some will be presented.

### 4.1.1 Material transmission

Due to frequency dispersion of the refractive index  $n(\omega)$ , the transmission through an optical medium with thickness  $d$  alters the spectral phase according to

$$\varphi(\omega) = \frac{2\pi n(\omega)d}{\lambda} = \frac{n(\omega)d\omega}{c}. \quad (4.8)$$

Consequently, any material with a non-constant refractive index induces higher orders of phase to the pulse and changes its temporal structure. Typically, transparent materials show  $\partial n/\partial\omega > 0$ , which is a so called positive chirp. This implies  $\partial\varphi/\partial\omega > 0$  and lower instantaneous frequencies at the leading edge of the pulse. The GDD values of some materials that are often used in spectroscopic experiments are given in table 4.1 for  $\lambda = 600$  nm.

Figure 4.1 shows a simulated spectrum in the visible range (A), as well as two equivalents of this spectrum in the time domain. The difference between the two is only in the spectral phase. The transient in figure (B) is in the Fourier limit, whereas figure (C) and the yellow spectral phase in (A) were calculated for a transmission through 0.2 mm of fused silica.

Since material transmission adds GDD and higher orders of phase, they have to be compensated for, if a Fourier-limited pulse is desired. To do so, several techniques have been established and in a way, all of them isolate the different spectral components and manipulate the respective phase. Proceedings to separate different frequencies can be of refractive or diffractive nature, as it is done in  $4f$ -setups

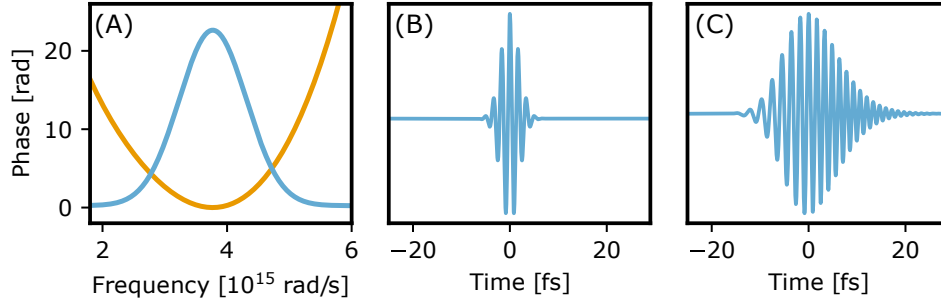


**Figure 4.1** – Effect of transmission through fused silica on a compressed laser pulse. (A) Blue: considered spectrum of the electric field. Yellow: Phase after transmission through 0.2 mm of fused silica. To stress the higher orders, CEP and GD are subtracted from the phase. (B) Transient of the Fourier-limited pulse with the spectrum displayed in (A). (C) Transient of a pulse with spectrum and phase from (A).

with prisms or gratings that might be upgraded with a phase mask to allow for arbitrary pulse shaping. Others, like chirped mirrors introduce phase differences by artificial resonances. Some of these methods are presented in the following.

#### 4.1.2 Grating compressor

A grating compressor is a symmetric arrangement of four diffractive gratings, where the first and the second, as well as the third and the fourth grating are parallel (Fisher and Kelley, 1969). Gratings 3 and 4 are a mirror image of the first two and thus, the whole design can be simplified with a folding mirror in the symmetry plane (figure 4.2 (A)). The first grating angularly disperses the pulse and thus gives rise to an increasing path length with decreasing frequency. This corresponds to a negative chirp or GDD, which quantitatively can be derived by calculating the optical path length with respect to the wavelength. With the grating law

$$\beta = \arcsin \left( M \frac{\lambda}{G} - \sin \alpha \right), \quad (4.9)$$

where  $\alpha$  and  $\beta$  are the entrance and diffraction angle,  $M$  is the order of diffraction and  $G$  is the grating constant, one can get the total phase  $\varphi(\lambda)$  and its second and third derivatives, as it is in more detail described in the work of Feurer and



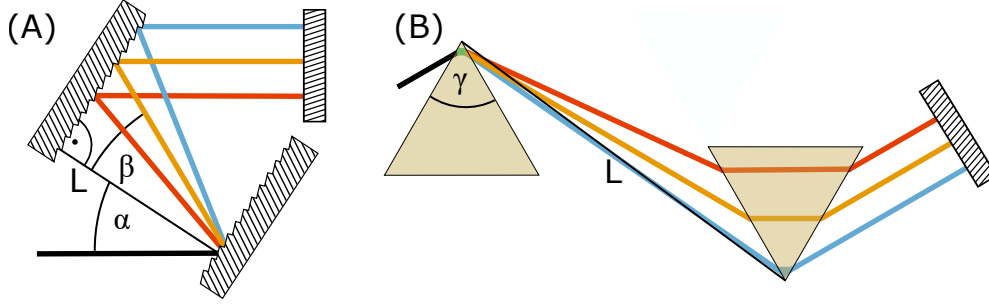


**Figure 4.2** – Schematics of folded compressors. Red, yellow and blue colors indicate beams with a low, intermediate and high frequency. (A) Folded grating compressor.  $\alpha$ : entrance angle between the incoming beam and the normal of the grating.  $\beta$ : Diffraction angle.  $L$ : Distance between the two gratings. (B) Folded prism compressor.  $\gamma$ : Apex angle.  $L$ : Length between the apex tips.

Roberts (2009)

$$\text{GDD} = \frac{d^2\varphi(\omega)}{d\omega^2} = -\frac{\lambda_0^3 L}{\pi c^2 G^2 \cos^3 \beta_0} \quad (4.10)$$

$$\text{TOD} = \frac{d^3\varphi(\omega)}{d\omega^3} = \frac{3\lambda_0^4 L}{2\pi^2 c^3 G^2 \cos^3 \beta_0} \left[ 1 + \frac{\lambda_0 \sin \beta_0}{G \cos^2 \beta_0} \right]. \quad (4.11)$$

The GDD of a grating compressor is always negative and changes linearly with the distance  $L$  between the gratings. The TOD, on the other hand, is always positive and linear with  $L$ , as well.

The disadvantage of this method is the limited transmission efficiency of gratings, when it comes to broad spectra, or even worse, an overlap of different orders of the diffracted beam, if the spectrum is broader than one octave.

### 4.1.3 Prism compressor

Using prisms instead of gratings can also lead to a tunable negative overall chirp. As in the grating compressor the arrangement is symmetric, but can be folded in the symmetry plane with a mirror. In the folded case, it consists of a dispersing and a collimating prism and the beam passes both twice. The input face of the second prism is parallel to the output face of the first one (figure 4.2 (B)).

Quantitatively, in such a setup the optical path length for every wavelength can be derived by applying Snell's law and making some geometric assumptions. First,

the angle  $\alpha_1$  of the incoming beam and the first surface is the Brewster angle of the center frequency  $\omega_0$ . This yields – if a  $p$ -polarization is chosen – a maximum efficiency of the compressor. Second, the apex angle  $\gamma$  has to be such that the angular deviation of the beam is minimum, which leads to a symmetric passage of the beam through the prisms and ensures that the Brewster angle is also obtained at the output face. The derivatives of the spectral phase are then (Feurer and Roberts, 2009)

$$\text{GDD}(\lambda) = -\frac{4\lambda_0^3 L}{\pi c^2} \left( \frac{dn}{d\lambda} \Big|_{\lambda_0} \right)^2 \quad (4.12)$$

$$\begin{aligned} \text{TOD}(\lambda) = & -\frac{6\lambda_0^4 L}{\pi^2 c^3} \left[ \left( \frac{dn}{d\lambda} \Big|_{\lambda_0} \right)^2 \left( 1 - \lambda_0 \frac{dn}{d\lambda} \Big|_{\lambda_0} \left( \frac{1}{n^3} - n^2 \right) \right) \right. \\ & \left. + \lambda_0 \frac{dn}{d\lambda} \Big|_{\lambda_0} \frac{d^2 n}{d\lambda^2} \Big|_{\lambda_0} \right]. \end{aligned} \quad (4.13)$$

Note that equations 4.12 and 4.13 both do not contain phase contributions that arise from the material transmission of the beam, since these depend on how far the prisms are inserted into the beam. The minimal insertion length, in case of the first prism, is related to the diameter of the beam. For the second prism, the bandwidth of the light and the length  $L$  between the apex tips determine the minimal amount of added material. Both, GDD and TOD are negative proportional to the length  $L$ , which is the regulator of the desired induced phase.

To show the capabilities of a prism compressor, a numerical calculation using ray tracing methods (ZEMAX) has been performed for the following parameters. Prism material: SF11,  $\gamma = 60^\circ$ ,  $L = 5$  cm, beam diameter 3 mm, and a spectrum from 500 to 600 nm. The insertion lengths of the prisms were chosen to minimize the path length of the pulses inside the prisms but still allow a transmission with the full diameter of the beam. The resulting phase parameters are  $\text{GDD} = -1930 \text{ fs}^2$ ,  $\text{TOD} = -17600 \text{ fs}^3$ . This GDD value corresponds to a transmission through approximately 30 mm of fused silica glass in the considered spectral range.

Already for a spectrum of  $\lambda = 450\text{--}650$  nm, however, the second prism needs to have a face of 38 mm width because of the strong angular dispersion of the first prism, if a similar GDD should be achieved. This in return increases the material transmission and thus leads to considerably higher order contributions

to the spectral phase. Obviously this compression approach is inappropriate for spectra broader than the previously discussed ones.

#### 4.1.4 Chirped mirror

A dielectric or Bragg mirror is composed of thin layers with alternating refractive indices  $n_i$  and well defined layer thicknesses  $d_i$ . Every layer transition leads to a reflection behavior based on the Fresnel laws. Beams reflected from different transitions propagate in the same direction and may interfere destructively or constructively, depending on the optical path length difference  $\delta_i = 2n_i d_i$  and the considered wavelength  $\lambda$ .

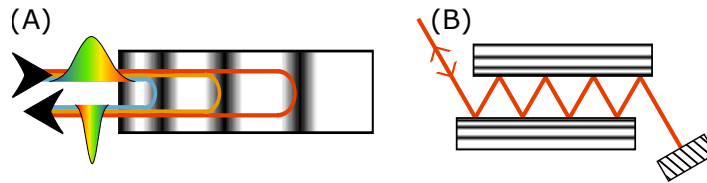


**Figure 4.3** – (A) Schematic of a chirped mirror. A positively chirped pulse enters a dielectric mirror with chirped layer structure, where the reflections of lower frequencies occur in deeper layers in the mirror. (B) Folded chirped mirror setup to realize a large amount of reflections,

A tailored wavelength dependency of the optical path length can thus be reached by not using a strict periodicity of refractive indices, but a specifically matched design such that reflection occurs in different layers for different wavelengths instead (Szipöcs et al., 1994), as it is sketched in figure 4.3 (A). Chirped mirrors typically reach a GDD of tens to few hundreds of  $\text{fs}^2$  per reflection, depending on the spectrum they cover and can of course also be designed to compress for higher order phase distortions. Since this value is rather small, people typically use setups in which several reflections on the chirped mirror are performed. Figure 4.3 (B) sketches a design that consists of two chirped mirrors and a folding mirror (hatched) that makes the beam pass the setup twice.

Fresnel reflections on the very first surface, however, yield disturbing dispersion ripples in the spectral phase. They are an inevitable result of summing the pulses reflected from the interface between the ambient medium and the mirror and shaped pulses that are reflected inside the mirror (Steinmeyer, 2003; Matuschek et al., 1999).

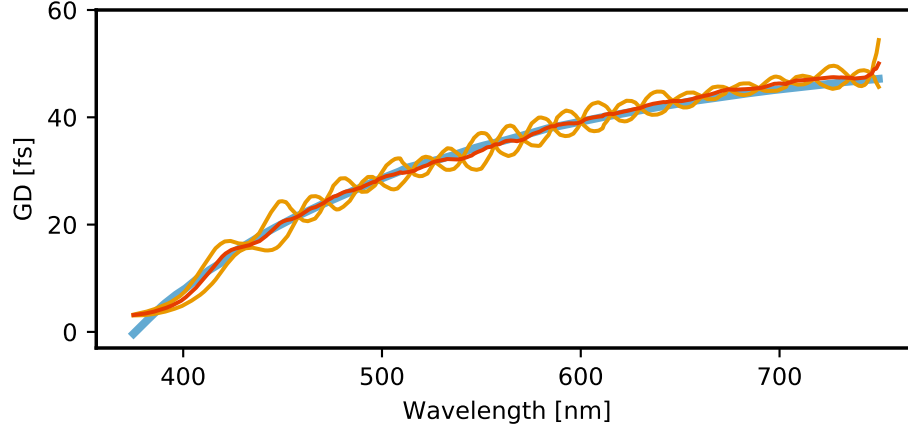


**Figure 4.4** – GD of chirped mirror pair by LAYERTEC, that was used during this work. Incident angle:  $0^\circ$  to  $10^\circ$ . Yellow: two different surfaces. Red: average. Blue: GD of 0.26 mm of fused silica glass.

Different procedures have been established to minimize dispersion ripples. One possibility targets at a reduction of unwanted reflections at the first surface and is called double chirped mirror (DCM). It consists of the implementation of an anti-reflective coating (ARC) on the surface of the mirror followed by a section in which the impedance of the mirror is matched to the ARC. This section excels by a slowly increasing duty-cycle of the refractive index variations and thus a continuous rise of the averaged refractive index. Subsequently to this index matching part a normal single chirped segment might be added, where only the Bragg frequency and not the duty cycle is modulated (Matuschek et al., 1999). Effective dispersion ripple suppression requires a reflectivity on the air-mirror interface with  $R < 10^{-4}$ . This is not possible for normal incidence beams and spectra with  $\lambda_U/\lambda_L > 1.5$ , where  $\lambda_U$  and  $\lambda_L$  indicate the upper and lower limit of the spectrum, respectively (Dobrowolski et al., 1996).

Another approach is the application of a chirped mirror pair (CMP), where both surfaces have slightly frequency-shifted dispersion ripples. While the total reflectivity will then be the product of every single reflectivity, the total GD can be derived by the sum of every reflection's GD (Laude and Tournois, 1999). If the light undergoes the same amount of reflections on either mirror, the resulting GD will be much smoother than for single mirrors, as it can be seen in figure 4.4.

Brewster-angled chirped mirrors feature a design in which a  $p$ -polarized beam

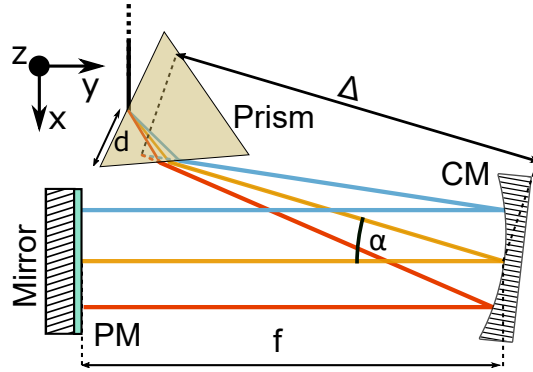


**Figure 4.5** – Schematic of a folded adaptive pulse shaping setup. The light enters from the top, is dispersed by a prism and after a distance  $\Delta$  collimated by a cylindrical mirror (CM). The distance between the phase mask (PM) and the cylindrical mirror fits the focal length  $f$  of the latter. A folding mirror is placed immediately after the phase mask. In the case of  $\Delta = f$ , the presented scheme is a  $4f$ -setup.  $d$ : Insertion length of the prism.

enters the layer structure in the Brewster angle. Hence, surface reflections and consequently also dispersion ripples are eliminated. Brewster-angled chirped mirrors have been designed for broad wavelength ranges of  $\lambda = 500\text{--}750\text{ nm}$ . In doing so, an ARC is not needed and the DCM section can be designed much simpler (Baum et al., 2006). Brewster angles for the visible region are typically in the range of  $55^\circ$  and thus rather large. Since usually tens of reflections on a mirror are necessary, the geometric design of such a setup can become challenging.

For parts of the presented work, a CMP was implemented. It was produced by LAYERTEC and its performance can be seen in figure 4.4, which shows the GD of 0.26 mm of fused silica glass (blue), as well as the two reflective surfaces of the CMP (yellow). Red is the average of the two yellow lines and corresponds thus to an average reflection on the CMP. Both reflecting surfaces are  $40\text{ mm} \times 10\text{ mm}$  large, such that it is possible to have several reflections on each surface. To achieve a smooth spectral GD, it is of course necessary to have an identical number of reflections on either surface. An implementation as in figure 4.3 (B) is a suitable solution, that was used during this work. The reflectivity is  $> 99.8\%$  in the range from 375 nm to 750 nm and the mirrors are designed to be used with an incident angle between  $0^\circ$  and  $10^\circ$ .

### 4.1.5 Adaptive pulse shaping

All the pulse shaping methods mentioned beforehand have in common to be more or less static techniques with a limited number of adjustable parameters. In grating and prism compressors, the distance between the disperser and the collimating element can be varied, whereas in the case of chirped mirrors, one might change the number of reflections. In any case, altering the induced phase includes changing the optical beam path.

In contrast to that, adaptive pulse shaping includes a fixed  $4f$ -line with a variable phase mask in the Fourier plane. The  $4f$ -line can be folded in the Fourier plane, such that it consists of a spectral angular disperser, like a prism or a grating and a collimating element, e.g. a lens or a concave mirror (figure 4.5). Since within this work pulse shaping is used for compression, lenses, which add a positive chirp, are not an adequate means for collimation.

Using a prism instead of a grating as a dispersive element was, to the best of my knowledge, never implemented before and – if designed and arranged in Brewster angle conditions – enables a strongly increased throughput compared with gratings. In section 4.3, ray tracing simulation results of both options are compared.

The modification of the phase in the Fourier plane is in any case achieved by varying the optical path length  $\delta(\lambda) = n(\lambda) d(\lambda)$  for each spectral component. Some techniques, like deformable mirrors, vary the actual distance  $d(\lambda)$ , whereas others, like LC SLMs, apply different refractive indices  $n(\lambda)$  for different wavelengths.

#### Deformable Mirror

One group of devices that can serve as a phase mask are deformable mirrors. They consist of an array of actuators which is covered by a reflective surface. This surface can either be a reflective coating of each pixel (pixelated deformable mirror, (Hacker et al., 2003)) or a reflective membrane (membrane deformable mirror, (Zeek et al., 1999)). The actuators are controlled individually and might be either of piezoelectric nature or simple electrodes that apply an electrostatic force. Independent of the actuator type and whether a membrane or pixelated device is considered, the optical path length is altered via the actual distance  $d(\lambda)$ , light with a certain wavelength travels, whereas the refractive index  $n(\lambda)$  remains constant.

Membrane devices can apply smoother optical path length modulations than pix-

elated shapers and thus avoid pulse replicas (section 4.2). However, there is a maximum displacement difference between two adjacent frequency components due to limited membrane elasticity. Consequently, phase wraps are not possible and the maximum stroke distance of the actuators limits the shaping capability.

Pixelated devices, on the other hand, allow phase wraps with modulo  $2\pi$  rad and one can induce spectral phase functions that otherwise would excel the maximum deflection of the actuators. Furthermore, amplitude shaping was proven to be possible with pixelated deformable mirrors by implementing not only a piston, but also a tilt motion control to every pixel (Extermann et al., 2011).

A big advantage of this technique is, that the only restrictions to their bandwidth are the reflectivity of the deformable mirror and the efficiency of the dispersive element, e.g. the prism.

### Liquid Crystal Spatial Light Modulator

An LC SLM is, as the deformable mirror presented above, a programmable phase mask that can induce a predetermined spectral phase to a pulse, if it is placed in the Fourier plane of a  $4f$ -line like in figure 4.5. Unlike the deformable mirror, however, the optical path length  $\delta(\lambda)$  is not modified via the actual distance  $d(\lambda)$ , but by the refractive index  $n(\lambda)$  of each pixel. For this, each pixel of an LC SLM has a transmissive front face, coated with an electrically conducting material like indium tin oxide, a reflective backside with a metal coating and liquid crystals with a large anisotropy in between. Both the front and back face are electrically contacted to be able to apply a voltage. As long as no voltage is applied, brushed electrodes lead to an alignment of the rod-like liquid crystals in the  $x$ -direction (dimensions labeled in figure 4.5). As soon as the voltage is switched on, the molecules orient along the electric field vectors, which corresponds to the  $y$ -axis. Light with a polarization along  $x$  was accordingly first exposed to the extraordinary and now to the ordinary axis. Consequently, the effective refractive index changes with respect to the average rotation angle of the liquid crystals and thus the electric field that was applied. To avoid electromigration of the liquid crystals, the electric field is alternating. (Weiner, 2000)

**Diffraction-based shaping** One approach of shaping light with an LC SLM is called diffraction-based shaping (Vaughan et al., 2005). Here, a phase is applied that, in the  $z$ -direction follows a saw tooth pattern similar to a reflective blazed grating (figure 4.6). The light is then diffracted up- or downwards with respect

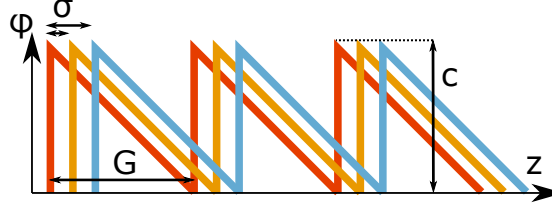


**Figure 4.6** – Illustration of diffractive shaping in the  $z$ -direction.  $G$ : grating constant,  $c$ : contrast,  $\sigma$ : spatial shift. Colors: different shifts of the saw tooth pattern.

to its expected reflected direction. This diffraction angle can be influenced by the grating constant  $G$ . By shifting one saw tooth pattern along  $z$  with respect to its neighbor pattern, a differential phase between two pixels and hence two frequency components is applied. The phase shift  $\varphi$  follows the equation

$$\varphi(\omega) = \frac{2\pi\sigma(\omega)}{G}, \quad (4.14)$$

with the shifting distance  $\sigma$ . Furthermore, diffraction based shaping not only allows to manipulate the phase of a spectral component by varying  $\sigma(\omega)$ , but also its amplitude via the contrast  $c(\omega)$ . The diffracted field can be described as a sinc function with its maximum for  $c(\omega) = 2\pi$  and  $E(c = 0) = 0$  (Vaughan et al., 2005).

$$E_{\text{out}}(\omega) = M_{\text{eff}}(\omega)E_{\text{in}}(\omega) \quad (4.15)$$

$$M_{\text{eff}}(\omega) = \text{sinc}\left(1 - \frac{c(\omega)}{2\pi}\right) e^{-i\varphi(\omega)} \quad (4.16)$$

The concept of the effective frequency filter  $M_{\text{eff}}(\omega)$  is in more detail described in section 4.2.

Figure 4.7 shows three color plots of phases imprinted on the LC SLM for no modulation (A), amplitude modulation only (B) and phase modulation only (C). While in the second and third case, the contrast of the sawtooth patterns or their vertical position is changed throughout the spectrum, neither of both is done in image (A). Of course, also a combination of amplitude and phase shaping is feasible.

A requirement of this approach is, that the spectrally dispersed light is collimated with a cylindrical mirror instead of a spherical one. Using a spherical



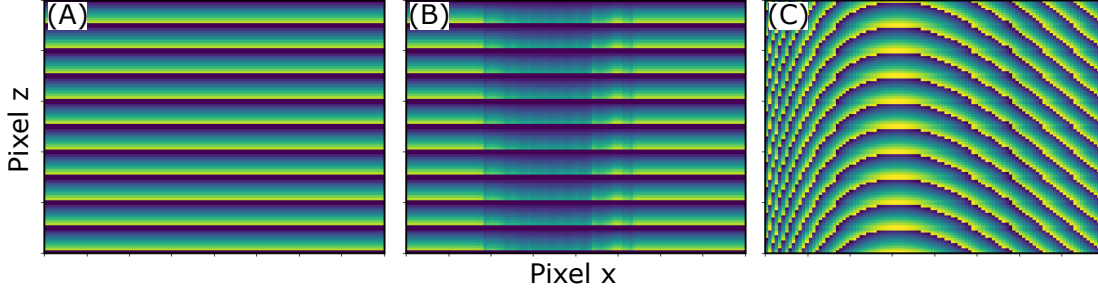


**Figure 4.7** – Color code images of the phase on the LC SLM in diffraction based shaping. (A) Neither phase, nor amplitude shaping. The beam is simply diffracted by the grating-like sawtooth pattern. (B) Amplitude shaping only. The decreased contrast in the center part of the spectrum reduces the amplitude in this spectral range. (C) Phase shaping only. The shifted sawtooth patterns result in phase shifts.

mirror, would focus the light in the Fourier plane also in the  $z$ -direction (figure 4.5). However, in order to be diffracted by the phase grating on the LC SLM, the light has to extend over several grating constants. This is achieved by the implementation of a cylindrical mirror.

One advantage of this method lies in the fact that the light that is reflected from the gaps between the LC SLM pixels is not diffracted and thus has a different direction of propagation than the shaped light. Consequently, it can be rejected with a spatial filter. Another benefit of this technique is, that for phase-only shaping, it is not even necessary to know the exact contrast in terms of  $\varphi$ , since this value is only needed to manipulate the amplitude. Complete phase control is even possible with a shaper that does not reach phase values of  $2\pi$ . In both cases of course, one has to accept intensity losses, as can be seen in equation 4.16 for  $c(\omega) < 2\pi$ .

## 4.2 Mathematical description of adaptive pulse shaping

A mathematical approach to the process of beam shaping is the concept of the effective frequency filter  $M_{\text{eff}}(\omega)$  with

$$E_{\text{out}}(\omega) = E_{\text{in}}(\omega)M_{\text{eff}}(\omega) \quad (4.17)$$

$$E_{\text{out}}(t) = E_{\text{in}}(t) * M_{\text{eff}}(t) \quad (4.18)$$

$E_{\text{in}}$  and  $E_{\text{out}}$  describe the complex electric field amplitudes of the input and output beams, respectively. The effective frequency filter is then connected to the complex transmittance function of the phase mask  $M(x)$  by a convolution with the spatial profile of the spectral component under consideration (Thurston et al., 1986). In case of a Gaussian beam mode, it looks like

$$M_{\text{eff}}(\omega) = \int dx M(x) \exp \left[ -\frac{2(x - \alpha\omega)^2}{\sigma_\omega^2} \right] \quad (4.19)$$

$$\alpha = \frac{dx}{d\omega} = -\frac{\lambda^2}{2\pi c} \frac{dx}{d\lambda}. \quad (4.20)$$

In equation 4.19,  $x$  is the spatial coordinate on the LC SLM. The design of an LC SLM is governed by pixels and not a smooth membrane, as it is in the case of a deformable mirror. Hence, the phase of every pixel can be set completely independent and a maximum phase change of  $2\pi$  is enough for complete phase control. However, due to the pixels and the inevitable gaps in between them,  $M(x)$  is a sum  $N$  of rectangular functions, with  $N$  being the number of pixels. This staircase approximation of the requested phase is then smeared out by the beam size  $\sigma_\omega$  of the beam on the phase mask (see equation 4.19). For a small focus however, the rectangular function is transferred to  $M_{\text{eff}}(\omega)$  and via a Fourier transform leads to the temporal effective filter function  $M_{\text{eff}}(t)$  (Weiner et al., 1992)

$$M_{\text{eff}}(t) \propto \left[ H(t) * \sum_{n=-\infty}^{\infty} \text{sinc}(N\pi \delta f(t - n/\delta f)) \right] \text{sinc}(\pi \delta f t) \quad (4.21)$$

with  $H(t)$  being the requested and smooth transfer function in the time domain and  $\delta f$  the frequency step between adjacent pixels. Equation 4.18 then relates the filter function and the incoming electric field to the beam that leaves the LC SLM. As derived by Weiner et al. (1992), if the spectrum is not clipped by the window of the LC SLM, one gets

$$E_{\text{out}}(t) \propto \left[ E_{\text{in}}(t) * \sum_{n=-\infty}^{\infty} H(t - n/\delta f) \right] \text{sinc}(\pi \delta f t) \quad (4.22)$$

The resulting intensity  $I(t)$  is a time comb of pulse replicas spaced by

$$\tau_{\text{rep}} = 1/\delta f \quad (4.23)$$

**Table 4.2** – Two parameter sets that were implemented in ray tracing simulations to obtain optical path lengths and ultimately spectral phase functions of the setups. Geometrical explanation of the parameters in figure 4.5.

Parameter	Value	Parameter	Value
Dispersive element	F2 glass prism	Dispersive element	Reflective grating
Apex angle	60°	Grating constant	3.3 $\mu\text{m}$
$\Delta$	18.8 cm	$\Delta$	14.4 cm
$f$	18.8 cm	$f$	14.4 cm
Spectral range	380–750 nm	Spectral range	380–750 nm

and modulated with an amplitude  $|\text{sinc}(\pi \delta f t)|^2$ . The zeros of the amplitude function coincide with the positions of the pulse replicas and suppresses them.

However, if  $M_{\text{eff}}(t)$  induces a shift in time to the pulses, the whole comb shifts and the replica get a finite amplitude. Equation 4.22 teaches us that any pixelated phase mask is only able to shape pulses in the range of  $\tau_{\text{rep}}$  if it is undesired to have an intensity modulation governed by  $|\text{sinc}(\pi \delta f t)|^2$ . For a spectrum reaching from  $\lambda = 400\text{--}750\text{ nm}$  and an LC SLM with 792 pixels like the Hamamatsu LCOS SLM X10468-01, the width of the sinc function is  $\tau_{\text{rep}} \approx 2.3\text{ ps}$ .

Since a finite beam size  $\sigma_\omega$  smears out  $M_{\text{eff}}(\omega)$ , at the costs of a worse frequency resolution, the effect of the pixelation gets weaker and thus also the replica pulses have smaller amplitudes (Thurston et al., 1986).

### 4.3 Ray tracing simulation of adaptive pulse shaping

Prior to experimental tests, I run a series of ray tracing simulations (ZEMAX) for different adaptive pulse shaping configurations. In doing so, I obtained the optical path length of each spectral component and ultimately the spectral phase. Table 4.2 shows the parameter sets that were implemented. The geometrical meaning of the parameters is explained in figure 4.5. In both parameter sets,  $\Delta$  equals  $f$  (equivalent to a  $4f$ -line) and this value is chosen, such that the full active area width (16 mm) of the LC SLM of our group (HAMAMATSU LCOS-SLM X10468-01) is illuminated with light in a spectral range from 380 nm to 750 nm.

The spectral phase functions, that are induced by passing through the adaptive shaping setup back and forth, are presented in figure 4.8 (A), where the blue graph

**Table 4.3** – Phase parameters extracted from ray tracing simulations for setups with prism and grating as dispersive elements. See table 4.2 for parameters of simulations.

Dispersive element	GDD	TOD
Prism	$1152 \text{ fs}^2$	$581 \text{ fs}^3$
Grating	$0.9 \text{ fs}^2$	$7 \text{ fs}^3$

corresponds to the setup with a F2 glass prism as dispersive element and the red graph, which is magnified by a factor 100, belongs to the setup with the grating. For the moment, it is assumed, that the phase mask induces no phase. In both graphs, the CEP and the GD were subtracted to stress the higher orders of the spectral phase. The insertion length of the prism was chosen to minimize material transmission, but still allowing a beam of 3 mm diameter to fully pass through. While the prism setup shows a large GDD, the grating setup's spectral phase is much smaller. Its small deviation from the zero-phase, that can be expected from a perfect  $4f$ -setup, can be explained with the angle  $\alpha$  of the cylindrical mirror in figure 4.5.

Fitting a fifth order polynomial around  $\lambda_0 = 520 \text{ nm}$  to the spectral phase  $\varphi(\omega)$  leads to the phase parameters in table 4.3. The material transmission in the simulated prism setup is approximately 5.3 mm. Since F2 glass has a group velocity dispersion of  $208 \text{ fs}^2/\text{mm}$  at  $\lambda_0 = 520 \text{ nm}$  (Schott, 2017), a GDD of approximately  $1100 \text{ fs}^2$  can be expected. This confirms, that the origin of the phase in the simulated prism setup is the additional material and is not due to geometrical properties of the beam path.

The next simulation treats the effect of the length  $\Delta$  in figure 4.5. Changing this value means displacing the setup from a  $4f$ -arrangement and thus inducing a spectral phase, similar to a grating or prism compressor (section 4.1.2). Figure 4.8 (B) shows the GDD at 520 nm for prism setups with different distances  $\Delta$ . Not surprisingly, for  $\Delta = f$ , the GDD is identical to one that can be expected from the material transmission (horizontal red line). As predicted by equation 4.12, the GDD behaves linear with the displacement of the concave mirror. Increasing the length  $\Delta$  leads to a reduction of the chirp. The insets in figure 4.8 (B) show, that  $\Delta \neq f$  yields a spatial chirp and thus a degradation of the spatial mode. For  $\Delta = f$ , the spatial mode degradation is negligible.

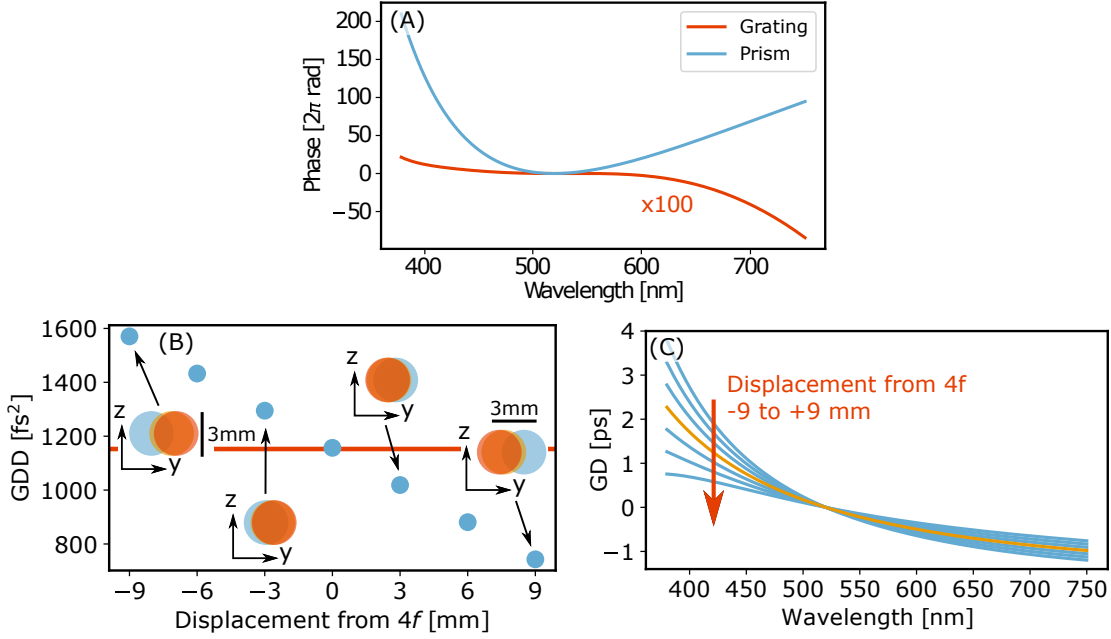


**Figure 4.8** – Ray tracing simulation on adaptive pulse shaping. (A) Spectral phase of the setups described in table 4.2. The graph for the grating is magnified by a factor 100 and linear phase components are subtracted. (B) Effects of shifting the distance  $\Delta$  (figure 4.5) away from a  $4f$ -setup with a prism as a dispersing element. Red line: GDD introduced due to prism material ( $1152 \text{ fs}^2$ ). Inlets: Spatial beam mode after the setup (blue:  $\lambda = 380 \text{ nm}$ , yellow:  $\lambda = 565 \text{ nm}$ , red:  $\lambda = 750 \text{ nm}$ ). For  $\Delta = f$ , the spatial chirp is negligible. (C) Spectral GD plots for displacements from  $\Delta = f - 9 \text{ mm}$  to  $\Delta = f + 9 \text{ mm}$ , as in subfigure (B). Yellow:  $\Delta = f$

Figure 4.8 (C) depicts the spectral GD for the same geometrical configurations as in subfigure (B), namely  $\Delta = f - 9 \text{ mm}$  to  $\Delta = f + 9 \text{ mm}$ . In summary one can say that by shifting the length  $\Delta$ , a negative chirp can be induced, however, it is not possible to compensate for the GDD that is introduced due to the material of the prism without degrading the spatial mode significantly.

As a next step, the shaping capability of a membrane deformable mirror is considered. Therefore, the phase from figure 4.8 (A) is converted into an optical path length  $\delta$  according to

$$\delta = \frac{\varphi \lambda}{2\pi}. \quad (4.24)$$

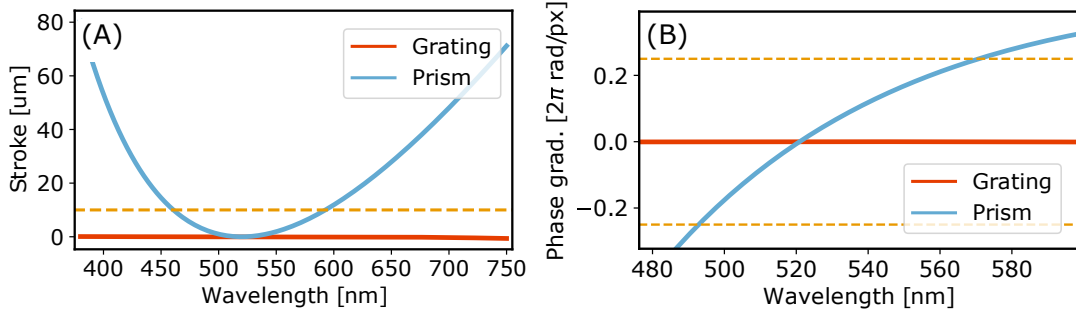


**Figure 4.9** – Shaping capability of deformable mirrors (A) Membrane deformable mirror. Stroke that is necessary to compress the phase from figure 4.8 (A). Yellow: Maximum stroke of deformable mirror by OKOTECH. (B) Pixelated deformable mirror. Phase gradient per pixel for a bandwidth 495–570 nm with pixelated deformable mirror by BOSTON MICROMACHINES (96 pixels). Yellow: Limit for  $\pm 2\pi$  rad/4 pixels.

These optical path length data are plotted in figure 4.9 (A) in red (grating setup) and blue (prism setup) and compared with the maximum stroke of a membrane deformable mirror by OKOTECH, which is 10  $\mu\text{m}$  (yellow). Note that the grating data are not magnified in this diagram. It can be seen that, while the deformable mirror can compensate the much smaller GDD of the grating setup with ease, this is only possible for a limited spectral range from 460–590 nm in the case of the prism as a dispersing element.

In contrast to a membrane system, phase wrapping can be applied, when a pixelated device is used and the shaping capability is then limited by the gradient of the phase per pixel. For this study, it is assumed that a pulse can only be shaped, if there are at least four pixels per  $2\pi$  rad. For the data from figure 4.8 (A), this gradient is plotted in figure 4.9 (B). Therefore, the specifications of a device from BOSTON MICROMACHINES with 96 pixels were assumed. If the spectrum is chosen to be 495–570 nm, the device reaches its limits at the edges of the spectrum (prism setup) and a broader spectrum is not compressible with these specifications.

To conclude this series of simulations, it can be said, that it is possible to build a  $4f$  adaptive shaping setup with a prism as a disperser that yields a good spatial mode and – for geometrical reasons – does not add any GDD to the pulses.

However, due to the additional material, using a prism as a dispersive element induces a chirp that has to be compensated for. Partly, this can be achieved by a

shift of the collimating mirror, but this decreases the spatial mode quality of the beam. If the additional GDD should be compensated with commercially available deformable mirrors, one has to accept bandwidth restrictions.

Despite these drawbacks, since the throughput of a prism in the Brewster-angle condition is significantly higher than the one of a grating, and furthermore, the prism dispersion law allows for a better shaping in the high-frequency part of the spectrum, choosing a prism as a disperser can be useful in some occasions. In this case, a reduction of the beam diameter to decrease the minimum insertion length of the prisms or a pre-compression with, e.g. a CMP can be a helpful to reach Fourier-limited pulses.

## 4.4 Pulse characterization techniques

The temporal characterization of ultrashort pulses in the optical regime necessitates sophisticated techniques, since currently available detectors are not fast enough for a direct monitoring. Most of these techniques base on a gating or self-gating procedure in a nonlinear optical medium. In the following, two approaches that were deployed in the present project, will be presented. In both, the result is a signal  $S(t, \omega)$  from which the GD( $\omega$ ) and subsequently the spectral phase  $\varphi(\omega)$  can be extracted through an integration.

$$\varphi(\omega) = \int_0^\omega \text{GD}(\omega') d\omega' + \text{const.} \quad (4.25)$$

### 4.4.1 Cross-phase modulation

The cross-phase modulation (XPM) is a nonlinear phenomenon of third order that is based on the optical Kerr effect (OKE) effect. It is typically observed in transient-absorption spectroscopy (TAS) experiments, where a pump and a probe pulse are focused into the same spot in a sample and their relative delay is scanned.

Due to the third order susceptibility  $\chi^{(3)}$  of a material, an intensity  $I(t)$ , e.g. of the pump pulse, induces a time-dependent refractive index that follows

$$n(t) = n_0 + n_2 I(t), \quad (4.26)$$

with the linear refractive index  $n_0$  and the second-order nonlinear refractive index

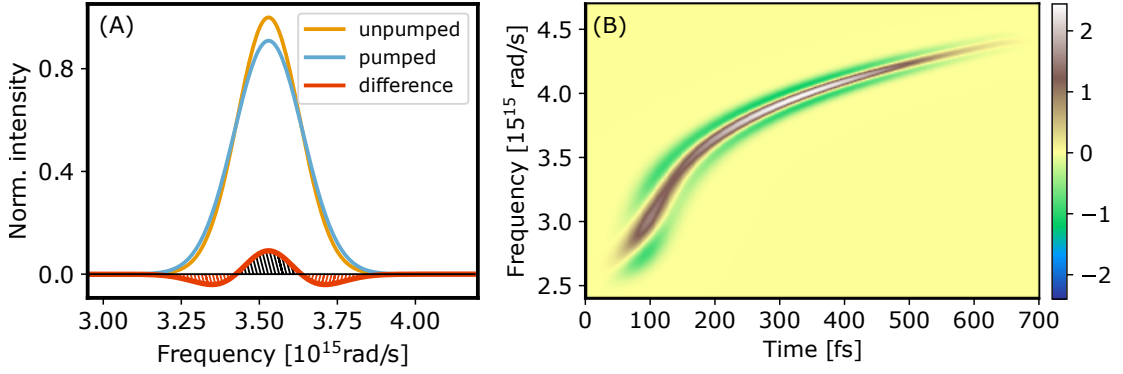


**Figure 4.10** – Simulation of the XPM of a chirped pulse with a Gaussian spectrum. (A) XPM at one delay (red) together with the pumped and unpumped spectrum (blue and yellow). Hatched: Positive and negative area under XPM signal. (B) Simulated spectrogram with the XPM of a probe pulse with a strong FOD. The pump pulse is assumed to be a Gaussian with width  $\sigma = 16$  fs

$n_2 \propto \chi^{(3)}$ . This phenomenon is called OKE and becomes significant only with very strong intensities, as they are given in spectroscopic experiments with ultrafast pulses.

The change of the refractive index is not only seen by the pump itself, but also by a probe pulse if it overlaps spatially and temporally with the pump in the nonlinear medium. The modulation of the refractive index yields a phase shift

$$\varphi_{\text{OKE}}(t) = -\frac{2\pi}{\lambda} \delta_{\text{OKE}}(t) = -\frac{2\pi}{\lambda} n_2 I(t) l, \quad (4.27)$$

where  $\delta_{\text{OKE}}$  is the optical path length, that is induced by the OKE,  $l$  is the length of the pulse overlap in the material and  $\lambda$  is the wavelength of the probe pulse. The instantaneous frequency of the probe is given by the time derivative of the phase

$$\omega(t) = \frac{d\varphi}{dt} = \omega_0 + \frac{d\varphi_{\text{OKE}}(t)}{dt} = \omega_0 - \frac{2\pi}{\lambda} n_2 l \frac{dI(t)}{dt}. \quad (4.28)$$

According to equation 4.28, a temporal overlap of the probe with the rising and the falling edge of the pump leads to a broadening of the probe spectrum (figure 4.10 (A)). Subtracting the probe spectrum in the presence of the pump  $S_{\text{pu}}(\omega)$  from an unpumped one  $S_{\text{up}}(\omega)$  and normalizing the difference with their average,



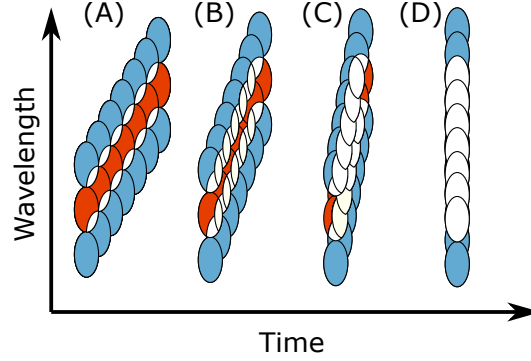


**Figure 4.11** – Explanatory sketch for weaker XPM traces in the case of better pulse compression due to overlap of positive and negative contributions. (A) to (D) Pulses with increasing compression. Blue: Areas with negative XPM signal (hatched red in figure 4.10). Red: Areas with positive XPM signal (hatched black in figure 4.10). White: Overlap of positive and negative areas.

as it is done in a TAS experiment, leads to the red signal in figure 4.10 (A).

$$\text{TA}(\omega) = \frac{2(S_{\text{up}}(\omega) - S_{\text{pu}}(\omega))}{2.3(S_{\text{up}}(\omega) + S_{\text{pu}}(\omega))} \quad (4.29)$$

The normalization factor 2.3 is due to a switch from  $\log_{10}$  to  $\ln$  in the derivation of the TAS signal (Nazari, 2018).

Since this effect is instantaneous, by scanning the pump temporally over the whole probe pulse, the group delay of each spectral component can be derived with that method. A simulated scan with a pump pulse that is considered to have a Gaussian shape with a width  $\sigma = 16$  fs and a probe with a strong FOD and a spectrum from 400 to 700 nm is shown in figure 4.10 (B).

In the range around  $\omega = 3.3 \cdot 10^{15}$  rad/s in figure 4.10 (B), the XPM trace is a bit weaker, compared with the rest of the spectrum, which is due to the better compression of the pulse in that spectral range. This effect is sketched in figure 4.11, where four XPM traces with different compression states are depicted. While the blue ellipses indicate regions of negative signal in the spectrogram, the red color indicates a positive signal (see hatched areas in figure 4.10 (A)) White areas correspond to an overlap of negative and positive parts, in which the overall signal is either reduced or even zero. For uncompressed pulses, the negative and positive components are clearly distinguishable (A), whereas with improving compression, positive and negative areas overlap more and more and thus cancel

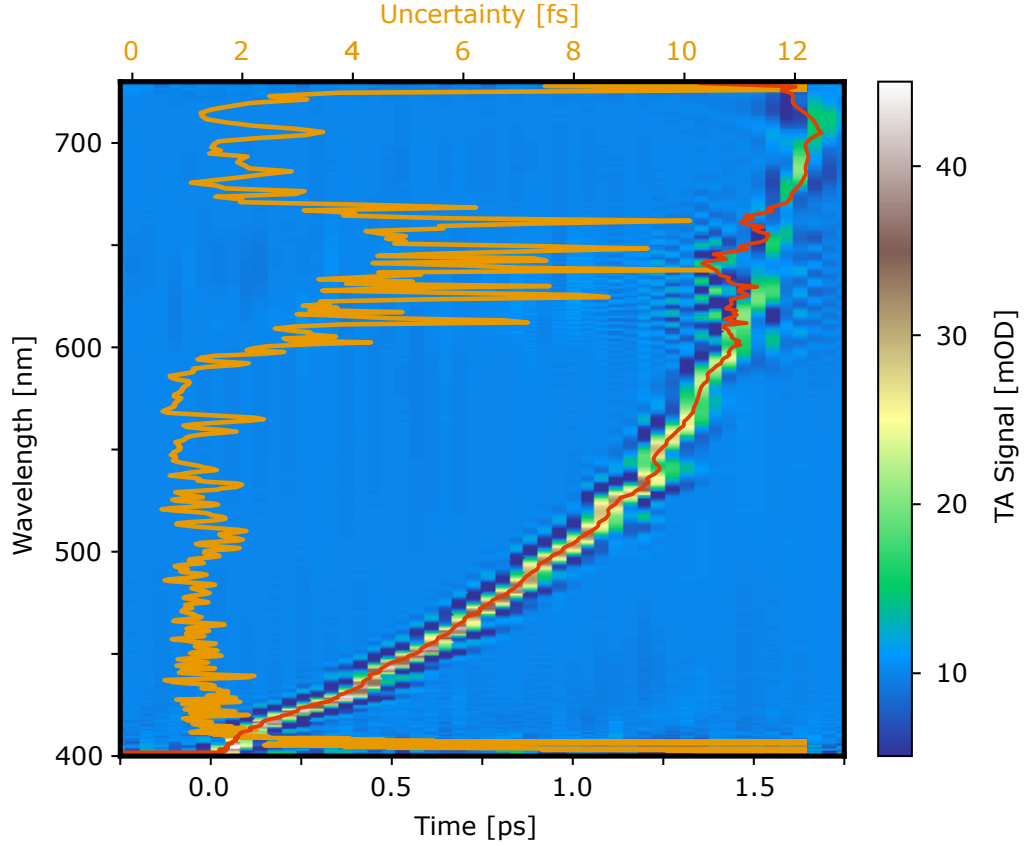


**Figure 4.12** – XPM measurement of a supercontinuum (SC) spectrum, generated in ethanol. Colorcode: TAS signal. Red: Result of the GD characterization. Yellow: Uncertainty of the GD characterization.

out. The overall signal strength of an XPM trace is consequently much weaker for a compressed pulse (D), than for pulses with a large GDD.

For the sake of energy conservation, the surface areas under the pumped and the unpumped spectra in figure 4.10 are identical and thus the negative area and the positive area in the XPM are identical, as well. Accordingly, in the case of a perfectly compressed pulse with a flat spectrum, the XPM vanishes completely, except for the edges of the spectrum.

An experimental XPM is displayed by the color code in figure 4.12. For this measurement, a supercontinuum (SC) with a spectrum from 400 nm to 700 nm was generated in a calcium fluoride ( $\text{CaF}_2$ ) crystal. A NOPA served as a pump source for pulses from 610 nm to 660 nm with a pulse energy of 20  $\mu\text{J}$  (see section 4.5.1 for more details on the NOPA). The XPM was generated in ethanol that

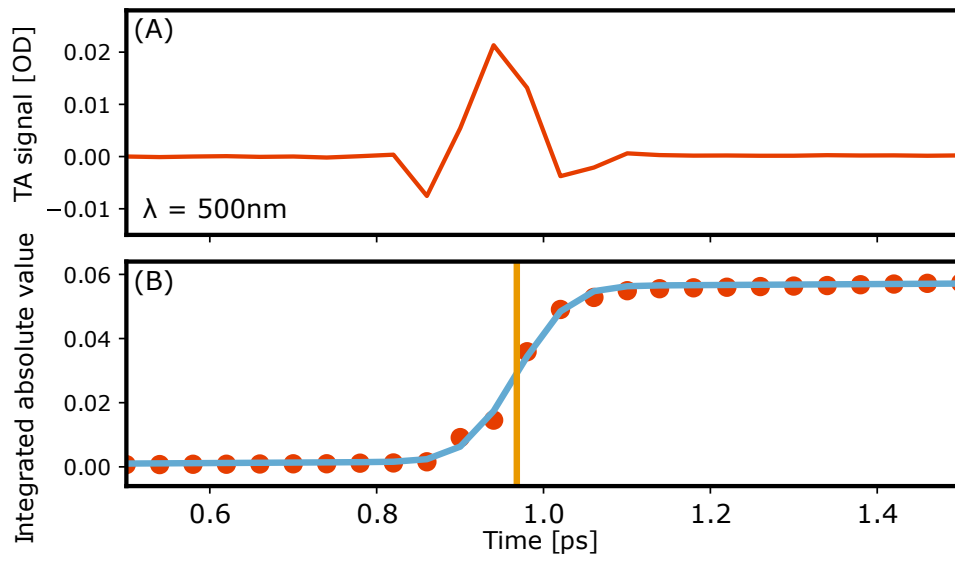


**Figure 4.13** – GD extraction from XPM trace. (A) A time trace of figure 4.12 at  $\lambda = 500\text{ nm}$ . (B) Red: Data from (A) if processed as in equation 4.30. Blue: Error function with slope fitted to the red data. Yellow: Resulting position of the error function.

was flowing through a cuvette of 200  $\mu\text{m}$  thickness. It can be clearly seen, that the probe pulse has a strong GDD  $\approx 740 \text{ fs}^2$ , that corresponds to a transmission through about 13 mm fused silica glass. The signal-to-noise ratio (SNR) in the range of 610 nm to 660 nm is much worse due to pump scattering.

One advantage of this technique is, that only a pump probe setup is needed for it. Furthermore, no complicated reconstruction algorithm as in other methods is necessary to qualitatively identify the chirp of a pulse, since the spectrogram already depicts the spectral GD function. In addition, it is possible to characterize probe pulses of weak intensity and/or with a bad compression, as it is shown in figure 4.12, if a compressed, high intensity pump pulse is available. The reason for that is, that the nonlinear refractive index of the OKE is induced by the pump and not by the probe pulse.

The relatively weak signal strength is a disadvantage of this approach. Consequently, for pump pulses that spectrally overlap with the probe, scattering rejection becomes a challenging issue (as can be seen in the range of 610 nm to 660 nm in figure 4.12). This is why, in this work, XPM was only used as a cross-correlation method in combination with a compressed and narrow pump pulse. For auto-correlation, TGFROG, which is described in section 4.4.2, was used.

### Group delay quantification

In order to develop an automated pulse compression procedure with means of adaptive shaping, it is crucial to establish a method to quantify the GD of an XPM trace. However, while it is intuitive to do a qualitative evaluation on the chirp of a pulse with an XPM trace, a quantitative analysis is more difficult. To get a function  $\text{GD}(\omega)$  from an XPM measurement, it is necessary to determine the center of the XPM signal for every frequency. Since this signal contains both, positive and negative contributions that are not always as symmetric as in figure 4.10, precisely quantifying  $\text{GD}(\omega)$  can be challenging and signals with a weak SNR further increase that difficulty.

Within the presented work, different methods to achieve that, like standard peak finding methods or fitting procedures with one or two Gaussian functions, have been tested. The results were unsatisfying, either due to too many fitting parameters (two Gaussians) or because the method did not consider a possible asymmetry in the XPM function (peak finding and single Gaussian fit). For that reason, within this work, a new method was developed that works better and is explained

in the following.

The procedure is presented in figure 4.13, for a single time trace  $S_\omega(t)$  of figure 4.12 at  $\lambda = 500$  nm. To consider negative and positive contributions to the XPM in the same way, we use the absolute value of  $S_\omega(t)$  and integrate it.

$$S_\omega(t) \rightarrow \int_{-\infty}^t dt' |S_\omega(t')| \quad (4.30)$$

The result is a step function that is due to the integration of the Gaussian-like  $|S_\omega(t)|$  and a linear slope that arises from the integration of the absolute value of the noise. In figure 4.13 (B), the integrated data are plotted in red. The blue curve is an error function together with a slope, as shown in equation 4.31, fitted to these data. The position  $t_0$  (yellow) yields the  $\text{GD}(\omega)$  for this specific wavelength,  $m$  is an indicator for the noise and  $\sigma$  is the width of the error function.

$$A \text{erf}((t - t_0)/\sigma) + mt \quad (4.31)$$

Finally, by applying this procedure to every frequency of an XPM trace, a  $\text{GD}(\omega)$  function can be extracted. In the case of the data in figure 4.12,  $\text{GD}(\lambda)$  is depicted by the red curve and the uncertainty (standard deviation) of the error function fit is given by the yellow curve. The uncertainty for these data is about 1 fs, whereas the results in the spectral region of the pump scattering (610–660 nm) are a bit worse.

#### 4.4.2 Transient grating FROG

The term frequency-resolved optical gating (FROG) refers to a collection of cross- or auto-correlation techniques. They all work through different kinds of nonlinear mixing processes of two or more replicas of the pulse under investigation in a nonlinear crystal. A comprehensive review on these methods is given by Trebino et al. (1997). In the current work, transient grating (TG) FROG is deployed and will thus be discussed in the following.

TG FROG necessitates three replicas of the investigated pulse that are ideally arranged in a box-CARS geometry, since this leads to a phase-matched emission of the signal (see sections 2.1.7 and 2.2.3). All three pulses overlap in a medium with a third-order susceptibility  $\chi^{(3)}$  and two of them (e.g. A and B in figure 2.6) overlap in time ( $t_1 = 0$ ). The constructive interference of the incident pulses cre-

ates a spatial refractive index grating in the material, due to the OKE (equation 4.26), as it is sketched in figure 4.14. The colors red and blue refer to two different points in time. The lines orthogonal to the direction of propagation indicate the maxima of the electric field of the beams A and B, whereas the circles are the intersections of these lines in the corresponding color, namely the points of constructive interference. It can be seen that, as time passes and the light propagates, the points of constructive interference move along the yellow lines, but their distance among themselves remains unchanged. These yellow lines indicate the induced grating with a vector  $\vec{k}_g = -\vec{k}_A + \vec{k}_B$ , which diffracts the third pulse into the direction  $\vec{k}_{TG} = -\vec{k}_A + \vec{k}_B + \vec{k}_C$ . In a box-CARS geometry this corresponds to the direction of the fourth corner. The diffracted light, which only occurs if there is a time overlap between all three pulses, is then detected in a spectrometer.

For a given delay between the pulse B and the first two, the emitted signal intensity can mathematically be described as (Trebino et al., 1997)

$$I_{TG}(\omega, \tau) = \left| \int_{-\infty}^{\infty} dt E_A^*(t) E_B(t) E_C(t - \tau) e^{-i\omega t} \right|^2. \quad (4.32)$$

An experimental TG FROG trace is displayed by the color code in figure 4.19.

In contrast to other FROG techniques, TG FROG traces do not necessitate reconstruction algorithms, but they immediately provide the time structure of the pulse. Its non-collinear nature facilitates scattering suppression and since it is phase-matched, the signal is relatively strong and has a broader acceptance bandwidth. A drawback is the more complicated experimental geometry with three beams, but since the presented project includes a box-CARS geometry for the spectroscopy experiment, this phase retrieval method can be run without any additional effort.

### Group delay quantification

Quantifying the group delay is much simpler in the case of a TG FROG, since there are only positive contributions to the signal. Therefore, the center of the

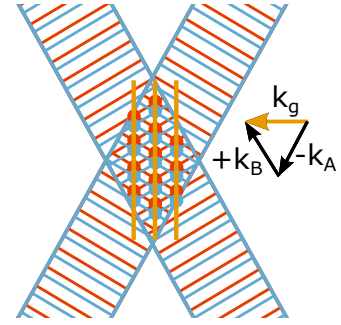


**Figure 4.14** – Induction of the transient grating through two pulses incident at  $\vec{k}_A$  and  $\vec{k}_B$ .  $\vec{k}_g = -\vec{k}_A + \vec{k}_B$  is the wave vector of the grating (yellow).

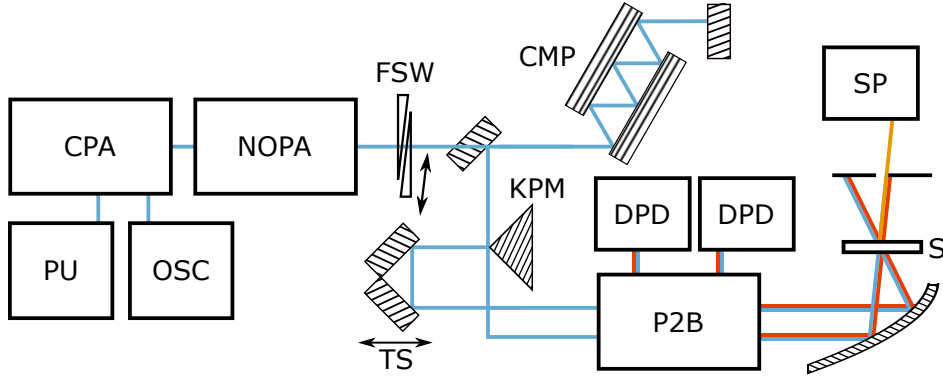


**Figure 4.15** – Schematic of the FT FWM spectroscopy setup. PU: Pump laser. OSC: Seed oscillator. CPA: Chirped pulse amplification. NOPA: Noncollinear optical parametric amplifier. FSW: Fused silica wedges. CMP: Chirped mirror pair. KPM: Knife-edge prism mirror. TS: Translation stage (150 mm). P2B: pump-probe-to-box-CARS element. DPD: Differential phase determination setup. S: Sample position. SP: Spectrometer, as described in figure 3.1. Blue beams are in the figure plane, red ones behind it. Yellow: Signal, potentially heterodyned with LO.

signal for every wavelength can be obtained, by standard peak finding procedures. In the presented work, a Gaussian function was fitted to the data.

## 4.5 Pulse generation and compression

### 4.5.1 NOPA

During this work, different techniques for pulse compression were implemented and tested. First, the results of the NOPA compression are presented. The experimental setup that was used for that issue and also, later in this thesis, for FWM spectroscopy experiments, is illustrated in figure 4.15.

A Ti:sapphire chirped pulse amplifier (COHERENT LEGEND ELITE) is seeded by a Kerr lens mode-locked Ti:sapphire oscillator (KAPTEYN-MURNANE LABORATORIES,  $\lambda = 791 \text{ nm}$ ,  $\text{FWHM}_\lambda = 15 \text{ nm}$ ,  $f_{\text{rep}} = 80 \text{ MHz}$ ) and pumped by a frequency-doubled Nd:YLF laser (QUANTRONIX DARWIN-527,  $\lambda = 527 \text{ nm}$ ,  $P_{\text{ave}} = 19.5 \text{ W}$ ). All experiments within this work are executed at repetitions rates of either 3.5 kHz or 5 kHz. This system generates pulses at  $\lambda = 800 \text{ nm}$  with pulse energies of 500  $\mu\text{J}$  and pulse durations of 100 fs.

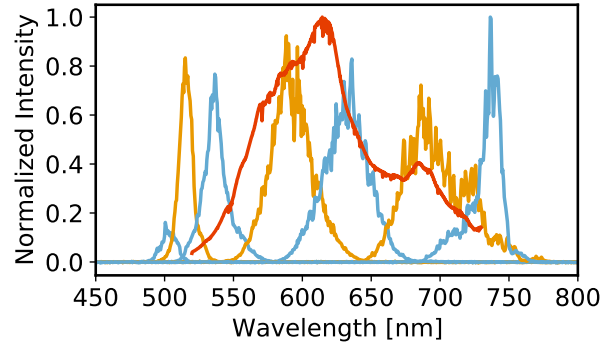


**Figure 4.16** – Typical NOPA spectra. Red: Broadband spectrum. Blue and yellow: Different intermediate spectra.

Inside a commercial NOPA (LIGHT CONVERSION TOPAS WHITE), one portion of this light is used to generate SC pulses, whose GD can be varied with a grating compressor and a phase mask. The second portion of the fundamental light is frequency-doubled and used as a pump in the seeded down-conversion process. A more detailed description of the processes in a NOPA can e.g. be found in (Cerullo and De Silvestri, 2003).

A peculiarity of the NOPA, that was used for the current work, is the possibility to shape the GD of the SC pulses before the amplification. In doing so, the spectral components of the SC, that temporally overlap with the pump pulse in the nonlinear medium can be selected (figure 4.17). This allows to run this NOPA with bandwidths between 10 nm (large GDD in SC) up to 250 nm (small GDD in SC) in the range 500–760 nm. In the case of a narrow or intermediate bandwidth, the center wavelength can be chosen with the delay between the SC and the pump pulse. Some typical NOPA spectra are plotted in figure 4.16. The red spectrum is in the broadband configuration with a bandwidth of over 200 nm, whereas blue and yellow show different intermediate bandwidths. Achievable pulse energies are typically 15–20  $\mu\text{J}$ .

Subsequently, the NOPA beam passes a chirped mirror pair (CMP), which is in more detail described in section 4.1.4, with 28 reflections. This element ideally slightly overcompresses the pulses, such that the Fourier limit can be reached through the preceding step, where the beams are transmitted through a pair of fused silica wedges. They are arranged anti-parallel, as depicted in figure 2.10, and one of them is mounted on a manual translation stage. Like that, moving this wedge does not lead to a significant change of the beam path. The wedges



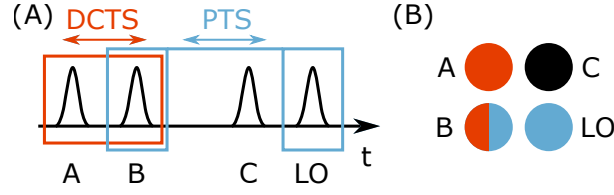


**Figure 4.18** – (A) The DC motor translation stage (DCTS, figure 4.15) delays the pulses A and B with respect to C and LO. The PTS inside the P2B element (PTS, figure 3.3) delays the pulses B and LO with respect to A and C. (B) Spatial arrangement of the beams before the focusing off-axis parabolic mirror. Colors indicate the translation stage, that delays the respective pulse.

have an internal angle of  $4^\circ$  and the translation resolution is about  $10\text{ }\mu\text{m}$ . This is small enough to add fused silica in steps of  $700\text{ nm}$  for fine compression of the laser pulses.

Without adding additional chirp, a knife-edge prism mirror splits the beam into two replicas, of which one can be delayed with a retroreflector on a translation stage (PI M-406.6PD, DC motor,  $150\text{ mm}$  travel range,  $250\text{ nm}$  minimum incremental motion). In the following they propagate on parallel trajectories and enter the P2B element, that is in more detail described in section 3.2. Afterwards, the four pulses, that are arranged in the box-CARS geometry are focused into the sample position by an off-axis parabolic mirror with an effective focal length of  $f_e = 100\text{ mm}$ . In the case of a TG FROG measurement, a sapphire slab of  $250\text{ }\mu\text{m}$  thickness is placed in the sample position. After the sample, spatially, only the components with the wave vector  $\vec{k}_{\text{LO}} = -\vec{k}_A + \vec{k}_B + \vec{k}_C$  are selected to be sent to the home-built spectrometer (figure 3.1).

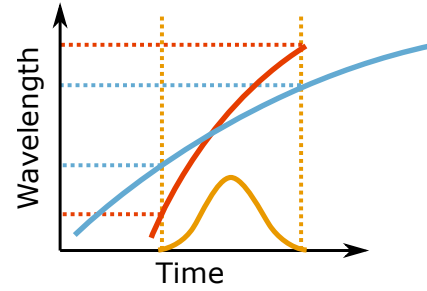


**Figure 4.17** – Sketch of bandwidth selection in NOPA. Yellow: Time structure of pump pulse. Red and blue: Different GDs of SC pulses lead to narrow (blue) and broad (red) bandwidth of amplified pulses.

In this configuration, which is used for the TG FROG measurements, but also for the FWM spectroscopy experiments later in this work, a motion of the DC motor translation stage delays the pulses A and B, whereas the PTS inside the P2B element shifts the pulses B and LO (figure 4.18).

A TG FROG measurement does not require heterodyne detection, so the LO is blocked for the time being. There are two proceedings that result in a TG FROG trace. First, using the PTS to set the delay between pulses A and B to zero and thus creating a spatial refractive index grating, as described in section 4.4.2. The DC motor translation stage is then used to scan beam C temporally through this grating. The TG FROG trace is then identical to equation 4.32. The data in figure 4.19 (A) were measured with that approach. Since the target step size of 2 fs is close to the minimum increment of the stage, the time steps are inconstant throughout the measurement. However, since they are measured with the feedback loop of the translation stage, they are reliable and correspond to the actual delay  $t_2$ .

It can clearly be seen, that there is a positive GDD in the pulses. Fitting a Gaussian function to the TG FROG trace of every wavelength leads to a GD function with a GDD of approximately  $13.5 \text{ fs}^2$  around 650 nm. This value corresponds to a thickness of 270  $\mu\text{m}$  of fused silica glass and can thus with ease be compensated by the fused silica wedges.

For the data that are shown in figure 4.19 (B), the fused silica wedges were used to optimize the material transmission for the best possible compression and the second proceeding was applied. In this case, the DC motor translation stage, instead of the PTS was used to set the delay between pulses A and C to zero in order to generate the spatial refractive index grating. Subsequently, pulse B was scanned temporally through the grating with the PTS to generate a TG signal. In that case, the mathematical description of the trace (equation 4.32) has to be modified to

$$I_{\text{TG}}(\omega, \tau) = \left| \int_{-\infty}^{\infty} dt E_A^*(t) E_B(t - \tau) E_C(t) e^{-i\omega t} \right|^2. \quad (4.33)$$

Since pulses A, B and C are replicas of the same pulse, however, equations 4.32 and 4.33 can be considered identical. Obviously, the second approach to achieve a TG FROG results in a much smoother trace, which is due to the smaller increment of the PTS.

Furthermore, it can be said that by adjusting the setting of the fused silica wedge pair, a much better compression was possible. While in 4.19 (A), the integration of the NOPA trace along the wavelength axis yields a pulse length of  $13.0 \pm 0.7 \text{ fs}$ ,  $8.1 \pm 0.1 \text{ fs}$  are achieved in figure 4.19 (B).

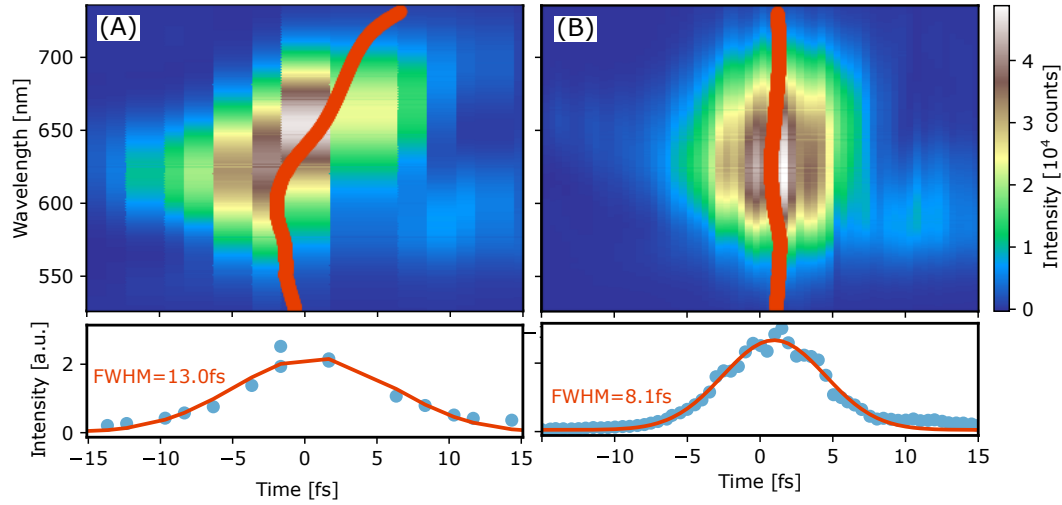


**Figure 4.19** – Top row: TG FROG traces of NOPA pulses (color plots) with  $GD(\omega)$  in red. The TG signal was generated in sapphire slabs of 250  $\mu\text{m}$  thickness. Bottom row: Integration of FROG traces along wavelength axis (blue scatter plot). Red: A Gaussian function fitted to the integrated data. (A) 28 reflections on CMP, positive chirp of  $GDD(650\text{ nm}) \approx 13.5\text{ fs}^2$ . Gaussian function fitted to  $\text{FWHM} = 13.0 \pm 0.7\text{ fs}$  (B) Identical to (A), but material transmission through fused silica wedge pair was optimized. Gaussian function fitted to  $\text{FWHM} = 8.1 \pm 0.1\text{ fs}$ .

### 4.5.2 Supercontinuum

In this experiment, I want to show the capability of broadband pulse compression in an adaptive scheme with an iterative approach. The simulations in section 4.3 indicate, that for the compression in a prism-based adaptive shaping setup with spectrally broad pulses, due to the additional material of the prism, a pre-compression is necessary. The LC SLM, that was used for this experiment (HAMAMATSU LCOS-SLM X10468-01), however, has a front face made of a BK7 glass plate, with a thickness of 3 mm, which leads to additional 6 mm of glass transmission. The glass plate thus introduces an even higher chirp than the prism, which in total is too much. To enable a compression in this configuration, I replaced the prism by a grating.

The setup was used as depicted in figure 4.20. The laser system including the chirped pulse amplification is identical to section 4.5.1. Afterwards, 90% of the light is reflected to the NOPA that was described in section 4.5.1, as well. However, the configuration of the NOPA is more narrow now, such that the bandwidth

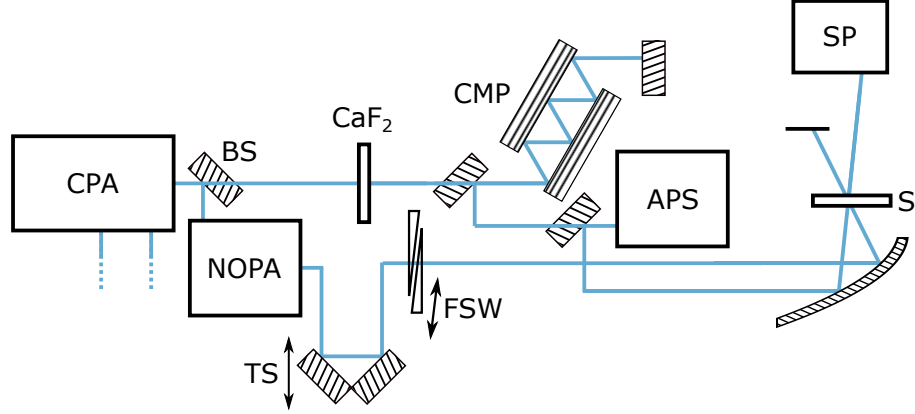


**Figure 4.20** – Schematic of the supercontinuum (SC) compression setup. CPA: Chirped pulse amplification. BS: Beam splitter with 90% reflection. NOPA: Non-collinear optical parametric amplifier. TS: DC motor translation stage (150 mm). FSW: Fused silica wedges.  $\text{CaF}_2$ : calcium fluoride crystal for SC generation. CMP: Chirped mirror pair. APS: Adaptive pulse shaping setup. S: Sample position. SP: Spectrometer, as described in figure 3.1

of the generated pulses is from 650 nm to 700 nm. In contrast to the broad pulses, that were used in section 4.5.1, these narrow-band NOPA pulses show a negative GDD, which can be compressed simply with transmission through fused silica. As before, these pulses can be delayed with a DC motor translation stage. These pulses serve as pump pulses in an XPM phase retrieval setup.

The 10% of the fundamental light, that is transmitted by the beam splitter is focused into a 5 mm  $\text{CaF}_2$  crystal and through a series of nonlinear processes like self-focusing and self-phase modulation generates SC pulses with a bandwidth that spans from 400 nm to 700 nm. A detailed description of the generation of SC pulses is given by Dubietis et al. (2017). The beam passes the CMP with 28 reflections for pre-compression and is subsequently sent into an adaptive pulse shaping setup, as it is described in section 4.1.5 with the parameters in table 4.4.

For this measurement, the LC SLM was run in the diffraction-based shaping mode. In the first measurement, the phase of the LC SLM was set to zero and an XPM signal was generated in a sapphire slab of 250  $\mu\text{m}$  thickness (figure 4.21 (A)). The spectral phase that was retrieved with the GD extraction method (red data in the spectrogram) as explained in section 4.4.1 and equation 4.25 was then plugged into the LC SLM to get an almost compressed pulse (figure 4.21 (B)). Small inaccuracies were then corrected by repeating this process in a second iteration

**Table 4.4** – Parameter set of adaptive shaping setup that was experimentally implemented to compress SC pulses iteratively.

Parameter	Value
Dispersive element	Reflective grating
Grating constant	3.3 $\mu\text{m}$
$\Delta$	18.8 cm
$f$	18.8 cm

(figure 4.21 (C)). The yellow line in figure 4.21 is a vertical reference line, which helps to see that there is still some improvement from figure 4.21 (B) to (C).

The improving pulse compression from figure 4.21 (A) to (C) not only reflects in the vertical shape of the GD, but also in the reduced intensity of the XPM. This effect is explained in figure 4.11 and the related discussion.

## 4.6 Conclusion

In the beginning of this chapter, the different parameters of the spectral phase of a light pulse were introduced and their physical meaning was explained. Subsequently, different ways to take an influence on this phase, were presented and the main focus was put on adaptive shaping. The field of adaptive shaping was extended by the concept of a prism as a dispersive element with the advantage of an improved efficiency and a better dispersion in the high-frequency range of the spectrum.

Ray tracing simulations on adaptive shaping showed, that using a prism does not lessen the beneficial properties of a  $4f$ -scheme in terms of the spatial beam mode and the GDD of the pulses. However, the additional material introduces a chirp, that has to be minimized with a small beam diameter and insertion length of the prism or compensated with a pre-compression scheme, e.g. a CMP. If the additional chirp due to the prism material should be compensated with commercially available deformable mirrors, one has to accept restrictions in terms of the bandwidth. Independent from the dispersive element, positive and negative chirp can be added to the phase by changing the distance  $\Delta$  between the dispersive element and the collimating mirror. However, only in the case of  $\Delta = f$ , the setup yields a perfect spatial beam mode.

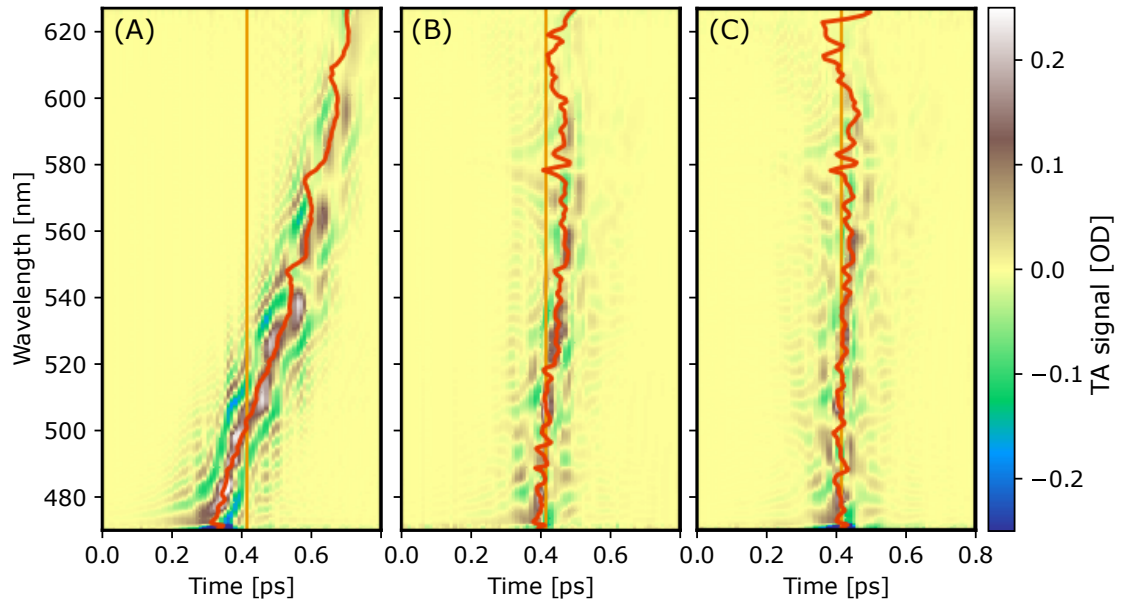


**Figure 4.21** – XPM of SC pulses, generated in a 250  $\mu\text{m}$  sapphire slab and pre-compressed via 28 reflections on the CMP, described in figure 4.4. (A) LC SLM phase set to zero. (B) and (C) Iterative compression by retrieving the phase from preceding XPM measurement and adding it to the LC SLM. Yellow: Vertical line for reference. Red:  $GD(\lambda)$ .

Afterwards, with TG FROG and XPM, two pulse characterization techniques, that were used during this work, were explained. The first one is suitable for intense pulses that are already close to the Fourier limit, whereas the latter is more appropriate for the characterization of uncompressed pulses, also with lower intensity. For an automated phase extraction from an XPM trace, a new algorithm was introduced and also applied as part of an iterative compression of SC pulses in an adaptive shaping setup with an LC SLM. TG FROG was used to characterize broadband NOPA pulses that were compressed with a combination of a CMP and a pair of fused silica wedges.





## Towards FT FWM Spectroscopy Experiments

This chapter shows the first results of an FT FWM spectroscopy measurement that was realized with the approach of SSI, as described in section 2.2.6. Furthermore, some preliminary outcomes like a TG spectroscopy experiment and steps that were made to achieve an appropriate precision in single-shot phase retrieval are presented. Throughout the whole chapter, the experimental setup is identical to the one, used for the TG FROG measurements in chapter 4 (figure 4.15).

### 5.1 Homodyne TG spectroscopy

For the first measurement, a resonant TG signal is generated in Rhodamine 800, dissolved in ethanol. Rhodamine 800 is a laser dye, with an absorption maximum at  $\lambda = 682\text{nm}$ , as can be seen in figure 5.2. It was chosen, since its absorption bandwidth overlaps well with the spectrum of the light from the NOPA and it shows a large natural lifetime of more than one nanosecond (Alessi et al., 2013; Abugo et al., 2000).

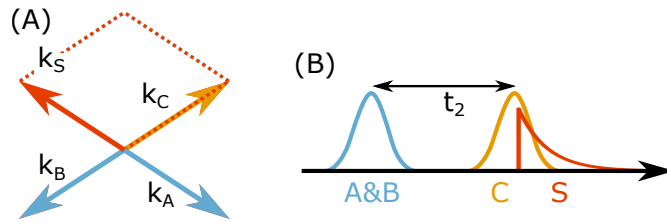


**Figure 5.1** – TG experiment. (A) Phase matching in the box-CARS geometry. Blue: Projections of  $k$ -vectors of beams A and B on the plane that is perpendicular to the direction of propagation. Yellow: Beam C. Red: TG signal  $\vec{k}_S = -\vec{k}_A + \vec{k}_B + \vec{k}_C$  (B) Pulse sequence with  $t_1 = 0$  and the signal being emitted immediately after the third interaction.

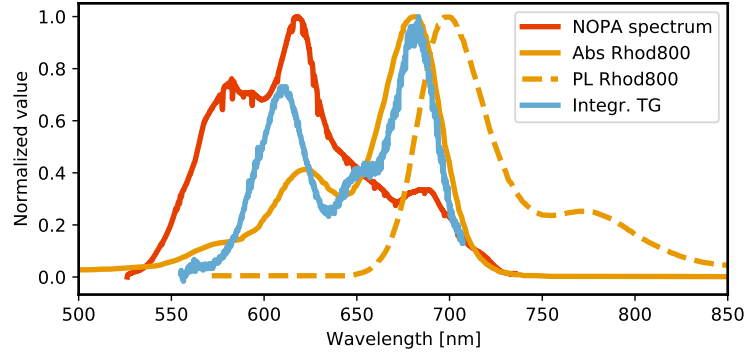


**Figure 5.2** – Red: NOPA spectrum used for the TG experiment. Yellow: Absorbance (solid) and emission (dashed) of Rhodamine 800 (Alessi et al., 2013). Blue: Integrated TG signal  $S_{\text{int}}(\lambda)$ , normalized by the NOPA spectrum (see equation 5.1).

In TG spectroscopy, as in a TG FROG measurement, two pulses, that overlap spectrally and temporally in the sample, generate a spatial refractive index grating, which then diffracts a third pulse. This process is explained in figure 4.14. The only difference to a FROG measurement is, that the spatial refractive index grating is not due to the instantaneous Kerr effect, but due to a resonant induction of a local excited state population in the sample. Thus, in a TG spectroscopy experiment, the effect is not only instantaneous but due to the molecular life time, the spatial refractive index grating can be probed for much longer delays  $t_2$ . By keeping the delay  $t_1$  between the first two pulses fixed to zero and scanning the third one, namely the delay  $t_2$ , a signal  $S(\omega_S, t_2)$  with frequency  $\omega_S$  is emitted.

The spectrum of the NOPA that was used can be seen in red in figure 5.2. The experiment was realized in a box-CARS geometry, as shown in figure 5.1 (A). The delay between A and B is set to  $t_1 = 0$  with the PTS inside the P2B element. Pulse C can then temporally be shifted by scanning  $t_2$  with the DC motor translation stage (figure 4.15). The signal, that is emitted immediately after the third interaction is detected in the home-built spectrometer that is described in figure 3.1. Since the detection scheme is homodyne, the LO is blocked for this measurement.

The signal  $S(\omega_S, t_2)$ , that was normalized with the NOPA spectrum, is shown in figure 5.3. One can clearly see, that the spatial refractive index grating decays within hundreds of picoseconds and that it is not present for  $t_2 < 0$ . Furthermore, the signal fits well to the absorption spectrum of Rhodamine 800 (Alessi et al.,

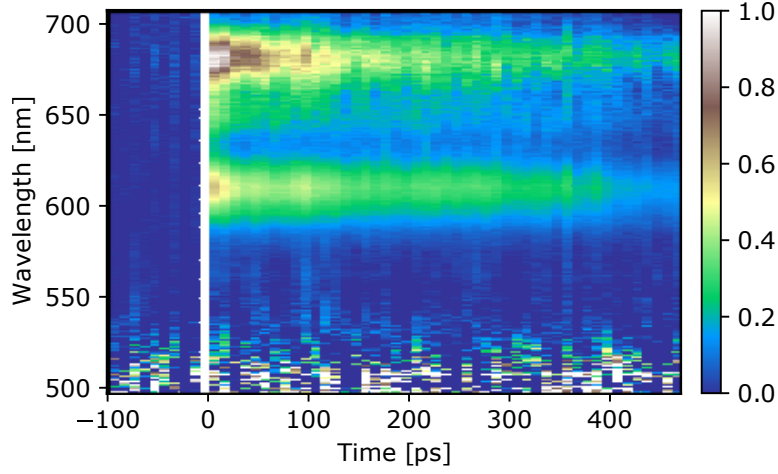


**Figure 5.3** – TG spectroscopy result for Rhodamine 800 in ethanol. Spectral intensity as a function of the time  $t_2$ .

2013). This can be seen by looking at the integrated signal

$$S_{\text{int}}(\omega_S) = \int_0^\infty S(\omega_S, t_2) dt_2, \quad (5.1)$$

that is shown in figure 5.2 in blue, and comparing it with the absorption spectrum (yellow).

To conclude, it can be said that Rhodamine 800 in ethanol is a sample that fits the needs for an FT FWM spectroscopy experiment with this setup and is capable to serve as a model dye to further characterize the setup. Furthermore, the calibration procedure works, since the emitted signal fits the expected absorption spectrum.

## 5.2 Comparison of approaches to scan delays

In order to perform a FT FWM spectroscopy experiment with the SSI approach that was presented in section 2.2.6, the setup is used as described by figure 4.15. All four pulses A, B, C and LO originate from one broad-band NOPA pulse and are compressed by the CMP with 28 reflections, as described in section 4.3 and characterized by figure 4.4. Furthermore, a pair of anti-parallel fused silica glass wedges (figure 2.10) was used for the fine tuning of the chirp.

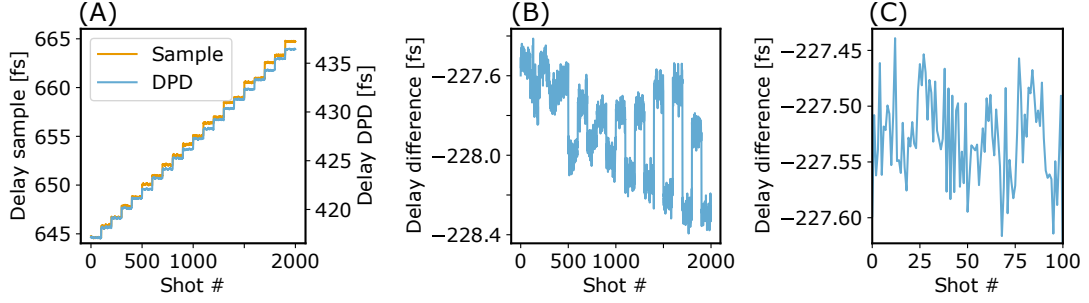


**Figure 5.4** – Delays between the pulses A and B at the sample position and DPD setup. (A) Absolute delays for all shots. (B) Difference between delays from sample position and DPD setup. (C) Magnification of the shots within the first PTS position.

### 5.2.1 Delay scan via translation stage

As a first step, it is essential to evaluate the phase offset between the two DPD setups (figure 3.4) and the sample position. I previously referred to this process as phase calibration. Therefore, the procedure, as it is described in section 3.4, is performed twice. First, the pulse pair (A,B) is sent to the sample position, where a glass slab with a scattering surface is put in place. Both beams are focused into a spot on the scatterer, which then is imaged on the detector inside the home-built spectrometer (figure 3.1). Depending on the delay of the beams A and B, which can be set by the PTS, the measured spectral intensity is an interferogram as described by equation 3.3.

From this interferogram, the differential phase of beams A and B,  $\Delta\varphi_{\text{sam}}$ , can be derived. However, it is still unknown, which pulse arrives first and thus, there is an ambiguity in the sign of the differential phase. As explained by figure 3.7, this can be solved by moving the PTS and thus changing the delay between the two pulses. In order to improve the statistics, the stage is moved in steps of 1 fs over a range of 20 fs and 100 shots are recorded per translation stage position. In total, 2000 single-shot phases  $\Delta\varphi_{\text{sam},i}$  are retrieved.

Simultaneously, the same measurement is performed in one of the two DPD setups, which yields a set of  $\Delta\varphi_{\text{DPD},i}$ . By subtracting  $\Delta\varphi_{\text{sam},i}$ , one can get the phase offset  $\Delta\varphi_{\text{cal},i}$ . After deriving the set of  $\Delta\varphi_{\text{cal},i}$  for the pulses A and B, the same procedure has to be performed for the pulses LO and C.

Figure 5.4 shows the delays  $t_{\text{DPD}}$  and  $t_{\text{sam}}$  that were extracted from the set of differential phases of the pulses A and B. The extraction algorithm that was used

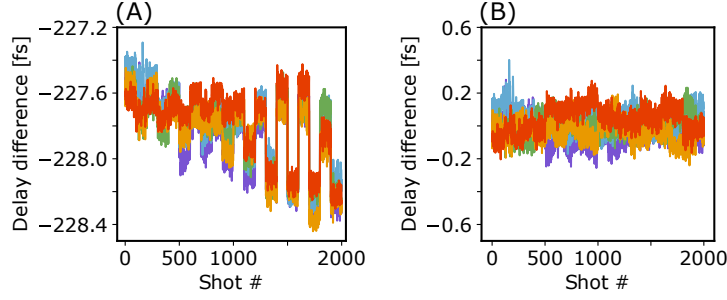


**Figure 5.5** – Repeatability of difference  $\Delta t$  between delays from sample position and DPD setup. (A) Five scans under identical conditions as figure 5.4 (B). (B) Data from (A), but the average was subtracted for each translation stage position, as expressed in equation 5.3.

for this purpose is described in section 3.3. The absolute values of the delays are plotted in panel (A) and in both curves, one can clearly see the step function that is performed with the PTS. However, for some translation stage positions, the step that is measured in the DPD setup does not exactly fit the step size, that is measured in the sample position. This is even clearer, when having a look at figure 5.4 (B), which displays the difference  $\Delta t$  between the two curves in panel (A).

$$\Delta t = t_{\text{DPD}} - t_{\text{sam}} \quad (5.2)$$

The biggest step in  $\Delta t$  can be observed at shot number 1700 with around 600 as. This would reflect into an uncertainty in the single-shot delay of more than  $\lambda/4$  and is thus far away from interferometric precision ( $\lambda/100$ ). However, if looked into a set of shots, in which the PTS was at a constant position, as it is depicted in figure 5.4 (C), one can see that  $\Delta t$  remains constant within an uncertainty that in terms of standard deviation amounts to 38 as.

During this work, many efforts have been made to eliminate the different response of the delays that are measured in the two different positions of the setup to a motion of the PTS. The result of this research indicates, that the translation stage performs a slight yaw when it is moved. Since the single-mode fibers in the DPD setup act as an image point with an aperture of only  $4.1 \mu\text{m}$  (mode field diameter), the calibration on the detector should be unaffected by the yaw. As the pulses from the NOPA exhibit a slight spatial chirp, the spectral coupling efficiency could be influenced. The experimental setup, however, does not have

such an image point after the sample position, which means that a yaw of the PTS directly affects the spectral component of the pulse, that is detected by a certain detector pixel and leads to a temporary miscalibration of the spectrometer.

The hypothesis of the PTS yaw as an origin of the steps in  $\Delta t$  is fortified by the fact that they show a repeatability that can be seen in figure 5.5. Panel (A) shows the same data as figure 5.4 (B), but for five consecutive measurements. It is obvious, how these steps are repeatable and it gets even clearer, when looking at figure 5.5 (B). Here, the corrected delay difference  $\Delta t_{ijk}^{\text{corr}}$  is plotted. It is the difference value of every single shot, subtracted by the average of all shots taken at the corresponding translation stage position.

$$\Delta t_{ijk}^{\text{corr}} = \Delta t_{ijk} - \frac{1}{n_i n_k} \sum_{i,k}^{n_i, n_k} \Delta t_{ijk} \quad (5.3)$$

Here,  $i$  indicates the shot number within one measurement and one translation stage position. In the presented case it spans 0–99. The subscript  $j$  represents the position of the translation stage and spans 0–19. The measurement run is indicated by  $k$ , which runs from 0 to 4. The standard deviation  $\sigma$  is a means to depict the deviation of these numbers from a constant value. In the following,  $\sigma_{\Delta t}^{\text{uncorr}}$  refers to the data in figure 5.5 (A) and  $\sigma_{\Delta t}^{\text{corr}}$  to the corrected data in panel (B).

$$\begin{aligned} \sigma_{\Delta t}^{\text{uncorr}} &= 223 \text{ as} \\ \sigma_{\Delta t}^{\text{corr}} &= 78 \text{ as} \end{aligned} \quad (5.4)$$

A physical explanation for the repeating jumps in  $\Delta t$  is, that the yaw of the translation stage is not random, but induced by irregularities in the guiding. This assumption is confirmed by a scan in which the time ordering of the PTS positions was randomized. It indicates the same dependency of  $\Delta t$  on the stage position.

### 5.2.2 Delay scan via mechanical fluctuations

Using SSI for FT FWM spectroscopy allows a second, innovative approach to vary the delays in the desired range. Instead of moving the PTS to specific, predetermined positions, one can simply increase mechanical oscillations in the system and thereby induce a fluctuation of the delays. Analyzing such data requires a shot-by-shot delay measurement. It can thus not be done with a conventional

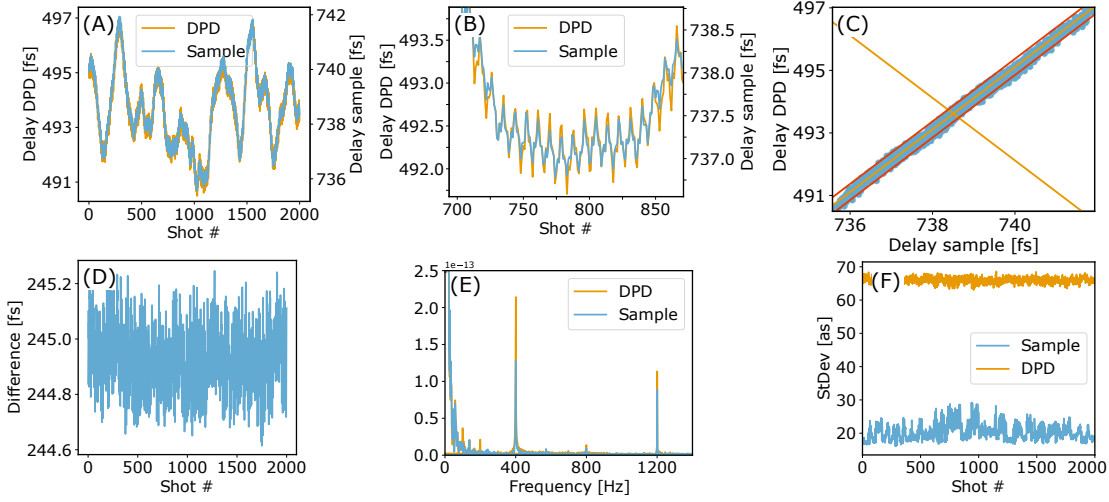


**Figure 5.6** – Delay induced by mechanical fluctuations. A loudspeaker that played a 400 Hz sound was held against the mirror on the PTS. (A) Delay measured for 2000 shots at the sample position and the DPD setup. (B) Magnification of panel (A), to highlight the 400 Hz oscillation. (C) Correlation of the delay at the sample position and the DPD setup. Yellow lines: Diagonals. Red lines:  $\pm 3\sigma$  interval predicted from single-shot uncertainty. Blue dots: Measurement results. (D) Difference of delays  $\Delta t$ . (E) Fourier transforms of the curve in (A). (F) Single-shot uncertainty (standard deviation) that was used to derive the  $\pm 3\sigma$  interval in (C).

method and is a unique feature of the multi-camera SSI approach.

Since I was forbidden to increase the temperature of the lab up to a level that significantly increases noise, this was done by playing a 400 Hz sine wave on a commercial loudspeaker that I held against the end mirror in the modified Michelson interferometer that is mounted on the PTS (figure 3.3).

The delays that are achieved with this approach are shown in figure 5.6. While the 400 Hz sound induces oscillations, that are only resolved in panel (B), fluctuations with a much lower frequency, but larger amplitude appear in panel (A). They exist due to a varying pressure, when holding the loudspeaker against the mirror. Interestingly, these slowly varying fluctuations are perfectly identical in both measurement arms (sample position and DPD setup). The measurements performed in the DPD setup, however, react more sensitive to the 400 Hz sound than the ones in the sample position. To show the correlation of  $t_{\text{DPD}}$  and  $t_{\text{sam}}$ , panel (C) indicates every laser shot with a blue dot in a graph with  $t_{\text{sam}}$  on the horizontal and  $t_{\text{DPD}}$  on the vertical axis. The yellow lines are the diagonals and

the red lines show the  $\pm 3\sigma$  interval that was derived from the single-shot uncertainty (panel (F)) and should contain 99.7 % of all shots. Figure 5.6 (D) displays the difference  $\Delta t$  and is the analogon of figure 5.4 (B) in the PTS approach. These values are distributed with a standard deviation of 113 as. Compared to the 78 as from equation 5.4, it is a bit enhanced, which can be explained with the uncorrected difference in the response of the two measurement arms to the 400 Hz oscillation. The Fourier transform of the oscillations in (A) and (B) can be seen in panel (E). Besides the zero-frequency contribution, it is the 400 Hz oscillation and its overtones that dominate the signal. Panel (F) shows the single-shot uncertainties of the fitting algorithm on the phase that was extracted from the interferograms.

The slowly varying fluctuations are very well tracked by both measurement arms. Here, the accordance of  $t_{\text{DPD}}$  and  $t_{\text{sam}}$  is much better than in the PTS approach or the 400 Hz oscillation. A possible explanation is the following: The pressure with which the loudspeaker was hold against the mirror on the PTS slowly varied throughout the measurement. This stage, however, is mounted on a manual translation stage that absorbed these slow motions better than the piezoelectric one. In contrast to that, the 400 Hz oscillations happen on much shorter time scales and are absorbed by the PTS, whose coil spring has a different stiffness compared to the manual stage.

Apparently, a motion of the manual stage leads to less yaw. Besides a bad quality of the guide rail in the PTS, an explanation for that can be, that the manual stage deals better with the vertical mounting in the setup than the piezoelectric stage. This, in consequence, can lead to an asymmetric friction inside the guide rail of the PTS and the increased yaw angles.

The delays in this measurement only span a range of about 6.5 fs. For an FT FWM spectroscopy experiment, this is not enough, since after a Fourier transform this would result in a frequency resolution of only  $1.7 \cdot 10^{14} \text{ rad s}^{-1}$  or 30 nm if the wavelength is 600 nm. Despite that, this section showed that the presented approach allows to run an FT FWM spectroscopy experiment even without a costly PTS by simply inducing enough mechanical vibrations and measuring them on a single-shot base. As a consequence, one profits from the mechanical noise of the system and – in contrast to conventional FT FWM spectroscopy – a suppression of it is undesired.



### 5.3 Delay uncertainty simulations

In sections 5.2.1 and 5.2.2, it became clear, that there are some uncertainties in the back calculation of the differential phase from the DPD setup to the phase that was measured in the sample position. As explained previously, this is probably due to the different design of both measurement arms and hence slightly different responds to the yaw of the PTS. In order to estimate the effects of an uncertainty in the delays, a simulation was performed prior to the FT FWM experiment.

Therefore, a set of delays  $t_1$  and the corresponding interferograms  $S(t_1, \omega)$  were generated with spectra in the visible range ( $\lambda_0 = 600$  nm, FWHM= 100 nm, figure 5.7 (A)). Starting from these data, the interferograms were shuffled randomly with a specific shuffling amplitude that in terms of standard deviation was  $\sigma_{\Delta t_1} = 200$  as (C), 400 as (E) and 800 as (G). An FFT along the time axis yields the corresponding 2D spectrum in the panels (B), (D), (F) and (H).

Since no molecular behaviors, like e.g. couplings of different states, are considered in this study, the signal in the undisturbed case (B) is exclusively on the diagonal. However, the spectrograms  $S(t_1, \omega_S)$  lose their diagonal structure, the less precise the delay of the pulses is known. In the 2D spectra  $S(\omega_{12}, \omega_S)$  in the right columns of figure 5.7, this reflects in a noise that stretches along the full excitation frequency axis and becomes dominant for  $\sigma_{\Delta t_1} > 400$  as. Besides the noise, there is also a decrease of the signal on the diagonal observable with increasing  $\sigma_{\Delta t_1}$ . The vertical lines in the 2D spectra, that can mostly be seen in panels (B) and (C) are artifacts due to a limited range of the delay  $t_1$ .

This simulation indicates, that it is feasible to run a successful FT FWM experiment with both delay scanning techniques, that were presented in section 5.2, since in either case, the precision is approximately 100 as.

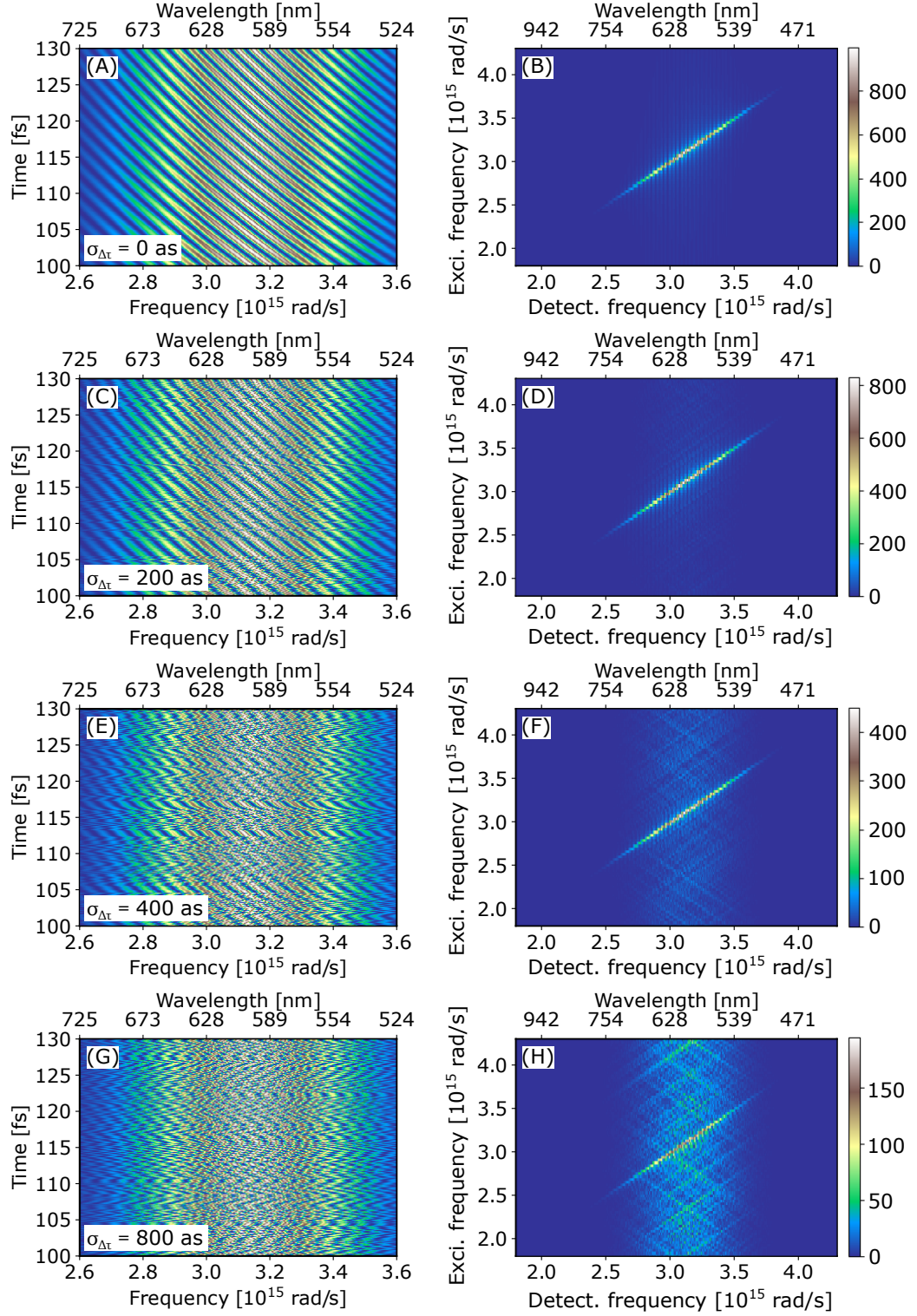


**Figure 5.7** – Simulated 2D spectra in the presence of delay uncertainty. Left column:  $S(\omega_S, t_1)$  before Fourier transform. Right column: 2D spectrum  $S(\omega_S, \omega_{12})$  after Fourier transform along  $t$ . Row 1: No uncertainty. Row 2: Uncertainty  $\sigma_{\Delta t} = 200$  as. Row 3:  $\sigma_{\Delta t} = 400$  as. Row 4:  $\sigma_{\Delta t} = 800$  as.

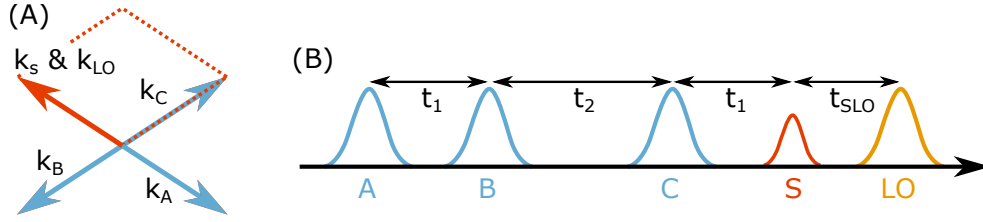


**Figure 5.8** – FT FWM spectroscopy experiment. (A) Phase matching in the box-CARS geometry. Blue: Projections of  $k$ -vectors of beams A, B and C on the plane that is perpendicular to the direction of propagation. Red: TG signal  $\vec{k}_S = -\vec{k}_A + \vec{k}_B + \vec{k}_C$  and the LO. (B) Pulse sequence in a rephasing experiment.

## 5.4 FT FWM spectroscopy

In this section I present the results of the first FT FWM spectroscopy experiment, that was realized with the approach of this work and – to show the potential of SSI in this context – I compare different analysis methods.

Figure 5.8 shows the phase matching condition and the pulse sequence for a rephasing FT FWM spectroscopy experiment. Here, delaying the LO to a point in time behind the signal is reached by inserting a glass slab of thickness 1 mm between the focusing mirror and the sample into the LO beam. First of all, this shifts the LO temporally behind the signal emission, such that it cannot effect the sample before the signal emission. Second, if the slab is slightly tilted, a spatial shift is induced, such that the focus point of the LO and the other beams do not overlap. This avoids any effect of the first three pulses on the LO and thus prevents a possible modification of the LO field due to varying experimental parameters like e.g. delays of A, B or C. And finally, by using a glass slab with a reduced optical transmission, it is possible to decrease the intensity of the LO down to the level of the signal. Like that, a saturation of the detector can be avoided and optimal conditions for heterodyne detection are given.

### 5.4.1 Experimental parameters

For this experiment, the setup was configured as for the homodyne TG spectroscopy experiment (section 5.1) and the corresponding NOPA spectrum can be seen in figure 5.2 (red). This was achieved with the setup that is described in figure 4.15. Since heterodyne detection is obligatory in FT FWM spectroscopy, in contrast to the TG spectroscopy experiment, the LO was not blocked. As in

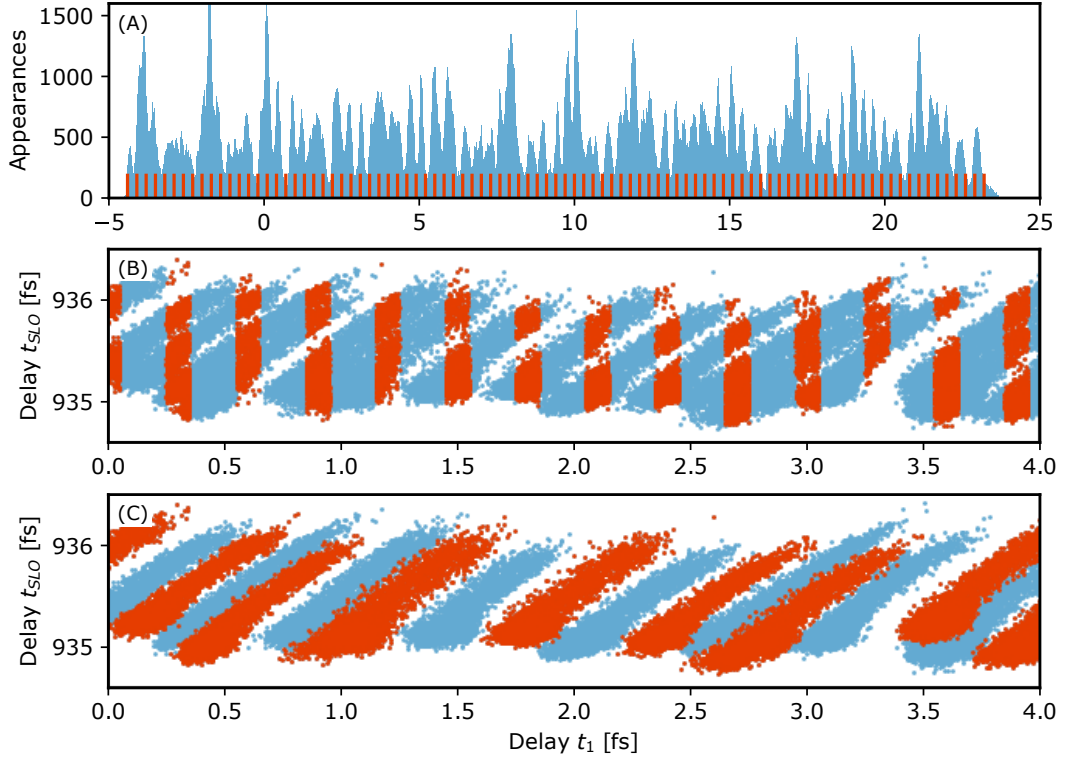


**Figure 5.9** – Delays in the FT FWM spectroscopy experiment. (A) Blue: Histogram of delays  $t_1$  (resolution: 20 as) in FT FWM spectroscopy experiment. Red: Centers of bins. (B) Depiction of analysis method 1. Section of the correlation plot between delays  $t_1$  and  $t_{SLO}$ . Blue: Unselected shots measured during the experiment. Red: Shots selected with binning. Bins are equally spaced by 300 as and have a width of  $\pm 50$  as. (C) Depiction of method 5. Red and blue: Shots that belong to different PTS positions.

chapter 4.5, the compression of the pulses was realized with 28 bounces on a CMP and a pair of fused silica wedges for the fine tuning.

Furthermore, the method of setting delays with the PTS, as it is presented in section 5.2.1, was chosen, since it is more reliable in terms of the resulting distribution of delays and the simulation from section 5.3 justifies the assumption, that it should be possible to do an FT FWM spectroscopy experiment with a precision of  $\sigma_{\Delta t} = 78$  as (equation 5.4).

To show the full set of novel capabilities, the approach can provide with respect to conventional experiments, I decided to target a continuous distribution of  $t_1$ , which was achieved by moving the PTS in small steps of 300 as. Like that the delay distributions for single stage positions overlap and a statistical distribution

**Table 5.1** – Experimental parameters of the FT FWM spectroscopy experiment.

Parameter	Value
PTS range	−5 to 25 fs
PTS spacing	300 as
Shots per PTS position	8000
DC stage position	50 fs

of points covering all the spanned range can be acquired. Finally, it is possible to select those shots, that fit the requirements best, in the analysis. Table 5.1 shows the chosen experimental parameters.

### 5.4.2 Phase calibration, binning and shot selection

Since the calibration phase  $\varphi_{\text{cal}}$  (equation 3.8) depends on the position of the PTS, the phase calibration measurement has to be done at every position of the stage, that later will be approached during the experiment. To make a realistic estimation of the calibration phase at every stage position and review the repeatability, the calibration procedure was run five times and average values were taken for calibration. Like that, for every position of the PTS, a  $\varphi_{\text{cal}}$  can be derived for both pulse pairs, (A,B) and (LO,C). With this, the respective differential phase in the sample position can be calculated according to equation 3.8.

The distribution of delays  $t_1$  between the pulses A and B, that was achieved with the experimental parameters presented in table 5.1 and measured in the DPD setup, can be seen in figure 5.9 (A), where the blue data show a histogram of  $t_1$ .

As explained in section 2.2.2, for a FWM experiment in the time domain, it is the goal to get the amplitude and phase of the third order signal  $S(t_1, \omega_s)$ . In order to perform an FFT along  $t_1$ , the delays have to be equidistant. In this work, no special care was taken to stabilize  $t_1$ , however, I am able to select the right shots after the measurement in the analysis. This can e.g. be done by applying a binning procedure with respect to  $t_1$  and considering all shots within a certain bin to have an identical  $t_1$ . By selecting equally spaced binning centers an FFT will be possible.

The result of a binning procedure with 300 as  $t_1$ -bin spacing and  $\pm 50$  as bin size can be seen in figure 5.9 (B). The horizontal axis is  $t_1$  and the vertical axis is the delay  $t_{\text{SLO}}$  between the emission of the rephasing signal and the LO. Every

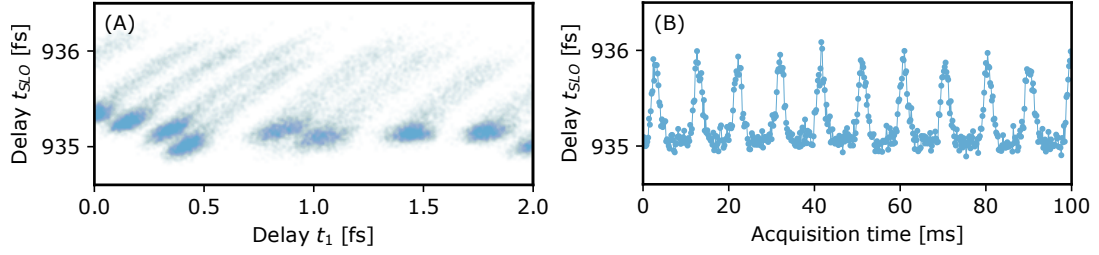


**Figure 5.10** – (A) Correlation plot, as in figure 5.9. Transparent color indicates strongly reduced shot density within the tails of each PTS position (at larger  $t_{\text{SLO}}$ ). (B)  $t_{\text{SLO}}$  over acquisition time, while PTS did not move.

point refers to one shot in the experiment. The red points indicate shots with a  $t_1$  inside a bin, whereas the blue shots are outside. The delay  $t_{\text{SLO}}$  is derived by

$$t_{\text{SLO}} = t_{\text{CLO}} - t_1, \quad (5.5)$$

where  $t_{\text{CLO}}$  is the delay between the pulses C and LO (figure 5.8 (B)) and can be calculated with the result from the DPD and the phase calibration. The binning centers can also be seen in figure 5.9 (A), where they are marked as red lines.

The shot-by-shot calculation of the delay  $t_{\text{SLO}}$  is a peculiarity of this approach. It allows a direct calculation of the absolute phase of the signal and thus a determination of its real and imaginary part without an ambiguity, which is a common issue for most of the conventional techniques (Jonas, 2003).

It is noteworthy, that the actual distribution of the shots along  $t_{\text{SLO}}$  is much narrower than figure 5.9 (B) suggests. To show that, figure 5.10 (A) shows the same plot, but without the bins and in transparent color. Like that the density of shots is getting clear and it can be seen that the large values of  $t_{\text{SLO}}$  belong to tails with only very few shots. By plotting  $t_{\text{SLO}}$  with respect to the acquisition time (panel (B)), a 100 Hz oscillation appears. After an extensive research, I could ascribe the origin of this oscillation to the current of the pump laser of the chirped pulse amplification (PU in figure 4.15). The fluctuating current leads to an increased intensity, which – via a series of nonlinear effects in optical media – has an influence on the delay of the pulses. Regardless, multi-camera SSI allows to either correct for this behavior or only select shots that are not affected. In any case, an elaborate suppression of the problem is not necessary with this approach.

After the binning procedure, there are different ways to proceed and some of them



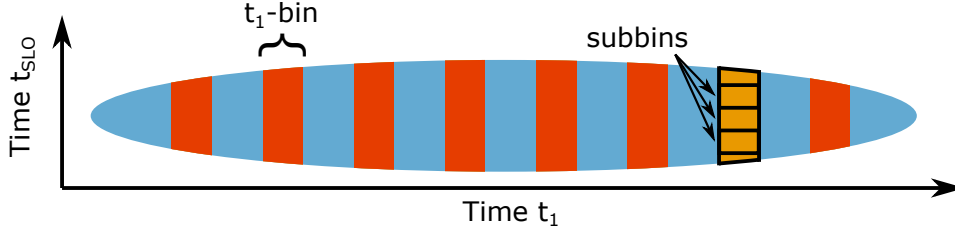


**Figure 5.11** – Schematic of correlation plot for the binning procedure. Blue: Unselected shots. Red: Equally spaced  $t_1$ -bins to enable FFT along  $t_1$ . Yellow: Subbins inside one  $t_1$ -bin, as used in method 3.

are presented in the following.

**Method 1: Averaging interferograms** Averaging all interferograms inside a  $t_1$ -bin leads to a correct result, given that the spacing of the bins is small enough. However, due to mechanical fluctuations, the delay  $t_{\text{SLO}}$  is not constant for all shots inside one  $t_1$ -bin, but every shot  $i$  shows a deviation  $\Delta t_{\text{SLO},i}$  from the average  $\bar{t}_{\text{SLO}}$ . This reflects in the vertical spread of the red bins in figure 5.9 (B).

$$t_{\text{SLO},i} = \bar{t}_{\text{SLO}} + \Delta t_{\text{SLO},i} \quad (5.6)$$

The larger the single-shot fluctuations are, the worse will be the contrast of the averaged interferogram, which in return reduces the signal amplitude.

**Method 2: Averaging corrected interferograms** In contrast to method 1, method 2 does not average the interferograms in the pixel space, but first runs the phase extraction procedure that was described in section 3.3 for every shot to get a set of complex interferograms  $S(t_1, \omega_S)$  (figure 3.5 (C)). At this point, one can correct every single shot for a phase of  $\omega \Delta t_{\text{SLO},i}$  and average the complex interferograms afterwards. This analysis method compensates the drawback of reduced signal amplitude due to mechanical fluctuations in the experiment and takes full advantage of the single-shot multi-camera approach.

**Method 3: Averaging subbins** In the case of a weak SNR of the measured data, applying the phase extraction algorithm on single-shot interferograms can be challenging. In such cases, it can be useful to apply an intermediate method for the analysis. Sectioning the shots into subbins according to  $t_{\text{SLO}}$  inside each  $t_1$ -bin (figure 5.11) and averaging all interferograms inside one subbin preserves

the contrast and thus the signal amplitude, if the subbins are small enough. At the same time, the SNR is increased, which is beneficial for the phase extraction algorithm. After subtracting a phase of  $\omega\Delta t_{\text{SLO}}$  from the complex interferogram of each subbin, as it was also done in method 2, all subbin results inside one  $t_1$ -bin can be averaged. This average has to be weighted, to take the varying number of shots per subbin into account.

**Method 4: Interpolation** There are also methods that do not imply binning and averaging, that are conceivable. It is, e.g. an option to extract the amplitude and phase of every single shot and afterwards interpolate the complex spectra along  $t_1$ . Like that, equidistant delays  $t_1$  can be achieved. However, truncation errors and thus additional noise has to be expected due to the interpolation.

**Method 5: Conventional Analysis** In a conventional analysis, where the user has no knowledge on the single-shot delays, all interferograms within one PTS position are averaged in the pixel space. The different PTS positions are marked with different colors in figure 5.10 (C). This approach differs from method 1, as it can be seen by comparing them with the shots inside the  $t_1$ -bins from panel (B). The simulation results in section 5.3 showed that ultimately, this uncertainty in  $t_1$  will cause a degradation of the signal strength.

Of course these analysis methods can also be applied, if the steps of the PTS are bigger and the distribution of delays  $t_1$  is not continuous. In this case, however, one limits the selection of  $t_1$ -bins to the steps that were made with the translation stage.

### 5.4.3 Presentation and discussion of results

The methods presented above yield one complex interferogram  $S(t_1, \omega_s)$  per  $t_1$ -bin, which either before or after averaging is obtained from the phase and amplitude extraction algorithm. Exemplary, in figure 5.12 (A), the real part of such a set of interferograms, that was analyzed with method 2 is shown. For these data the  $t_1$ -bin size and the bin spacing are chosen to  $\pm 50$  as and 300 as, respectively. For the purpose of normalization, according to equation 2.65,  $S(t_1, \omega_s)$  is divided by  $|E_{\text{LO}}|$ . The oscillatory pattern along the frequency axis corresponds to the third term in equation 2.65 and thus depicts the differential phase between the signal and the LO. Increasing  $t_1$  by  $\Delta t_1$  with a translation (or oscillation) of the PTS shifts beam B and the LO (figure 4.18). However, in a rephasing experiment, the



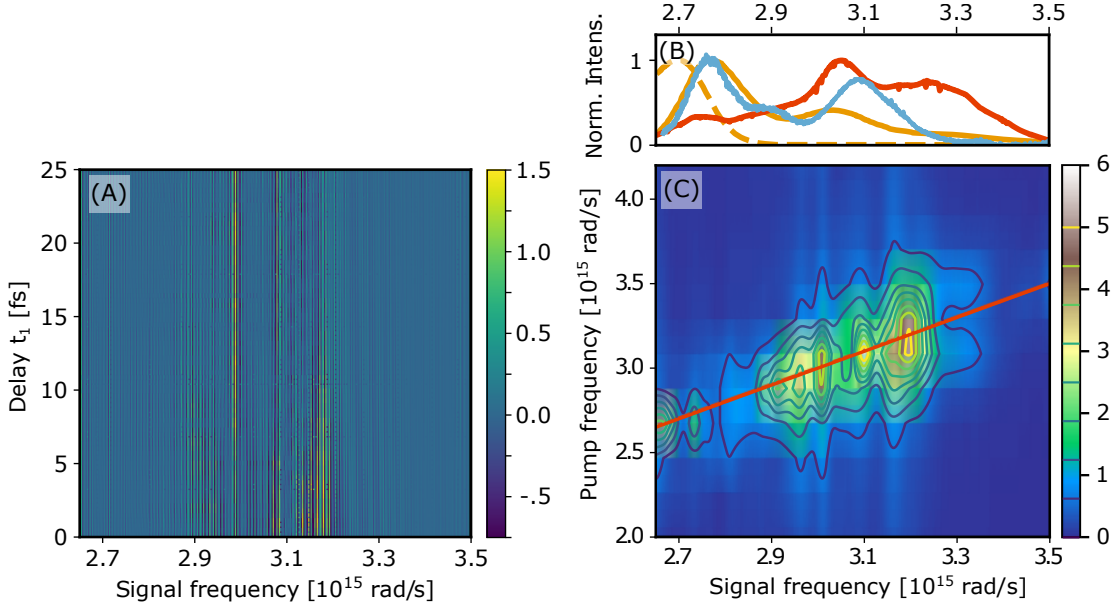


**Figure 5.12** – Rephasing FT FWM spectroscopy results on Rhodamine 800 analyzed with method 2. (A) Real value of  $S(t_1, \omega_S)$ . (B) TG signal (blue), NOPA spectrum (red), absorption and emission of Rhodamine 800 (yellow) as in figure 5.2. (C) Absolute value of  $S(\omega_{12}, \omega_S)$ . Red line: Diagonal of 2D spectrum.

emission of the signal with respect to the third pulse is delayed by  $t_1$  and thus also the signal experiences the shift  $\Delta t_1$ . For that reason,  $t_{SLO}$  remains constant for any position of the PTS. This reflects in the dominant vertical pattern throughout the whole spectrogram, as well as in the horizontal shape of the correlation plots in figures 5.9 (B), 5.9 (C) and 5.10 (A).

At this point, to each of the complex interferograms, the linear phase  $\omega t_1$  is added. This is done to refer the phase of the signal to the third pulse. Afterwards, an FFT along  $t_1$  is applied to get the 2D spectrum  $S(\omega_{12}, \omega_S)$ . The absolute values of the 2D spectrum are displayed in figures 5.12 (C).

The diagram in panel (B) above the 2D spectrum shows the NOPA spectrum (red), the spectrum of the TG experiment (blue) and the emission and absorption spectra of Rhodamine 800 (yellow). The data are identical to figure 5.2.

It can be said that the 2D spectrum shows a clear signal that is centered on the diagonal. It has three main peaks at the frequencies 3.2 rad/fs, 3.1 rad/fs and 3.0 rad/fs. By comparing it with the TG signal in panel (B), one can see that the peak with the highest frequency in the 2D spectrum matches a shoulder in the

TG spectrum and the intermediate 2D peak corresponds to the high-frequency peak of the TG signal. The low-frequency peaks of the TG experiment are a bit underrepresented in the 2D spectrum, however, there clearly is a shoulder in the 2D spectrum at 2.9 rad/fs and a small signal at 2.75 rad/fs, which both can be found in the TG result. The signal at 2.65 rad/fs in the 2D spectrum might correspond to the main peak in the emission spectrum of Rhodamine 800. However, it can also be an artifact due to the normalization with the very weak LO field amplitude in this range.

The relative underrepresentation of the signal in lower frequencies of the 2D spectrum can already be observed in the spectrogram in figure 5.12 (A), where the complex interferograms show a much smaller amplitude below 2.9 rad/fs for all delays  $t_1$ . A possible explanation for that is the strong absorption of Rhodamine 800 in that spectral range. The signal in the spectral regions above 3.3 rad/fs, however, is expected to be as small, since Rhodamine 800 shows neither absorption, nor emission in this frequency range.

By having a closer look at the shape of the signal in the 2D spectrum, it is clear, that it is much more distributed along the pump frequency axis than the signal frequency axis. This effect mostly appears at signal frequencies with strong signals and refers to the noise that is induced by an uncertainty in the derivation of the single-shot delays  $t_1$ . It is also observed in the simulation in figure 5.7. Improving the precision of the delay extraction could in consequence lead to a reduction of that noise.

In order to compare different analysis methods and parameters, figure 5.13 shows four different 2D spectra that all originate from the same experimental data. Table ?? lists the analysis settings that were used in either case. Note that the 2D spectrum in panel (C) is identical to the one that was previously shown in figure 5.12.

For all methods, the  $t_1$ -bin spacing was 300 as. In panel (A) the  $t_1$ -bin size is equal to the spacing and all shots of the experiment are used. Since I applied method 1, there was no correction of the phase according to the delay  $t_{\text{SLO}}$  to improve the signal amplitude after averaging. Still, it can be expected that this approach leads to better results than a conventional analysis of a FT FWM spectroscopy experiment, in which all shots from one PTS position are selected for one bin. This can be seen by comparing figures 5.9 (B) and (C), where shots from one PTS positions clearly span over several  $t_1$ -bins. However, in fact, the result from

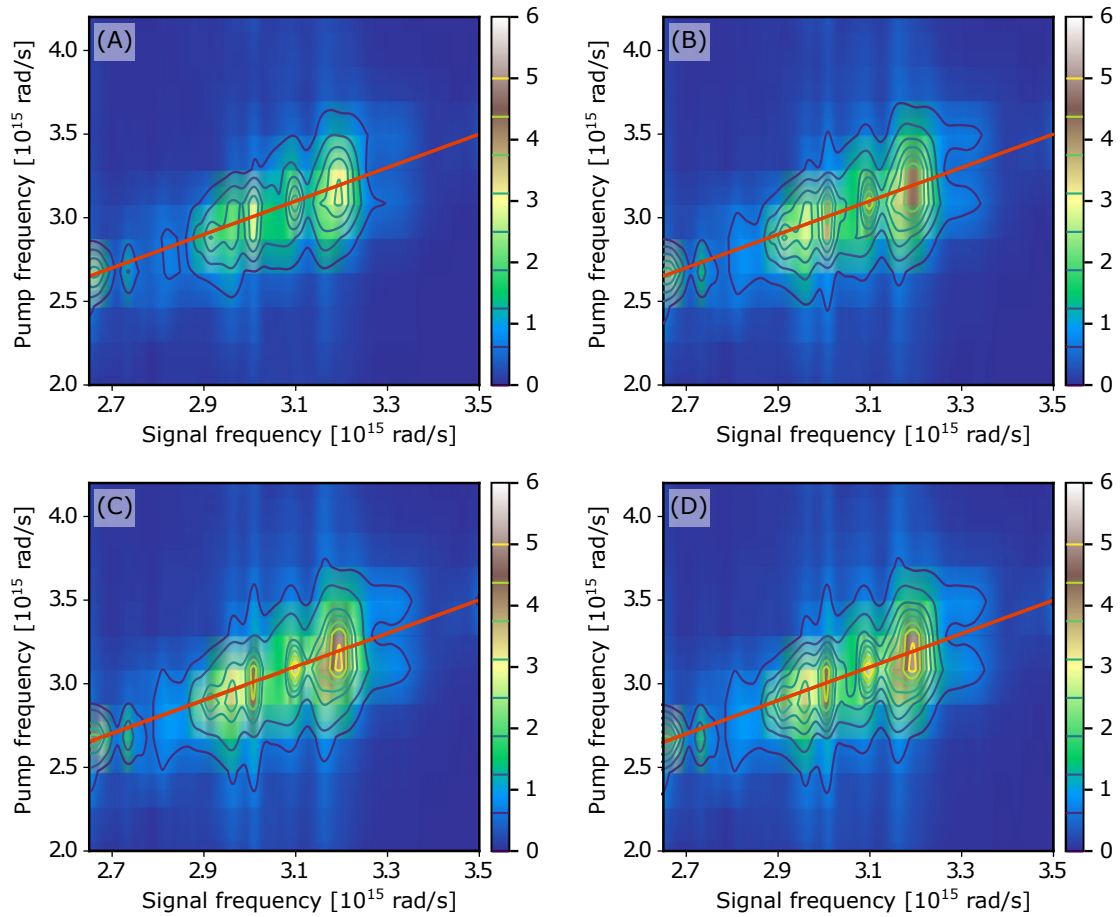


**Figure 5.13** – Comparison of 2D spectra from the same FT FWM spectroscopy experiment, analyzed with different methods. Methods and parameters of each panel are shown in table ?? . Color code and contour levels are identical to allow comparison.

a conventional analysis is very similar to method 1. This can be explained with the small number of shots that are located in the tails of figure 5.10 (A). Since there are so few outliers, they barely contribute to the experiment and do not remarkably disturb the result. This shows that the intrinsic phase stability of the setup that I used is already good enough. In the case of noisier experimental conditions or shorter wavelengths, a better improvement due to the application of method 1 with respect to a conventional analysis can be expected.

In the second analysis setting, I decreased the  $t_1$ -bin size, but still kept the analysis method identical. For panel (C) and (D), I took full advantage of the multi-camera SSI approach and selected only shots that were close enough to one of the  $t_1$ -binning centers, as well as corrected every shot by the fluctuations before averaging (method 2).

The color code and contour lines in figure 5.13 are identical throughout all panels and can be used for comparison. In doing so, it can be seen, that decreasing the  $t_1$ -bin size from  $\pm 150$  as to  $\pm 50$  as ((A) to (B)) improves the signal amplitude by more than 20%. By switching from method 1 to method 2 and keeping the  $t_1$ -bin size fixed, the amplitude of the data again increases by approximately 20%. No improvement was achieved from panel (C) to (D), where the  $t_1$ -bin size was reduced down to  $\pm 20$  as. This can be interpreted with the two counteracting processes, a reduction of the  $t_1$ -bin size has. Firstly, the signal can be expected to increase, because the error in  $t_1$  due to the binning is minimized. On the other hand, a reduction of the bin size leads to less shots that are considered for the analysis and thus to a smaller SNR. Besides that, due to the steps that appear in the calibration procedure of the DPD setup, the single-shot delay precision is approximately 80 as (equation 5.4). Decreasing the bin size to values smaller than the precision is not meaningful and can explain, why there is no improvement by a further reduction of the  $t_1$ -bin size.

#### 5.4.4 Independent control of the population time

This experiment was done to prove the ability of executing a FT FWM spectroscopy with this new approach that does not require any means of phase stabilization. The interpretation of the data and the conclusion on molecular properties of Rhodamine 800, however, is difficult. The reason for that is, that, as can be seen in figure 4.18, a translation of the PTS shifts pulse B, which ultimately leads to the desired increase of  $t_1$ . However, at the same time,  $t_2$ , which is sometimes

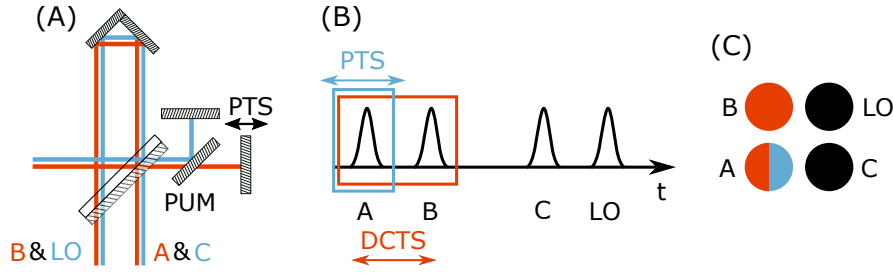


**Figure 5.14** – Independent control of the population time  $t_2$  in rephasing experiments. (A) New design of the Michelson interferometer. Pulses A and C are transmitted by the beam splitter. PUM: Pick-up mirror to redirect pulse C. (B) Pulse sequence as shown in figure 4.18. Only pulse A is shifted by PTS. (C) Geometrical arrangement of pulses. Blue: Pulse delayed by PTS. Red: Pulse delayed by DC motor translation stage. Black: Pulse not delayed.

referred to as the population time  $T$  and in a rephasing experiment is the delay between the pulses B and C, decreases, since pulse C is fixed in time. In consequence, the experimental data presented above were collected with an unconstant population time  $t_2 = 50$  fs for  $t_1 = 0$  and  $t_2 = 25$  fs for  $t_1 = 25$  fs. During this work, two possible workarounds were developed to solve this issue and they are discussed in the following.

In the first option, the beams are rearranged, such that pulses A and C instead of B and LO are now transmitted by the beam splitter inside the Michelson interferometer. The new arrangement is just a mirror image of the one previously used and thus still satisfies the phase matching condition. As can be seen in figure 5.14 (A), pulse C then has to be redirected by a pick-up mirror such that it is not influenced by the PTS. This leads to the pulse sequence in panel (B), where an increase of  $t_1$  solely shifts pulse A and  $t_2$  remains unchanged. In the case of a non-rephasing experiment, pulse B arrives at the sample before pulse A and  $t_2 = t_{AC}$ . Now the pick-up mirror has to be removed to shift A and C simultaneously and keep  $t_2$  constant.

As a further option, one could keep the beam arrangement, but install a second piezoelectric translation stage on top of the DC motor translation stage and run it synchronized, but with opposite direction to the PTS inside the P2B element. Like that, the variation of  $t_2$  that is induced by a translation of the PTS is compensated.

## 5.5 Conclusion

In the beginning of this chapter, I presented results of a homodyne TG spectroscopy experiment with Rhodamine 800 in the visible regime to prove its capability to be used as a model dye for the FT FWM experiment. The results agree with the expectations that can be made from previous studies on this dye in terms of spectral shape and dynamics (Alessi et al., 2013; Abugo et al., 2000).

Afterwards, two different methods to vary the delay  $t_1$  in a FT FWM experiment were tested and compared. Using the PTS leads to slightly different delays in the DPD setups and the sample position, which can be problematic for the calibration of the DPD setup. However, a repeatability was found in this mismatch, with which the problem can be compensated to a large amount. A better agreement between DPD setup and sample position was achieved by adding slow mechanical vibrations to one end mirror of the Michelson interferometer.

I presented simulation results on the effect of an uncertainty on the delay  $t_1$ . They indicate, that the achieved precision of the PTS method is sufficient to successfully run a FT FWM experiment.

The chapter continues with the results of the FT FWM experiment that are analyzed with different methods and analysis parameters. The comparison of the results reveals that there is a total improvement in the signal strength of the 2D spectrum by a factor 1.5 with respect to a conventional measurement in a phase-stable setup. Greater benefits of the presented methods can be expected for noisier systems. Besides that, it is conceivable, that for a further refinement of the method, a better precision in the extraction of the delay and consequently the differential phase is necessary. Like that, choosing smaller  $t_1$ -bins can improve the signal quality and also the correction according to  $t_{\text{SLO}}$  in method 2 works better. Ways to accomplish that requirement are discussed in section 6.2.

## Concluding Remarks

### 6.1 Summary

Within this thesis, a new concept for tackling the issue of phase stabilization in the context of Fourier transform (FT) four-wave mixing (FWM) spectroscopy was presented. Unlike other experimental techniques, this approach is not based on the suppression or compensation of mechanical fluctuations, but on a reduction of the effective integration time, by implementing a single-shot detection scheme. In combination with femtosecond laser pulses, the phase stability can be improved by many orders of magnitude. The experimental proof of principle was given through an interferometric experiment in the presence of strong mechanical noise and air turbulences. While the application of a conventional detection scheme led to an almost complete loss of the phase information, consistent results were achieved with single-shot interferometry (SSI).

Subsequently, I introduced the pump-probe-to-box-CARS (P2B) setup, which is the central experimental element of this work. With its modified Michelson interferometer, it converts any pump-probe scheme into a box-CARS geometry by creating duplicates of the two incoming beams, whose delays can be defined with a piezoelectric translation stage (PTS). Besides that, the P2B element superimposes fractions of the relevant pulse pairs for a single-shot interferometric measurement of their differential phase.

A delay extraction algorithm, that was developed as a part of this work, allows to determine all relevant delays for a FT FWM spectroscopy experiment with a precision of down to few attoseconds from the differential phase data. It thereby benefits from the fact, that all phase parameters with order larger than two can be assumed to be constant for all shots and only the second order, namely the delay of the pulses, fluctuates due to mechanical oscillations in the setup.

These two achievements, the single-shot multi-camera phase detection scheme, together with the attosecond delay extraction algorithm, together allow to renounce to build an elaborate delay control mechanism, which typically is necessary in FT FWM spectroscopy experiments. Instead, the distribution of delays is noise-driven and the shots that show appropriate delays for the respective experiment can be selected during the analysis. Indeed, later in the thesis, I presented two different approaches of delay variation. One of them is based on the motion of a PTS together with the intrinsic noise of the setup and the other was driven by externally induced mechanical fluctuations of the translation stage.

The subsequent chapter was devoted to pulse shaping and particularly to methods of pulse compression and phase retrieval. I compressed ultra-broad pulses with a combination of a chirped mirror pair and fused silica wedges with a small internal angle down to 8 fs FWHM. These results were measured with transient grating (TG) FROG. Furthermore, I introduced an iterative approach for pulse compression with means of adaptive shaping. Within this work, a liquid crystal spatial light modulator (LC SLM) was used for this experiment, however any kind of programmable phase-mask is appropriate. Since the phase retrieval for this experiment was achieved with a cross-phase modulation (XPM), an algorithm to extract the group delay from an XPM trace in a reliable way was introduced. Besides these experimental outcomes, ray tracing simulations showed that the implementation of an adaptive shaping scheme with a prism as a dispersive element can lead to a promising improvement of the throughput for broad pulses, compared to a grating setup. However, the additional material leads to a chirp that has to be minimized and pre-compressed.

To bring all the previously mentioned achievements together, in the last chapter, I show FT FWM spectroscopy results in Rhodamine 800. Therefore, experimental data were collected in the described single-shot multi-camera approach without applying special means of phase stabilization or attosecond delay control. The results were analyzed with two different methods, both profiting from multi-camera SSI at different extents. Method 1 selects only those shots that have an appropriate delay  $t_1$ , whereas method 2 does the same and besides that corrects the interferograms by the single-shot delay between the signal and the local oscillator. Both methods are unique to SSI and lead to a significant improvement of the signal strength.



## 6.2 Prospect

A further performance enhancement can be expected, if the calibration of the phase offset can be improved. While for a stationary PTS, the calibration works already excellent, difficulties appeared when the PTS was moved. I ascribe this to different yaw angles of the translation stage before and after the motion, which leads to a change of the detector calibration at the sample position, but, due to the single mode fibers, not in the differential phase determination (DPD) setups. One option to solve this problem was already presented in section 5.2: Manually inducing a varying pressure on the end mirror of the Michelson interferometer, that is mounted on the PTS and a manual translation stage leads to identical results in the sample position and the DPD setup. Applying this technique for a wider range of delays than before can indeed be a successful method for a FT FWM spectroscopy experiment.

This solution could give better results, due to a better correction of the single-shot delays, however, it is not a response to the fact that the two measurement arms react differently on angular fluctuations of one of the beams. To solve that, the implementation of a confocal detection scheme with a pinhole after the sample position seems to be mandatory. In doing so, the detector plane would be an image point of the pinhole and angular fluctuations will not effect the detector calibration anymore. The analogon of the pinhole in the DPD setup is the single-mode fiber.

Given the case that the confocal scheme – against my prediction – does not satisfy the expectations, it is an option to design both detection arms completely symmetric. In that case, the superimposition of the two pulses also in the DPD setups has to be achieved with a scattering surface, which both beams are focused on.

A modification which, firstly, reduces the amount of material transmission, secondly, can help to use the P2B element in other spectral regimes and finally, increases the throughput of the setup, is the substitution of the beam splitter and the chirp compensation plate inside the Michelson interferometer by a knife-edge prism mirror, as it is sketched in figure 6.1. The benefits of this modification are an easier pulse compression and less higher-order phase contributions, as well

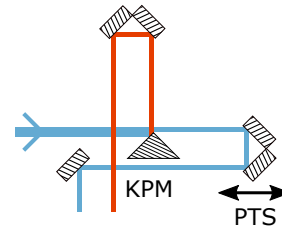


**Figure 6.1** – Alternative approach for the modified Michelson interferometer. KPM: Knife-edge prism mirror. PTS: Piezo translation stage.

as a potentially better availability of knife-edge prism mirrors compared to thin-substrate, broadband beam splitters in some spectral regimes. Furthermore, there will be an increase of the intensity by factor of two. This is due to the back-reflected light of a normal Michelson interferometer with a beam splitter, which is lost for the experiment. Implementing this approach necessitates a good quality of the beam mode, since a lateral chirp of the pulses can then lead to different spectra of the pulse duplicates.

This work simplifies and solves most of the problems, conventional approaches to FT FWM spectroscopy deal with (section 2.2) in a simple, elegant and yet cost-efficient way. Thus, it can make FT FWM spectroscopy a more routine experiment in any ultrafast laboratory. The fact that the presented approach only uses conventional and reflective optics brings to two major advantages: Firstly, the huge spectral flexibility allows the application in other spectral ranges, that currently are only rarely explored (Achazi and Cannizzo, 2017) and/or the implementation of new, broadband light sources (Klimczak et al., 2017), that can potentially boost the field of FT FWM spectroscopy.

And secondly, the presented scheme can be built in a very compact way. That allows the integration of this technique into other setups. For example, it is one idea to use it in combination with a terahertz experiment and run FT FWM spectroscopy measurements in the visible spectrum under strong quasi-static electric fields from ultrafast terahertz pulses. Such an experiment can help to investigate and understand polar properties and intramolecular electrostatics that play key roles in the charge transfer processes during photosynthetic reactions and in artificial light harvesting technologies.

# Appendix

---

## Problem A

$$\rho^{(1)}(t) = \int_{t_0}^t d\tau_1 E(\tau_1) e^{-\frac{i}{\hbar} H_0(t-t_0)} [\mu_I(\tau_1), \rho(t_0)] e^{+\frac{i}{\hbar} H_0(t-t_0)}$$

$$P^{(1)}(t) = \langle \mu(t) \rho^{(1)}(t) \rangle, \quad \alpha := \frac{i}{\hbar} H_0(t - t_0)$$

Plugging the equations for the first-order density matrix and the polarization together and for simplicity, substituting the exponent of the time evolution operator with  $\alpha$  leads to

$$\begin{aligned} P^{(1)}(t) &= \langle \mu(t) \int_{t_0}^t d\tau_1 E(\tau_1) e^{-\alpha} [\mu_I(\tau_1), \rho(t_0)] e^{+\alpha} \rangle \\ &= \int_{t_0}^t d\tau_1 E(\tau_1) \langle \mu(t) e^{-\alpha} [\mu_I(\tau_1), \rho(t_0)] e^{+\alpha} \rangle \\ &= \int_{t_0}^t d\tau_1 E(\tau_1) \langle \mu(t) e^{-\alpha} [e^{+\alpha} \mu(\tau_1) e^{-\alpha}, \rho(t_0)] e^{+\alpha} \rangle \\ &= \int_{t_0}^t d\tau_1 E(\tau_1) (\langle \mu(t) \cancel{e^{-\alpha}} e^{+\alpha} [\mu(\tau_1) e^{-\alpha}, \rho(t_0)] e^{+\alpha} \rangle \\ &\quad + \langle \mu(t) e^{-\alpha} [e^{+\alpha}, \rho(t_0)] \mu(\tau_1) \cancel{e^{-\alpha}} e^{+\alpha} \rangle) \\ &= \int_{t_0}^t d\tau_1 E(\tau_1) (\langle \mu(t) [\mu(\tau_1) e^{-\alpha}, \rho(t_0)] e^{+\alpha} \rangle \\ &\quad + \langle \mu(t) e^{-\alpha} [e^{+\alpha}, \rho(t_0)] \mu(\tau_1) \rangle) \\ &= \int_{t_0}^t d\tau_1 E(\tau_1) (\langle \mu(t) \mu(\tau_1) [e^{-\alpha}, \rho(t_0)] e^{+\alpha} \rangle \\ &\quad + \langle \mu(t) [\mu(\tau_1), \rho(t_0)] \cancel{e^{-\alpha}} e^{+\alpha} \rangle \\ &\quad + \langle \mu(t) e^{-\alpha} [e^{+\alpha}, \rho(t_0)] \mu(\tau_1) \rangle) \end{aligned}$$

$$\begin{aligned}
&= \int_{t_0}^t d\tau_1 E(\tau_1) (\langle \mu(t) \mu(\tau_1) [e^{-\alpha}, \rho(t_0)] e^{+\alpha} \rangle \\
&\quad + \langle \mu(t) [\mu(\tau_1), \rho(t_0)] \rangle \\
&\quad + \langle \mu(t) e^{-\alpha} [e^{+\alpha}, \rho(t_0)] \mu(\tau_1) \rangle) \\
&= \int_{t_0}^t d\tau_1 E(\tau_1) (\langle \mu(t) \mu(\tau_1) e^{-\alpha} \rho(t_0) e^{+\alpha} \rangle - \langle \mu(t) \mu(\tau_1) \rho(t_0) e^{-\alpha} e^{+\alpha} \rangle \\
&\quad + \langle \mu(t) [\mu(\tau_1), \rho(t_0)] \rangle \\
&\quad + \langle \mu(t) e^{-\alpha} e^{+\alpha} \rho(t_0) \mu(\tau_1) \rangle - \langle \mu(t) e^{-\alpha} \rho(t_0) e^{+\alpha} \mu(\tau_1) \rangle) \\
&= \int_{t_0}^t d\tau_1 E(\tau_1) (\langle \mu(t) \mu(\tau_1) e^{-\alpha} \rho(t_0) e^{+\alpha} \rangle - \langle \mu(t) \mu(\tau_1) \rho(t_0) \rangle \\
&\quad + \langle \mu(t) [\mu(\tau_1), \rho(t_0)] \rangle \\
&\quad + \langle \mu(t) \rho(t_0) \mu(\tau_1) \rangle - \langle \mu(t) e^{-\alpha} \rho(t_0) e^{+\alpha} \mu(\tau_1) \rangle) \\
&= \int_{t_0}^t d\tau_1 E(\tau_1) (\langle \mu(t) \mu(\tau_1) e^{-\alpha} \rho(t_0) e^{+\alpha} \rangle - \langle \mu(t) \mu(\tau_1) \rho(t_0) \rangle \\
&\quad + \langle \mu(t) [\mu(\tau_1), \rho(t_0)] \rangle \\
&\quad + \langle \mu(\tau_1) \mu(t) \rho(t_0) \rangle - \langle \mu(\tau_1) \mu(t) e^{-\alpha} \rho(t_0) e^{+\alpha} \rangle) \\
&= \int_{t_0}^t d\tau_1 E(\tau_1) (\langle \mu(t) [\mu(\tau_1), \rho(t_0)] \rangle)
\end{aligned}$$

This derivation is mainly an application of the product rule for commutators and finally the execution of commutators.

For the last step, the following is used:

$$\begin{aligned}
\mu(\tau_1) \mu(t) \rho(t_0) &= \mu(0) e^{-i\omega\tau_1} \mu(0) e^{-i\omega t} \rho(t_0) \\
&= \mu(0) e^{-i\omega t} \mu(0) e^{-i\omega\tau_1} \rho(t_0) = \mu(t) \mu(\tau_1) \rho(t_0)
\end{aligned}$$

# Bibliography

---

- Abugo, O. O., Nair, R., and Lakowicz, J. R. (2000). Fluorescence properties of rhodamine 800 in whole blood and plasma. *Analytical Biochemistry*, 279:142–150.
- Achazi, G. and Cannizzo, A. (2017). Fourier transform spectral interferometry with non-phase stable setups by broadband single shot detection of fs and ps pulses. *Review of Scientific Instruments*, 88(8):083110.
- Alessi, A., Salvalaggio, M., and Ruzzon, G. (2013). Rhodamine 800 as reference substance for fluorescence quantum yield measurements in deep red emission range. *Journal of Luminescence*, 134:385–389.
- Baum, P., Breuer, M., Riedle, E., and Steinmeyer, G. (2006). Brewster-angle chirped mirrors for broadband pulse compression without dispersion oscillations. *Conference on Lasers and Electro-Optics and 2006 Quantum Electronics and Laser Science Conference, CLEO/QELS 2006*, 31(14):2220–2222.
- Bohinc, R., Pamfilidis, G., Rehault, J., Radi, P., Milne, C., Szlachetko, J., Bencivenga, F., Capotondi, F., Cucini, R., Foglia, L., Masciovecchio, C., Minci-grucci, R., Pedersoli, E., Simoncig, A., Mahne, N., Cannizzo, A., Frey, H. M., Ollmann, Z., Feurer, T., Maznev, A. A., Nelson, K., and Knopp, G. (2019). Nonlinear XUV-optical transient grating spectroscopy at the Si L<sub>2,3</sub>-edge. *Applied Physics Letters*, 114(18):1–6.
- Bransden, B. H. and Joachain, C. J. (1998). *Physics of Atoms and Molecules*. Addison Wesley Longman, Harlow, Essex.
- Brida, D., Manzoni, C., and Cerullo, G. (2012). Phase-locked pulses for two-dimensional spectroscopy by a birefringent delay line. *Optics Letters*, 37(15):3027–3029.
- Brixner, T., Stenger, J., Vaswani, H., Cho, M., Blankenship, R., and Fleming, G. (2005). Two-dimensional spectroscopy of electronic couplings in photosynthesis. *Nature*, 434:625 – 628.
- Brixner, T., Stiopkin, I. V., and Fleming, G. R. (2004). Tunable two-dimensional femtosecond spectroscopy. *Optics Letters*, 29(8):884–886.

- Cavalieri, A. L., Müller, N., Uphues, T., Yakovlev, V. S., Baltuška, A., Horvath, B., Schmidt, B., Blümel, L., Holzwarth, R., Hendel, S., Drescher, M., Kleineberg, U., Echenique, P. M., Kienberger, R., Krausz, F., and Heinzmann, U. (2007). Attosecond spectroscopy in condensed matter. *Nature*, 449(7165):1029–1032.
- Cerullo, G. and De Silvestri, S. (2003). Ultrafast optical parametric amplifiers. *Review of Scientific Instruments*, 74(1).
- Ciddor, P. E. (1996). Refractive index of air: new equations for the visible and near infrared. *Applied Optics*, 35(9):1566–1573.
- Cowan, M., Ogilvie, J., and Miller, R. (2004). Two-dimensional spectroscopy using diffractive optics based phased-locked photon echoes. *Chemical Physics Letters*, 386(1):184 – 189.
- Dobrowolski, J. A., Tikhonravov, A. V., Trubetskov, M. K., Sullivan, B. T., and Verly, P. G. (1996). Optimal single-band normal-incidence antireflection coatings. *Applied Optics*, 35(4):644.
- Dubietis, A., Tamošauskas, G., Šuminas, R., Jukna, V., and Couairon, A. (2017). Ultrafast supercontinuum generation in bulk condensed media. *Lithuanian Journal of Physics*, 57(3):1–34.
- Dudovich, N., Oron, D., and Silberberg, Y. (2002). Single-pulse coherently controlled nonlinear Raman spectroscopy and microscopy. *Nature*, 418:512–514.
- Extermann, J., Weber, S. M., Kiselev, D., Bonacina, L., Lani, S., Jutzi, F., Noell, W., de Rooij, N. F., and Wolf, J.-P. (2011). Spectral phase, amplitude, and spatial modulation from ultraviolet to infrared with a reflective MEMS pulse shaper. *Optics Express*, 19(8):7580–7586.
- Feurer, T. and Roberts, G. (2009). Femtosecond Light: Optics and Interactions.
- Fisher, R. A. and Kelley, P. L. (1969). Subpicosecond pulse generation using the optical Kerr effect. *Applied Physics Letters*, 14(4):140–143.
- Fuller, F. D. and Ogilvie, J. P. (2015). Experimental Implementations of Two-Dimensional Fourier Transform Electronic Spectroscopy. *Annual Review of Physical Chemistry*, 66(1):667–690.

- Golonzka, O., Khalil, M., Demirdöven, N., and Tokmakoff, A. (2001). Vibrational Anharmonicities Revealed by Coherent Two-Dimensional Infrared Spectroscopy. *Physical Review Letters*, 86:2154–2157.
- Goodno, G. D., Dadusc, G., and Miller, R. J. D. (1998). Ultrafast heterodyne-detected transient-grating spectroscopy using diffractive optics. *Journal of the Optical Society of America B*, 15(6):1791–1794.
- Hacker, M., Stobrawa, G., Sauerbrey, R., Buckup, T., Motzkus, M., Wildenhain, M., and Gehner, A. (2003). Micromirror SLM for femtosecond pulse shaping in the ultraviolet. *Applied Physics B*, 76(6):711–714.
- Hamm, P., Lim, M., and Hochstrasser, R. M. (1998). Structure of the Amide I Band of Peptides Measured by Femtosecond Nonlinear-Infrared Spectroscopy. *The Journal of Physical Chemistry B*, 102(31):6123–6138.
- Hamm, P. and Zanni, M. (2011). *Concepts and Methods of 2D Infrared Spectroscopy*. Cambridge University Press.
- Hannaford, P. (2005). *Femtosecond laser spectroscopy*. Springer.
- Huang, F., Yang, W., and Warren, W. S. (2001). Quadrature spectral interferometric detection and pulse shaping. *Optics Letters*, 26(6):382–384.
- Hybl, J. D., Albrecht, A. W., Faeder, S. M. G., and Jonas, D. M. (1998). Two-dimensional electronic spectroscopy. *Chemical Physics Letters*, 297(3):307 – 313.
- Johnson, M. L. (2000). Parameter correlations while curve fitting. In *Numerical Computer Methods, Part C*, volume 321 of *Methods in Enzymology*, pages 424–446. Academic Press.
- Jonas, D. M. (2003). Two-Dimensional Femtosecond Spectroscopy. *Annual Review of Physical Chemistry*, 54(1):425–463. PMID: 12626736.
- Klimczak, M., Siwicki, B., Heidt, A., and Buczyński, R. (2017). Coherent supercontinuum generation in soft glass photonic crystal fibers. *Photonics Research*, 5(6):710–727.
- Krebs, N., Pugliesi, I., Hauer, J., and Riedle, E. (2013). Two-dimensional Fourier transform spectroscopy in the ultraviolet with sub-20 fs pump pulses and 250–720 nm supercontinuum probe. *New Journal of Physics*, 15.

- Laude, V. and Tournois, P. (1999). Chirped-mirror-pairs for ultra-broadband dispersion control. In *Summaries of papers presented at the Conference on Lasers and Electro-Optics. Postconference Edition. CLEO '99*, page 187.
- Maiuri, M., Garavelli, M., and Cerullo, G. (2020). Ultrafast spectroscopy: State of the art and open challenges. *Journal of the American Chemical Society*, 142(1):3–15. PMID: 31800225.
- Malitson, I. H. (1963). A Redetermination of Some Optical Properties of Calcium Fluoride. *Applied Optics*, 2(11):1103–1107.
- Malitson, I. H. (1965). Interspecimen Comparison of the Refractive Index of Fused Silica. *Journal of the Optical Society of America*, 55(10):1205–1209.
- Matuschek, N., Kärtner, F. X., and Keller, U. (1999). Analytical Design of Double-Chirped Mirrors with Custom-Tailored Dispersion Characteristics. *IEEE Journal of Quantum Electronics*, 35(2):129–137.
- Maznev, A. A., Nelson, K. A., and Rogers, J. A. (1998). Optical heterodyne detection of laser-induced gratings. *Optics Letters*, 23(16):1319–1321.
- Mukamel, S. (1995). *Principles of Nonlinear Optical Spectroscopy*. Oxford series in optical and imaging sciences. Oxford University Press.
- Mukamel, S., Healion, D., Zhang, Y., and Biggs, J. D. (2013). Multidimensional Attosecond Resonant X-Ray Spectroscopy of Molecules: Lessons from the Optical Regime. *Annual Review of Physical Chemistry*, 64(1):101–127.
- Myers, J. A., Lewis, K. L., Tekavec, P. F., and Ogilvie, J. P. (2008). Two-color two-dimensional Fourier transform electronic spectroscopy with a pulse-shaper. *Optics Express*, 16(22):17420.
- Nazari, M. (2018). *Long-Range Energy Transfer in DNA-Hosted Multichromophoric Systems by Ultrafast 1D and 2D fs UV-Vis Transient Absorption Spectroscopy*. PhD thesis, University of Bern.
- Rodriguez, Y., Frei, F., Cannizzo, A., and Feurer, T. (2015). Pulse-shaping assisted multidimensional coherent electronic spectroscopy. *Journal of Chemical Physics*, 142(21):212451.



- Sardesai, H. P., Chang, C.-C., and Weiner, A. M. (1998). A Femtosecond Code-Division Multiple-Access Communication System Test Bed. *Journal of Light-wave Technology*, 16(11):1953.
- Schlau-Cohen, G. S., Dawlaty, J. M., and Fleming, G. R. (2012). Ultrafast multidimensional spectroscopy: Principles and applications to photosynthetic systems. *IEEE Journal of Selected Topics in Quantum Electronics*, 18(1):283–295.
- Schott (2017). *Schott Glass Data Sheet*. SCHOTT North America, Inc, 400 York Avenue, Duryea, PA 18642, USA.
- Selig, U., Langhojer, F., Dimler, F., Löhrig, T., Schwarz, C., Giesecking, B., and Brixner, T. (2008). Inherently phase-stable coherent two-dimensional spectroscopy using only conventional optics. *Optics Letters*, 33(23):2851–2853.
- Shim, S. H., Strasfeld, D. B., Ling, Y. L., and Zanni, M. T. (2007). Automated 2D IR spectroscopy using mid-IR pulse shaping and applications to membrane peptides. *Optics InfoBase conference papers series*, 104(36).
- Son, M., Mosquera-Vazquez, S., and Schlau-Cohen, G. S. (2017). Ultrabroadband 2D electronic spectroscopy with high-speed, shot-to-shot detection. *Optics Express*, 25(16):18950.
- Steinmeyer, G. (2003). Dispersion oscillations in ultrafast phase-correction devices. *IEEE Journal of Quantum Electronics*, 39(8):1027–1034.
- Szipöcs, R., Spielmann, C., Krausz, F., and Ferencz, K. (1994). Chirped multilayer coatings for broadband dispersion control in femtosecond lasers. *Optics Letters*, 19(3):201.
- Thurston, R. N., Heritage, J. P., Weiner, A. M., and Tomlinson, W. J. (1986). Analysis of Picosecond Pulse Shape Synthesis by Spectral Masking in a Grating Pulse Compressor. *IEEE Journal of Quantum Electronics*, 22(5):682–696.
- Tian, P., Keusters, D., Suzuki, Y., and Warren, W. S. (2003). Femtosecond Phase-Coherent Two-Dimensional Spectroscopy. *Science*, 300:1553–1556.
- Trebino, R., DeLong, K. W., Fittinghoff, D. N., Sweetser, J. N., Krumbügel, M. A., Richman, B. A., and Kane, D. J. (1997). Measuring ultrashort laser pulses in the time-frequency domain using frequency-resolved optical gating. *Review of Scientific Instruments*, 68(9):3277–3295.

- Tseng, C.-h., Matsika, S., and Weinacht, T. C. (2009). Two-Dimensional Ultrafast Fourier Transform Spectroscopy in the Deep Ultraviolet. *Optics Express*, 17(21):9348–9349.
- Vaughan, J. C., Hornung, T., Feurer, T., and Nelson, K. A. (2005). Diffraction-based femtosecond pulse shaping with a two-dimensional spatial light modulator. *Optics Letters*, 30(3):323.
- Volkov, V., Schanz, R., and Hamm, P. (2005). Active phase stabilization in Fourier-transform two-dimensional infrared spectroscopy. *Optics Letters*, 30(15):2010–2012.
- von Vacano, B., Buckup, T., and Motzkus, M. (2007). Shaper-assisted collinear SPIDER: fast and simple broadband pulse compression in nonlinear microscopy. *Journal of the Optical Society of America B*, 24(5):1091.
- Weiner, A. M. (2000). Femtosecond pulse shaping using spatial light modulators. *Review of Scientific Instruments*, 71(5).
- Weiner, A. M., Leaird, D. E., Patel, J. S., and Wullert, J. R. (1992). Programmable Shaping of Femtosecond Optical Pulses by Use of 128-Element Liquid Crystal Phase Modulator. *IEEE Journal of Quantum Electronics*, 28(4):908–920.
- Woutersen, S. and Hamm, P. (2000). Structure Determination of Trialanine in Water Using Polarization Sensitive Two-Dimensional Vibrational Spectroscopy. *The Journal of Physical Chemistry B*, 104(47):11316–11320.
- Zeek, E., Maginnis, K., Backus, S., Russek, U., Murnane, M., Mourou, G., Kapteyn, H., and Vdovin, G. (1999). Pulse compression by use of deformable mirrors. *Optics Letters*, 24(7):493.
- Zhang, T., Borca, C. N., Li, X., and Cundiff, S. T. (2005). Optical two-dimensional Fourier transform spectroscopy with active interferometric stabilization. *Optics Express*, 13(19):7432–7441.